BRNO UNIVERSITY OF TECHNOLOGY
VYSOKÉ UČENÍ TECHNICKÉ V BRNĚ

FACULTY OF ELECTRICAL ENGINEERING AND COMMUNICATION
FAKULTA ELEKTROTECHNIKY
A KOMUNIKAČNÍCH TECHNOLOGIÍ

DEPARTMENT OF CONTROL AND INSTRUMENTATION
ÚSTAV AUTOMATIZACE A MĚŘICÍ TECHNIKY

MODELING AND CONTROL OF AC ELECTRIC DRIVES DURING FAULT CONDITIONS
MODELOVÁNÍ A ŘÍZENÍ STŘÍDAVÝCH ELEKTRICKÝCH POHONŮ PŘI PORUŠE

DOCTORAL THESIS
DIZERTAČNÍ PRÁCE

AUTHOR — **Ing. Matúš Kozovský**
AUTOR PRÁCE

SUPERVISOR — **doc. Ing. Petr Blaha, Ph.D.**
ŠKOLITEL

BRNO 2020

ABSTRACT

The thesis deals with modeling and control methods of the electric motor during failure. The work focuses exclusively on multi-phase motors. The first part of the thesis deals with the mathematical equations of a general multi-phase motor and the equation derivation for n-times three-phase connection. Models in dq coordinates and models in stator coordinates are designed to simulate the behaviour of the motor during a failure. The next part of the thesis deals with the multi-phase motors fault analysis using designed mathematical models. The various internal structures of the motor windings are analyzed from the motor control during a failure point of view. The behaviour of the different motor structures under a fault condition is shown. Motor electrical faults, as well as power stage faults, are analysed.

The last part of the thesis deals with the designed control algorithm and fault compensation strategies tests using real motors. The segregate dual three-phase motor and the interlaced experimental motor with internal short-circuit emulation functionality were used for testing. Realised tests demonstrate that a properly designed motor in combination with the well-designed control algorithm and power electronics can guarantee continuous motor run during a failure.

KEYWORDS

Multi-phase PMSM, motor fault analysis, winding faults, motor faults modeling, fault control

ABSTRAKT

Dizertační práce se zabývá modelováním a řízením elektrických pohonů během poruchových stavů. Práce se obzvláště zaměřuje na více-fázové motory. První část práce se zabývá matematickými rovnicemi obecného více-fázového motoru a následným odvozením n-krát troj-fázového zapojení motoru. Modely v dq souřadnicovém systému a modely ve statorových souřadnicích jsou navrženy pro simulaci chování motoru během poruchových stavů. Další část práce se zabývá analýzou poruch ve více-fázových motorech s využitím matematických modelů. Různé vnitřní struktury vinutí motoru jsou analyzovány z pohledu možného řízení během poruchového stavu. Taktéž je prezentováno chování těchto různých struktur motoru během poruchových stavů. Předmětem analýzy jsou elektrické poruchy vinutí motoru a elektrické poruchy výkonové elektroniky. Poslední část práce se zabývá testováním navrženého řídícího algoritmu a navržených kompenzačních strategií pro poruchy na reálných motorech. Pro testování byl použit segregovaný dvakrát troj-fázový motor a experimentální motor s odbočkami pro emulaci poruch vinutí. Provedené testy prokázaly, že vhodně navrhnutý motor v kombinaci se správným řídícím algoritmem a výkonovou elektronikou dokáže zaručit kontinuální běh pohonu i během poruchy.

KLÍČOVÁ SLOVA

Více-fázové PMSM, analýza poruchových stavů motoru, poruchy vinutí motoru, modelování poruch motoru, řízení při poruchových stavech

KOZOVSKÝ, M. *Modeling and control of AC electric drives during fault conditions*. Brno, 2020, 111 p. Doctoral thesis. Brno University of Technology, Faculty of Electrical Engineering and Communication , Department of Control and Instrumentation. Advised by doc. Ing. Petr Blaha, Ph.D.

DECLARATION

I declare that I have written the Doctoral Thesis titled "Modeling and control of AC electric drives during fault conditions" independently, under the guidance of the advisor and using exclusively the technical references and other sources of information cited in the thesis and listed in the comprehensive bibliography at the end of the thesis.

As the author I furthermore declare that, with respect to the creation of this Doctoral Thesis, I have not infringed any copyright or violated anyone's personal and/or ownership rights. In this context, I am fully aware of the consequences of breaking Regulation § 11 of the Copyright Act No. 121/2000 Coll. of the Czech Republic, as amended, and of any breach of rights related to intellectual property or introduced within amendments to relevant Acts such as the Intellectual Property Act or the Criminal Code, Act No. 40/2009 Coll., Section 2, Head VI, Part 4.

Brno ....

author's signature

ACKNOWLEDGEMENT

I would like to thank my supervisor, doc. Ing. Petr Blaha, Ph.D., for the proffesional guidance, encouragement and advices he has provided throughout my time as his Ph.D.student.
Special thanks comes also to my wife Zuzana, as without her support and motivation I may never have completed this thesis.
The research dealt with in this thesis was partially financially supported from the Horizon 2020 program of the European Union within the project 737469 Autodrive - Advancing fail-aware, fail-safe, and fail-operational electronic components, systems, and architectures for fully automated driving to make future mobility safer, more efficient, affordable, and end-user acceptable.

Brno ....

author's signature

CONTENTS

LIST OF FIGURES

LIST OF TABLES

1 INTRODUCTION

1.1 Motivation

The development in the field of fully automated electric vehicles was massively growing during the last couple of years. It has become apparent that automated driving poses strong requirements on system reliability and safety. Fail-safe or even fail-operational architectures need to be developed. Requirements on reliability spread from breaking and steering subsystems also to other ones like powertrain, sensing systems, etc [1].

The redundancy is a common approach to increase the reliability and availability of systems. Different redundancy concepts are used in practice. The two-out-of-three (2oo3) architecture which is typically used in the aviation field would be very expensive in the automotive field and therefore unusable. The one-out-of-two with self-diagnostic (1oo2D) is therefore an option there.

Increasing requirements on reliability and high power density of electric machines are leading to higher requirements on control algorithms, self-diagnostic algorithms as well as to innovative electric machine designs. Three-phase permanent magnet synchronous machines (PMSM) are well known for their high power density and high-efficiency but they usually fail with one fault. Utilization of multi-phase motors or motors composed from multiple 3-phase sub-systems brings needed redundancy while keeping one motor but for the price of mutual couplings. This solution leads not only to higher machine reliability but can lead also to higher machine efficiency, a smoother generated torque and also to a possible price reduction.

1.2 Multi-phase machines

The windings of multi-phase machines can be connected in many different ways. Machine behaviour is closely related to the internal hardware structure; the behaviour can differ according to the possible winding arrangements of the stator as well as to the magnets' distribution in the rotor.

Specially designed multi-phase machines can operate during an electrical fault of the power inverter, or even during an electrical motor fault. The behaviour during fault conditions needs to be considered during the motor design process of those machines. This is why fault analysis is important.

The complexity of control algorithms and motor models grows with the complexity of the electric machine itself. Nevertheless, multi-phase machines have many advantages in comparison to classic three-phase machines. However, the control algorithm needs to be adapted to the specific motor structure. Each multi-phase motor structure requires an individual control approach during the fault. Behaviour during the motor fault needs to be considered during the control algorithm design.

1.3 Faults in PMS machines

The typical faults of three-phase PMS machines are well known. The faults can be classified into three categories: electrical faults, mechanical faults and magnetic faults. Magnetic faults are related to PMSM machines, for instance, demagnetisation fault. Mechanical faults include magnet damage, shaft bending, air gap eccentricity, and the most typical mechanical fault which is bearing fault. Bearing faults represents almost 40–50 % of all motor faults [2]. This thesis deals with motor electrical faults and power inverter transistor faults. Stator faults constitute 38 % of all motor faults [2]. The most common fault of the stator windings in PMSM is the interturn short-circuit.

1.4 Model-based design

The motor control algorithm is typically designed with the help of motor models. Model-based design requires a precise motor model. Models that can simulate motor behaviour during the fault are required to design and verify the control algorithms. The fail-operational control algorithm needs to operate properly during motor or inverter faults.

Motor models can also predict the behaviour of the machine which is under the design process. Well designed motor models can help to find principal problems before motor construction itself.

1.5 Tested motors

Several different motor structures are considered during the behaviour analysis which is a part of this thesis. All analysed structures have the same nominal power to highlight differences in the behaviour. However, real experiments are realised using two different motors. The first tested motor is dual three-phase PMS motor with segregated structure. This is a high-performance motor, which does not allow to emulate electrical faults inside of the machine. The parameters of this motor are equal to analysed motors.

The second motor is a small experimental motor that was specially designed to verify control strategies for the machine under the fault condition. The motor was designed as a machine with segregated windings. Internal short-circuits or even an internal short circuit between different phases or even between sub-systems can be emulated using this motor.

Power density and peak power of this machine are significantly smaller in comparison with analysed motors. However, realised experiments demonstrate machine capability to continuously operate under different fault conditions.

2 STATE OF THE ART

Permanent magnet synchronous (PMS) motors are used for their high power density and higher efficiency applications compared to asynchronous motors. Behaviour during the fault is also determined by the mechanical construction. The main disadvantage of PMS motors is their behaviour during fault conditions. Permanent magnets located in the rotor induce voltage in the stator windings while the rotor is spinning. Induced voltage can cause overcurrent and subsequent thermal damage of the motor in some failure states. The fail-operational system can be created using multi-phase system [3]. Another option to create a fail-operational system is by connecting each motor phase to an individual inverter H bridge [4, 5]. Multi-phase motor construction requires specific parameters to operate during faults [6]. High reliability can be reached by using a combination of multi-phase motor structures with fail operation methods for three-phase motors [7].

Many different multi-phase motor constructions exist. Every construction has its advantages and disadvantages. Multi-phases motors are typically controlled using Field Oriented Control (FOC) similar to classic three-phase motors. Multi-phase motors have higher efficiency in comparison to a three-phase equivalent [8]. Multi-phase motors can be divided into two large categories [9]. The first category is represented by general multi-phase motors [10, 11]. All coils are electrically connected into one n-phase star and as a consequence phase currents are transformed into one set of dq currents. Used space transformations are adapted for multi-phase arrangement. These motors can be controlled during open phase fault [12, 13]. Multi-phase motors with suitable parameters can even operate during interturn short-circuit fault [14]. Multi-phase motors are typically fully symmetrical due to mechanical construction. Asymmetry is caused only by fault.

Second category is represented by multiple k-phase motor [15, 16]. Phase currents of these motors are transformed into multiple sets of dq currents [9]. Electrical fault can be isolated into one motor sub-system [17]. This behaviour can be helpful during winding faults. Short-circuit between winding and motor case is one typical electric fault of electric machines. Interturn short-circuit and disconnected phase are other typical electrical motor faults [18, 19, 20]. Multiple k-phase motors can operate during open phase fault [21], or even during the short-circuit faults [22]. Different compensation methods can be used to reduce current distortion or torque ripples during fault conditions. Compensation methods are closely related to the structure of the machine. Multiple k-phase motors are typically symmetrical as general multi-phase motors. However, individual motor sub-systems can be symmetrical or asymmetrical according to stator arrangement.

The sub-system can be evenly distributed in the stator. This is the case of an

interlaced windings arrangement [23]. The benefit of this arrangement lies in the symmetry of each sub-system. During fault conditions individual sub-systems can be electrically interconnected to each other during fault. In this case the fault affects both sub-systems. This is one of the biggest disadvantages of an interlaced geometrical arrangement. Another possible arrangement is to geometrically separate individual sub-systems. This is referred to as segregated windings [17]. The probability of an electrical connection between sub-systems is eliminated by the electrical insulation and the geometrical distance. However, mutual inductances in the sub-system are not equal in all windings pairs. This mean that individual sub-systems themselves are not fully symmetric.

3 DISSERTATION OBJECTIVES

The aim of the dissertation is to derive a mathematical model of a multi-phase motor and realise the model in MATLAB/Simulink. Dual three-phase or triple three-phase motor arrangements are considered.

The model must respect mutual couplings between individual motor windings. The realised model should be able to simulate multi-phase motor behaviour during normal operation without any fault and also during electrical faults of the motor stator or the power inverter.

The motor model will be used to analyse motor behaviour during fault conditions and to design a proper control strategy during fault conditions. Any control strategy during fault conditions needs to provide smooth motor run and to reduce high fault current amplitude and torque oscillations. The motor should be able to operate continuously during the fault using the prepared control strategy. The fault control method will consider inverter with one leg per motor phase.

Designed control strategy will be used in six-phase power inverter to verify behaviour during fault using real dual three-phase PMS motor.

Objectives can be summarized in the following points:

- Familiarization with the electric drives modelling methods using MATLAB Simulink.
- Development of the multi-phase motor model suitable for fault simulation.
- Analysis of multi-phase motor arrangement influence on motor behaviour.
- Simulation of fault behaviour during individual multi-phase faults using the developed motor model.
- Analysis of possible multi-phase motor faults and proposal of compensation strategies.
- Development and verification of the control method for the dual three-phase motor.

4 MULTI-PHASE PMSM MOTOR MODEL

The multi-phase motor model has to understand the behaviour of multi-phase motors. Several possible methods of designing a motor model exists. Selected modelling platforms have to provide the possibility of creating the motor model and also of testing the model in different operation stages. MATLAB/Simulink was chosen for motor modelling. Control algorithms can also be created and tested in this environment. MATLAB automatic code generation simplifies the process of migration of control algorithms onto the target platform.

4.1 Space transformations

These transformations convert variables from one coordinate system to another one. The calculation can be easier in new coordination system. The most commonly used transformations related to motors are Clarke and Park transformations. Motor variables can be transformed from the *abc* stator coordinate system into rotor *dq* coordinates. These transformations are typically used by motor control algorithms. The same transformations can be used to simplify motor models.

4.1.1 Clarke transformation

The Clarke transformation converts the motor variables voltage/current represented by variable x from stator coordinates into two dimensional $\alpha\beta$ coordinates. $\alpha\beta$ coordinates are perpendicular to each other. The specific form of this transformation depends on the stator winding distribution and pole-pairs count. Transformation have the following mathematical form (4.1).

$$\begin{bmatrix} x_\alpha \\ x_\beta \end{bmatrix} = \boldsymbol{T}_{\alpha\beta} * \begin{bmatrix} x_a \\ x_b \\ \vdots \\ x_n \end{bmatrix} = \frac{2}{n} \begin{bmatrix} \cos(\varphi_a) & \cos(\varphi_b) & \cdots & \cos(\varphi_n) \\ \sin(\varphi_a) & \sin(\varphi_b) & \cdots & \cos(\varphi_n) \end{bmatrix} \begin{bmatrix} x_a \\ x_b \\ \vdots \\ x_n \end{bmatrix} \tag{4.1}$$

Variable n represents number of motor phases which are transformed into $\alpha\beta$ coordinates. Variable φ denotes electrical angle between individual motor phases and stator reference axis α. This transformation holds for multi-phase systems; however, it is typically used for three-phase system. Geometrical distance between coils is 120 electrical degrees for symmetrical three-phase motor. Transformation has then the

following form:

$$\begin{bmatrix} x_\alpha \\ x_\beta \end{bmatrix} = \boldsymbol{T}_{\alpha\beta} * \begin{bmatrix} x_a \\ x_b \\ x_c \end{bmatrix} = \frac{2}{3} \begin{bmatrix} 1 & \frac{-1}{2} & \frac{-1}{2} \\ 0 & \frac{\sqrt{3}}{2} & -\frac{\sqrt{3}}{2} \end{bmatrix} \begin{bmatrix} x_a \\ x_b \\ x_c \end{bmatrix} \tag{4.2}$$

The method of converting variables from $\alpha\beta$ coordinates back to abc coordinates is similar. It is called inverse Clarke transformation and it is described by Eq (4.3).

$$\begin{bmatrix} x_a \\ x_b \\ x_c \end{bmatrix} = \boldsymbol{T}^{-1}_{\alpha\beta} * \begin{bmatrix} x_\alpha \\ x_\beta \end{bmatrix} = \begin{bmatrix} 1 & 0 \\ \frac{-1}{2} & \frac{\sqrt{3}}{2} \\ \frac{-1}{2} & -\frac{\sqrt{3}}{2} \end{bmatrix} \begin{bmatrix} x_\alpha \\ x_\beta \end{bmatrix} \tag{4.3}$$

Variables transformed into $\alpha\beta$ coordinate system are typically not directly used in control algorithm or motor models. Variables are usually further transformed by using another transformation. [24]

4.1.2 Park transformation

This transformation recalculates variables from $\alpha\beta$ coordinates into rotor dq coordinates. The motor rotor continuously changes its position during motor operation, and the transformation matrix continuously changes its coefficients. Each coefficient is dependent on the current electrical angle of motor rotor θ_r. This variable represents electrical angle between direct rotor axis d and motor phase a. The transformation has the following form:

$$\begin{bmatrix} x_d \\ x_q \end{bmatrix} = \boldsymbol{T}_{dq} * \begin{bmatrix} x_\alpha \\ x_\beta \end{bmatrix} = \begin{bmatrix} \cos(\theta_r) & \sin(\theta_r) \\ -\sin(\theta_r) & \cos(\theta_r) \end{bmatrix} \begin{bmatrix} x_\alpha \\ x_\beta \end{bmatrix} \tag{4.4}$$

The reverse transformation is in fact a rotation in the opposite direction. Inverse transformation is described by the Eq. (4.5).

$$\begin{bmatrix} x_\alpha \\ x_\beta \end{bmatrix} = \boldsymbol{T}^{-1}_{dq} * \begin{bmatrix} x_d \\ x_q \end{bmatrix} = \begin{bmatrix} \cos(\theta_r) & -\sin(\theta_r) \\ \sin(\theta_r) & \cos(\theta_r) \end{bmatrix} \begin{bmatrix} x_d \\ x_q \end{bmatrix} \tag{4.5}$$

4.2 Simulink *dq* model

4.2.1 General multi-phase motor

Multi-phase motor models can be realised using different modelling methods. A motor model implemented in dq coordinates is one of the most common modelling methods. This model is simpler in comparison to other models. Field oriented control methods are also typically implemented in dq coordinates. The understanding of dq coordinates motor behaviour is important for this reason.

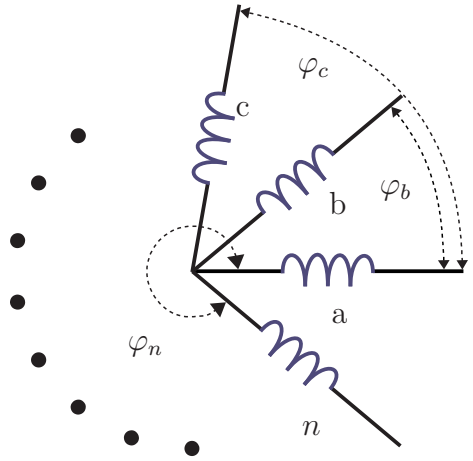

Fig. 4.1: General multi-phase motor arrangement.

The electrical behaviour of general multi-phase motors can be described by equation (4.6). The equation is calculated in stator abc coordinates. This matrix equation can be used for dual three-phase motors or general multi-phase motors.

$$\boldsymbol{u}_{ab..n} = \boldsymbol{R}_{ab..n}\boldsymbol{i}_{ab..n} + \frac{\mathrm{d}\boldsymbol{L}_{ab..n}\boldsymbol{i}_{ab..n}}{\mathrm{d}t} + \frac{\mathrm{d}\boldsymbol{\Psi}_{Mab..n}}{\mathrm{d}t} = \boldsymbol{R}_{ab..n}\boldsymbol{i}_{ab..n} + \frac{\mathrm{d}\boldsymbol{L}_{ab..n}\boldsymbol{i}_{ab..n}}{\mathrm{d}t} + \boldsymbol{e}_{ab..n} \tag{4.6}$$

Matrix $\boldsymbol{R}_{ab..n}$ denotes the resistances of individual coils while the variable $\boldsymbol{L}_{ab..n}$ represents winding inductances (the main diagonal elements) and also mutual inductances. Motor inductances are typically functions of rotor position. Inductance fluctuation depends on stator geometry. Variables $\boldsymbol{u}_{ab..n}$ and $\boldsymbol{i}_{ab..n}$ represent motor currents and motor terminal voltages.

The $\boldsymbol{e}_{ab..n}$ variable reflects the influence of back electromotive force (back-EMF). It is the voltage, or electromotive force, that pushes against the magnetic field which induces it. This voltage is generated by the rotating magnetic field generated by the rotor permanent magnets. The back-EMF voltage defines the maximum operating speed of the motor using classical control methods. When the back-EMF voltage reaches critical level, the DC-link voltage is applied to balance the back-EMF and no voltage remains to generate torque. This maximum speed can be exceeded using field weakening control method. $\boldsymbol{e}_{ab..n}$vector consist of back-EMF voltages for individual coils (4.10).

Equation (4.7) reflects the torque generated by the machine. ω_e denotes the motor electrical speed of the motor. Variable Pp represents the number of motor

pole-pairs. T_e represents the torque generated by the machine.

$$T_e = Pp\left(\frac{1}{2}\boldsymbol{i}_{ab..n}^{\intercal}\frac{\mathrm{d}\boldsymbol{L}_{ab..n}}{\mathrm{d}\theta}\boldsymbol{i}_{ab..n} + \frac{\boldsymbol{i}_{ab..n}^{\intercal}\boldsymbol{e}_{ab..n}}{\omega_e}\right) \tag{4.7}$$

The generated torque can be used as an input variable when modelling motor mechanical parts.The mechanical model can be described by the following equations.

$$\frac{\mathrm{d}\omega_m}{\mathrm{d}t} = \frac{1}{J}\left(T_e - T_l\right) - \frac{B}{J}\omega_m \tag{4.8}$$

$$\frac{\mathrm{d}\theta_m}{\mathrm{d}t} = \omega_m \tag{4.9}$$

J represents the moment of inertia. T_l denotes the motor load torque. Variable B denotes the motor viscous friction. The mechanical speed ω_m relates with electrical speed through the formula $\omega_e = Pp\,\omega_m$. The mechanical system equations of multi-phase motors are identical to the classical three-phase motor mechanical equation.

Back-EMF voltage is a function of actual motor electric speed ω_e, and the back-EMF constant λ_m. Voltage on each motor phase can be described by the following equation (4.10).

$$e_n = \omega_e \lambda_m \cos(\theta + \varphi_n) \tag{4.10}$$

Variable θ represents the electric angle between stator reference axis α and a quadrature rotor axis q. The variable φ_n denotes the electrical angle between specific phase and stator reference. A motor is typically constructed to generate same back-EMF voltage amplitudes for each coil.

Electrical equations (4.6) can be transformed into dq coordinates using Park and Clarke transformations. Transformation matrices need to be adapted for n-phase motor. All phases are electrically connected to form one n-phase star in a general n-phase motor. Thereby all stator currents are transformed into one set of dq currents. Multiple three-phase motor electrical equations can be also recalculated into dq coordinates, however multiple sets of dq variables are formed using transformations. Example of using transformation matrixes is shown in equation (4.11) and (4.12).

$$\boldsymbol{T}_{\alpha\beta}^{-1}\boldsymbol{T}_{dq}^{-1}\boldsymbol{u}_{dq} = \boldsymbol{R}_{ab..n}\boldsymbol{T}_{\alpha\beta}^{-1}\boldsymbol{T}_{dq}^{-1}\boldsymbol{i}_{dq} + \frac{\mathrm{d}\boldsymbol{L}_{ab..n}\boldsymbol{T}_{\alpha\beta}^{-1}\boldsymbol{T}_{dq}^{-1}\boldsymbol{i}_{dq}}{\mathrm{d}t} + \boldsymbol{e}_{ab..n} \tag{4.11}$$

$$\boldsymbol{u}_{dq} = \boldsymbol{T}_{dq}\boldsymbol{T}_{\alpha\beta}\boldsymbol{R}_{ab..n}\boldsymbol{T}_{\alpha\beta}^{-1}\boldsymbol{T}_{dq}^{-1}\boldsymbol{i}_{dq} + \boldsymbol{T}_{dq}\boldsymbol{T}_{\alpha\beta}\frac{\mathrm{d}\boldsymbol{L}_{ab..n}\boldsymbol{T}_{\alpha\beta}^{-1}\boldsymbol{T}_{dq}^{-1}\boldsymbol{i}_{dq}}{\mathrm{d}t} + \boldsymbol{T}_{dq}\boldsymbol{T}_{\alpha\beta}\boldsymbol{e}_{ab..n} \tag{4.12}$$

The resistance matrix $\boldsymbol{R}_{ab..n}$ is transformed into dq coordinates using equation (4.13). Back-EMF voltage is transformed into one voltage constant, which is related

to q axis (4.14). Inductance transformation is the most problematic item. Derivation is divided into three parts. The first part is transformed into $\boldsymbol{L}_{dq}$ (4.15), other two parts are transformed into speed dependent cross-coupling term $\boldsymbol{C}_{dq}$ (4.16).

$$\boldsymbol{R}_{dq} = \boldsymbol{T}_{dq}\boldsymbol{T}_{\alpha\beta}\boldsymbol{R}_{ab..n}\boldsymbol{T}_{\alpha\beta}^{-1}\boldsymbol{T}_{dq}^{-1} \tag{4.13}$$

$$\boldsymbol{e}_{dq} = \boldsymbol{T}_{dq}\boldsymbol{T}_{\alpha\beta}\boldsymbol{e}_{ab..n} = \begin{bmatrix} 0 \\ \omega_e\lambda_m \end{bmatrix} \tag{4.14}$$

$$\boldsymbol{L}_{dq} = \boldsymbol{T}_{dq}\boldsymbol{T}_{\alpha\beta}\boldsymbol{L}_{ab..n}\boldsymbol{T}_{\alpha\beta}^{-1}\boldsymbol{T}_{dq}^{-1} \tag{4.15}$$

$$\boldsymbol{C}_{dq} = \boldsymbol{T}_{dq}\boldsymbol{T}_{\alpha\beta}\frac{\mathrm{d}\boldsymbol{L}_{ab..n}}{\mathrm{d}t}\boldsymbol{T}_{\alpha\beta}^{-1}\boldsymbol{T}_{dq}^{-1} + \boldsymbol{T}_{dq}\boldsymbol{T}_{\alpha\beta}\boldsymbol{L}_{ab..n}\boldsymbol{T}_{\alpha\beta}^{-1}\frac{\mathrm{d}\boldsymbol{T}_{dq}^{-1}}{\mathrm{d}t} \tag{4.16}$$

The motor electrical part equation transformed into dq coordinates has the following form (4.17).

$$\boldsymbol{u}_{dq} = \boldsymbol{R}_{dq}\boldsymbol{i}_{dq} + \boldsymbol{L}_{dq}\frac{\mathrm{d}\boldsymbol{i}_{dq}}{\mathrm{d}t} + \boldsymbol{C}_{dq}\boldsymbol{i}_{dq} + \boldsymbol{e}_{dq} \tag{4.17}$$

The cross-coupling item for a fully symmetrical three-phase system follows from (4.18).

$$\boldsymbol{C}_{dq} = \omega_e \begin{bmatrix} 0 & -Lq \\ Ld & 0 \end{bmatrix} \tag{4.18}$$

Variables $\boldsymbol{u}_{dq}$ and $\boldsymbol{i}_{dq}$ represent motor voltages and motor currents transformed into dq coordinates.

Fail operation strategy can be applied in some fault cases on a general multi-phase structure [13]. However, not every fault can be easily handled. For example, a short-circuited transistor causes an uncontrollable current through a fault related phase. Special hardware can be used in general multi-phase motors for damaged phase disconnection [25] which increases the complexity and the price. Hence a multiple three-phase motor structure can be used instead of general multi-phase structure.

4.2.2 Multiple three-phase motor model

This motor structure has some advantages in comparison to a general multi-phase motor. The behaviour of each three-phase sub-system is comparable with a classical three-phase motor during standard operation condition. Individual three-phase sub-systems are electrically separated. This separation is useful during faults. The fault causes problems only in one motor part (sub-system) while other sub-systems can

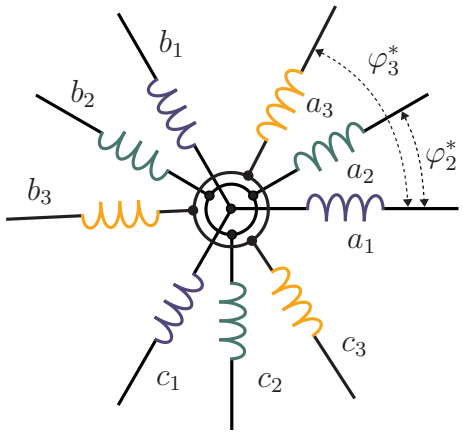

Fig. 4.2: Multiple three-phase motor arrangement.

continue to operate. A multiple three-phase windings connection is able to operate even during inverter short-circuited transistor fault.

We can use triple three-phase motor for example. This windings arrangement and connection into individual sub-systems is shown in figure 4.2. These sub-systems are electrically separated. Coupling between sub-systems is formed by shared rotor and windings mutual inductances. Individual three phase sub-systems can be geometrically shifted. The geometrical shift of sub-systems is defined by angle φ_i^*.

The sub-system model can be described by equation (4.19). The equation is divided into individual axes in dq coordinates.

$$\begin{aligned} u_{d_j} &= R_{dj} i_{d_j} + \frac{\mathrm{d}\psi_{d_j}}{\mathrm{d}t} - \omega_e \psi_{q_j} \\ u_{q_j} &= R_{q_j} i_{q_j} + \frac{\mathrm{d}\psi_{q_j}}{\mathrm{d}t} + \omega_e \psi_{d_j} \end{aligned} \tag{4.19}$$

R denotes the windings resistance in individual axis. This value is equal to stator winding resistance R_s. Variable ψ represents the motor magnetic flux and j denotes the index of sub-system ($j = \{1, 2, 3\}$).

Magnetic flux for individual axes can be described by (4.20)

$$\begin{aligned} \psi_{d1} &= \Psi_M + L_{d1} i_{d1} + M_{d1,d2} i_{d2} + M_{d1,d3} i_{d3} \\ \psi_{q1} &= L_{q1} i_{q1} + M_{q1,q2} i_{q2} + M_{q1,q3} i_{q3} \end{aligned} \tag{4.20}$$

Ψ_M represents the permanent magnet flux, L denotes the motor inductance and variable M represents the mutual inductance between sub-systems (both inductances for/between given axis and sub-system).

For simplification it will be assumed that all sub-systems have the same electrical characteristic and mutual inductances between sub-systems are the same. (4.19) can

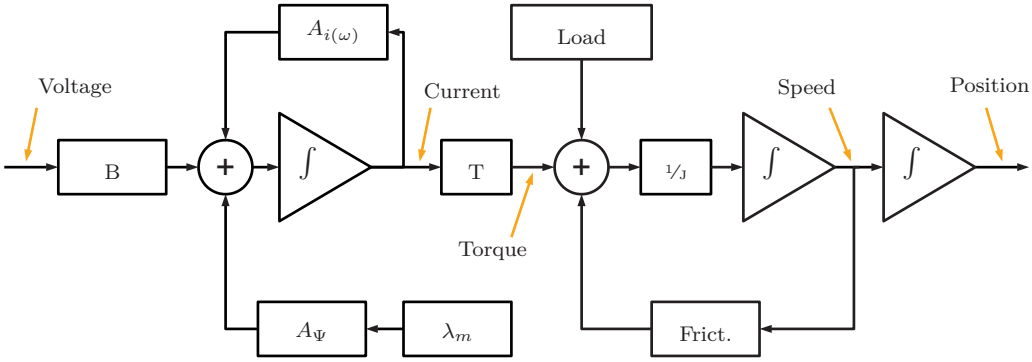

Fig. 4.3: Motor modeling scheme for Simulink.

be subsequently modified into state space description form (4.21).

$$\frac{\mathrm{d}\boldsymbol{i}_{dq123}}{\mathrm{d}t} = \boldsymbol{A}_i(\omega_e)\boldsymbol{i}_{dq123} + \boldsymbol{B}\boldsymbol{u}_{dq123} + \boldsymbol{A}_\Psi\lambda_m \tag{4.21}$$

This form is suitable for modelling. Simulink modeling scheme related to the state space description is shown in figure 4.3.

The matrix $\boldsymbol{A}_\Psi$ reflects influence of back electromotive force (back-EMF). The matrix $\boldsymbol{B}$ relates the currents time derivatives with input voltages $\boldsymbol{u}_{dq123}$. It is called system input matrix. This matrix also shows an input mutual linkage between sub-systems. Matrix $\boldsymbol{B}$ is defined by (4.22). This matrix also shows an input mutual linkage between sub-systems.

$$\boldsymbol{B} = \begin{bmatrix} \sigma_4 & 0 & \sigma_2 & 0 & \sigma_2 & 0 \\ 0 & \sigma_3 & 0 & \sigma_1 & 0 & \sigma_1 \\ \sigma_2 & 0 & \sigma_4 & 0 & \sigma_2 & 0 \\ 0 & \sigma_1 & 0 & \sigma_3 & 0 & \sigma_1 \\ \sigma_2 & 0 & \sigma_2 & 0 & \sigma_4 & 0 \\ 0 & \sigma_1 & 0 & \sigma_1 & 0 & \sigma_3 \end{bmatrix} \tag{4.22}$$

$$\sigma_1 = -\frac{M_{qq}}{L_q^2 + L_q M_{qq} - 2M_{qq}^2} \qquad \sigma_2 = -\frac{M_{dd}}{L_d^2 + L_d M_{dd} - 2M_{dd}^2}$$

$$\sigma_3 = \frac{L_q + M_{qq}}{L_q^2 + L_q M_{qq} - 2M_{qq}^2} \qquad \sigma_4 = \frac{L_d + M_{dd}}{L_d^2 + L_d M_{dd} - 2M_{dd}^2}$$

Matrix $\boldsymbol{B}$ shows that d-axis voltages influence only d-axis currents. This is also true for q-axis quantities. Absence of mutual coupling between axes comes from equation (4.19).

Cross-coupling between the sub-systems is reflected by matrix $\boldsymbol{A}_i(\omega_e)$. Mutual coupling between sub-systems is caused by mutual inductances. The matrix $\boldsymbol{A}_i(\omega_e)$ is a feedback matrix of links between individual currents and their time derivatives. The matrix has the following form (4.23).

$$\boldsymbol{A}_i(\omega_e) = \begin{bmatrix} \sigma_8 & \sigma_6 & \sigma_4 & \sigma_2 & \sigma_4 & \sigma_2 \\ \sigma_5 & \sigma_7 & \sigma_1 & \sigma_3 & \sigma_1 & \sigma_3 \\ \sigma_4 & \sigma_2 & \sigma_8 & \sigma_6 & \sigma_4 & \sigma_2 \\ \sigma_1 & \sigma_3 & \sigma_5 & \sigma_7 & \sigma_1 & \sigma_3 \\ \sigma_4 & \sigma_2 & \sigma_4 & \sigma_2 & \sigma_8 & \sigma_6 \\ \sigma_1 & \sigma_3 & \sigma_1 & \sigma_3 & \sigma_5 & \sigma_7 \end{bmatrix}$$

$$\begin{aligned} \sigma_1 &= \frac{\omega_e(L_d M_{qq} - L_q M_{dd})}{L_q^2 + L_q M_{qq} - 2M_{qq}^2} & \sigma_5 &= -\frac{\omega_e(L_d L_q + L_d M_{qq} - 2M_{dd} M_{qq})}{L_q^2 + L_q M_{qq} - 2M_{qq}^2} \\ \sigma_2 &= \frac{\omega_e(L_d M_{qq} - L_q M_{dd})}{L_d^2 + L_d M_{dd} - 2M_{dd}^2} & \sigma_6 &= \frac{\omega_e(L_q L_d + L_q M_{dd} - 2M_{dd} M_{qq})}{L_d^2 + L_d M_{dd} - 2M_{dd}^2} \\ \sigma_3 &= \frac{M_{qq} R}{L_q^2 + L_q M_{qq} - 2M_{qq}^2} & \sigma_7 &= -\frac{L_q R + M_{qq} R}{L_q^2 + L_q M_{qq} - 2M_{qq}^2} \\ \sigma_4 &= \frac{M_{dd} R}{L_d^2 + L_d M_{dd} - 2M_{dd}^2} & \sigma_8 &= -\frac{L_d R + M_{dd} R}{L_d^2 + L_d M_{dd} - 2M_{dd}^2} \end{aligned} \tag{4.23}$$

This feedback state matrix contains nonlinear components in the presence of electrical speed ω_e.

The matrix $\boldsymbol{A}_\Psi$ reflects the influence of back-EMF. This matrix in combination with motor voltage constant λ_m defines back-EMF.

$$\begin{gathered} \boldsymbol{A}_\Psi = \begin{bmatrix} 0 & \sigma & 0 & \sigma & 0 & \sigma \end{bmatrix}^\intercal \\ \sigma = \frac{\omega_e(L_q - M_{qq})}{L_q^2 + L_q M_{qq} - 2M_{qq}^2} \end{gathered} \tag{4.24}$$

Torque calculation of triple three-phase motor is another important part for modeling. Torque contribution must be considered from every sub-system. The resulting formula for calculating the torque generated by the motor is given by the following equation (4.25).

$$\begin{aligned} T_e &= \tfrac{3}{2} Pp(\lambda_m(i_{q1} + i_{q2} + i_{q3}) + (i_{d1} i_{q1} + i_{d2} i_{q2} + i_{d3} i_{q3})(L_d - L_q) + \\ &+ (i_{d1} i_{q2} + i_{d2} i_{q1} + i_{d1} i_{q3} + i_{d3} i_{q1} + i_{d2} i_{q3} + i_{d3} i_{q2})(M_{dd} - M_{qq})) \end{aligned} \tag{4.25}$$

The electrical angular acceleration ε_e of the rotor is time derivative of electrical speed ω_e and it depends on moment of inertia J and on resulting torque connected

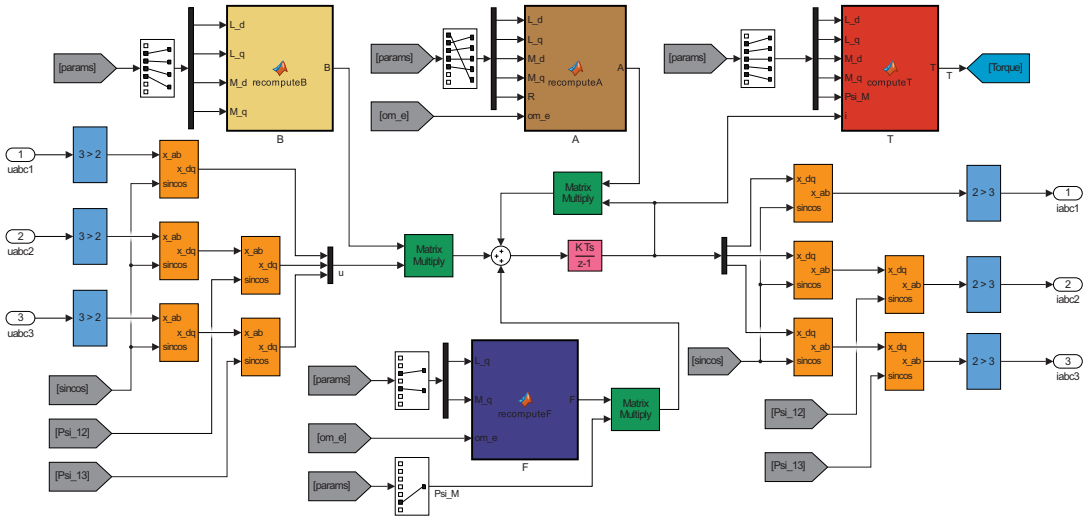

Fig. 4.4: Motor modeling scheme for Simulink.

to the rotor. The resulting torque is given as a sum of the motor torque T_e, the load torque T_l and the friction torque T_{fr}

$$\varepsilon_e = \frac{\mathrm{d}\omega_e}{\mathrm{d}t} = \frac{\mathrm{d}^2\theta}{\mathrm{d}t^2} = \frac{1}{J}(T_e - T_l - T_{fr}) \tag{4.26}$$

As it can be seen from Fig. 4.3, the friction torque is assumed to be proportional to the speed but has opposite direction. The equation (4.26) represents the mechanical part of the motor model (having electrical rotor position θ and speed ω_e as state variables) and together with the equation (4.21) they form complete non-linear electro-mechanical motor model with eight state variables.

The complete modeling scheme in dq coordinates for triple three-phase motor is shown in Fig. 4.4

4.2.3 Transformation of triple three-phase motor parameters to *dq* coordinates

The model as presented above requires that motor parameters are transformed into dq coordinates. The transformation parameters of multiple three-phase motor from stator abc coordinates into dq coordinates are similar to the transformation presented in chapter 4.2.1.

The equation (4.6) describes the electrical part of the motor in abc coordinates. Similar equation can be also formed for multiple three-phase motor.

$$\boldsymbol{u}_{abc1} = \boldsymbol{R}_{abc1}\boldsymbol{i}_{abc1} + \frac{d\boldsymbol{L}_{abc1}\boldsymbol{i}_{abc1}}{dt} + \frac{d\boldsymbol{M}_{abc12}\boldsymbol{i}_{abc2}}{dt} + \frac{d\boldsymbol{M}_{abc13}\boldsymbol{i}_{abc3}}{dt} + \boldsymbol{e}_{abc1} \tag{4.27}$$

The transformation into dq coordinates needs to be implemented individually for each sub-system. All motor currents can not be transformed into one set of dq currents due to electrical separation as already mentioned. Currents of every sub-system are transformed into one set of dq currents. Transformation matrix (4.28) required to transform multiple three-phase motor parameters into dq coordinates consists of several transformation matrices [9]. Transformation matrix of each sub-system depends on electrical shift between stator reference (α) and sub-system phase i (θ_i). Electrical shift between phases within sub-systems is typically $2\pi/3$ radians.

$$\boldsymbol{T}_{abc\rightarrow dq_{123}} = \begin{bmatrix} \boldsymbol{T}_{dq_1}\boldsymbol{T}_{\alpha\beta_1} & \mathbf{0} & \mathbf{0} \\ \mathbf{0} & \boldsymbol{T}_{dq_2}\boldsymbol{T}_{\alpha\beta_2} & \mathbf{0} \\ \mathbf{0} & \mathbf{0} & \boldsymbol{T}_{dq_3}\boldsymbol{T}_{\alpha\beta_3} \end{bmatrix} \tag{4.28}$$

Inverse transformation for triple three-phase motor consists of inverse transformations for each sub-system. Inverse transformation is shown by equation (4.29)

$$\boldsymbol{T}^{-1}_{abc\rightarrow dq_{123}} = \begin{bmatrix} \boldsymbol{T}^{-1}_{\alpha\beta_1}\boldsymbol{T}^{-1}_{dq_1} & \mathbf{0} & \mathbf{0} \\ \mathbf{0} & \boldsymbol{T}^{-1}_{\alpha\beta_2}\boldsymbol{T}^{-1}_{dq_2} & \mathbf{0} \\ \mathbf{0} & \mathbf{0} & \boldsymbol{T}^{-1}_{\alpha\beta_3}\boldsymbol{T}^{-1}_{dq_3} \end{bmatrix} \tag{4.29}$$

$\boldsymbol{i}_{dq_{123}}$ for triple three-phase motor has three d and three q components $\boldsymbol{i}_{dq_{123}} = [i_{d1}i_{q1}i_{d2}i_{q2}i_{d3}i_{q3}]^\intercal$. The voltage vector has components distributed similarly. $\boldsymbol{u}_{dq_{123}} = [u_{d1}u_{q1}u_{d2}u_{q2}u_{d3}u_{q3}]^\intercal$. The voltage equation can be transformed into dq coordinates using transformation matrices (4.28) and (4.29).

$$\begin{aligned} \boldsymbol{u}_{dq_{123}} = \; & \boldsymbol{T}_{abc\rightarrow dq_{123}}\boldsymbol{R}_{abc_{123}}\boldsymbol{T}^{-1}_{abc\rightarrow dq_{123}}\boldsymbol{i}_{dq_{123}} \\ & + \boldsymbol{T}_{abc\rightarrow dq_{123}}\frac{\mathrm{d}\boldsymbol{L}_{abc_{123}}\boldsymbol{T}^{-1}_{abc\rightarrow dq_{123}}\boldsymbol{i}_{dq}}{\mathrm{d}t} + \boldsymbol{T}_{abc\rightarrow dq_{123}}\boldsymbol{e}_{abc_{123}} \end{aligned} \tag{4.30}$$

Inductances of symmetrical triple three-phase motor can be transformed into dq coordinates. Different L_d and L_q reflect inductance fluctuation. If the inductance fluctuation of individual coils has the same amplitude and the phase shift is equal to electrical shift of motor coils ($^{2\pi}/_{3}$ radians for symmetrical three-phase sub-systems), inductances fluctuation are transformed into constants. Another criterium for transformation to constant dq inductances depends on inductances DC component symmetry. Self inductances and mutual inductances of each coil pair within sub-system need to be same. Similar conditions are also important for mutual inductances between sub-systems. If all conditions are fulfilled, inductances can be recalculated to dq coordinates and resulting inductances in dq coordinates become constants.

Reached matrix L_{dq} contains also mutual couplings between d and q coordinates. These mutual inductances depend on electrical shift between sub-systems. The

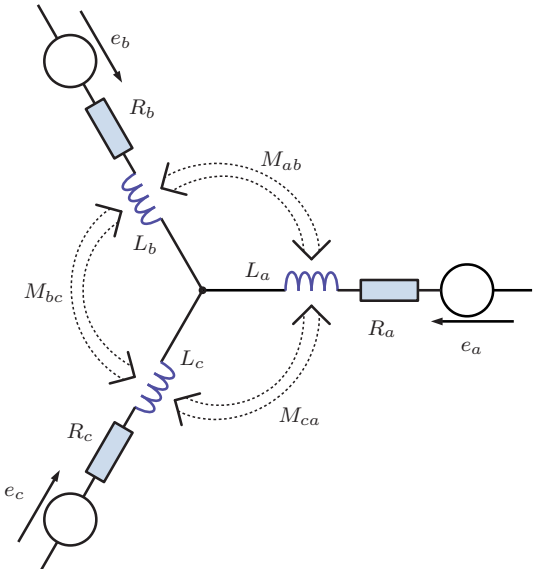

Fig. 4.5: Three-phase electric equivalent circuit.

motor construction without coupling between d and q coordinates is not typical. Such behaviour significantly reduces usability of motor models in dq coordinates.

The presented dq coordinates model shown here can be extended and mutual inductance between d and q axis can be added. The equation (4.19) needs to be changed and all other equations modified according to new flux equations.

This is why the motor model in abc coordinates is more suitable for multiple three-phase motor arrangements. This model can be also implemented in MATLAB/Simulink. The fault simulation using model implemented in stator abc coordinates is simpler and more straightforward in comparison to a fault simulation using the model in rotor dq coordinates.

4.3 Simulink *abc* coordinates model

Three-phase motor model calculated in stator abc coordinates is based on equation (4.6). This equation for three-phase motor has the following form (4.31).

$$\boldsymbol{u}_{abc} = \boldsymbol{R}_{abc}\boldsymbol{i}_{abc} + \frac{\mathrm{d}\boldsymbol{L}_{abc}\boldsymbol{i}_{abc}}{\mathrm{d}t} + \boldsymbol{e}_{abc} \tag{4.31}$$

Voltage vector u_{abc} represents motor terminals voltages. Motor terminal voltages are related to the motor middle point voltage. Electric equivalent scheme for three phase motor is shown Fig. 4.5.

The resistance of all phases R_a, R_b and R_c must be the same for symmetrical motor. Same condition needs to be met for windings inductances L_a, L_b, L_c and

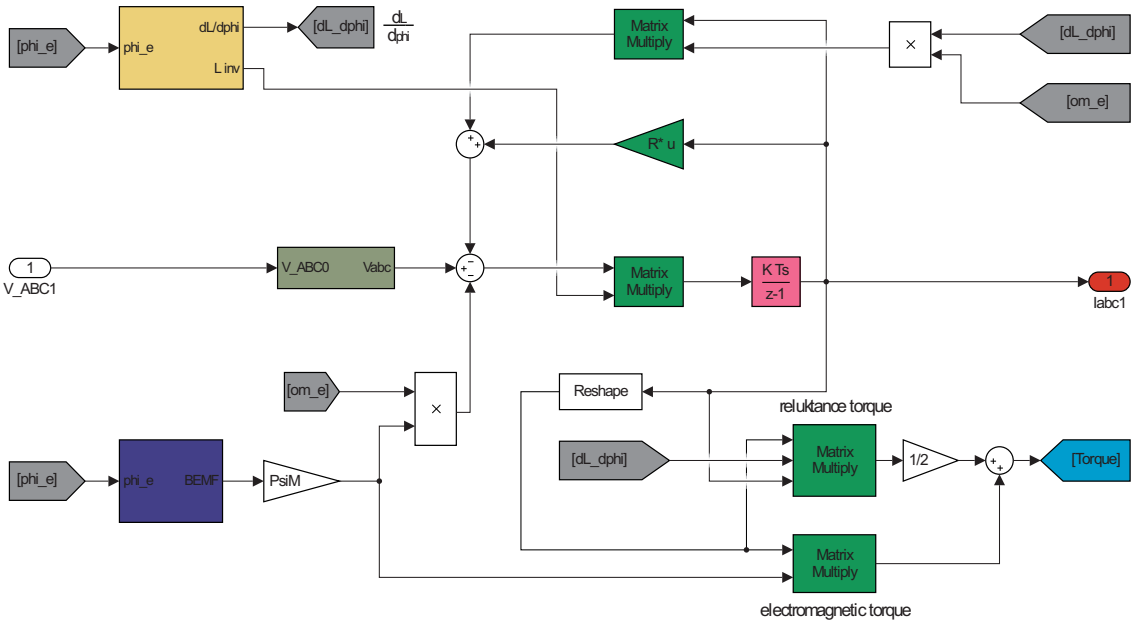

Fig. 4.6: Fully balanced triple three-phase motor modeling scheme.

mutual inductances M_{ab}, M_{bc}, M_{ca}. Symmetry condition is typically fulfilled by the three-phase motor constructions, though not all sub-systems of multiple three-phase motor constructions are fully symmetrical [26].

The actual motor currents represent the state variables. Motor current derivatives are required for modeling. The current derivatives are described in the following equation (4.32)

$$\frac{\mathrm{d}\boldsymbol{i}_{abc}}{\mathrm{d}t} = \boldsymbol{L}_{abc}^{-1}\left(\boldsymbol{u}_{abc} - \boldsymbol{R}_{abc}\boldsymbol{i}_{abc} - \omega_e \frac{\mathrm{d}\boldsymbol{L}_{abc}}{\mathrm{d}\theta}\boldsymbol{i}_{abc} - \boldsymbol{e}_{abc}\right) \tag{4.32}$$

The sum of all three currents is equal to zero during standard operation condition according to Kirchhoffs Circuit Law. The sum of current derivatives is also equal to zero. This condition is described by the equation(4.33). Current leakage can be caused by winding connection to the motor case, however, this behaviour is defined as fault state.

$$\sum_{n=a,b,c} \boldsymbol{i}_n = \sum_{n=a,b,c} \frac{\mathrm{d}\boldsymbol{i}_n}{\mathrm{d}t} = 0 = \begin{bmatrix}1 & 1 & 1\end{bmatrix} \frac{\mathrm{d}\boldsymbol{i}_{abc}}{\mathrm{d}t} \tag{4.33}$$

The middle point voltage is equal to the arithmetic average of motor terminal voltages. This condition is satisfied for fully symmetric motor. Thus individual phase voltages can be calculated. Simulink model scheme for symmetric three-phase motor is shown in Fig. 4.6.

This modeling scheme uses arithmetic average as middle point voltage. The middle point voltage is subtracted from each element of voltage vector by dark green

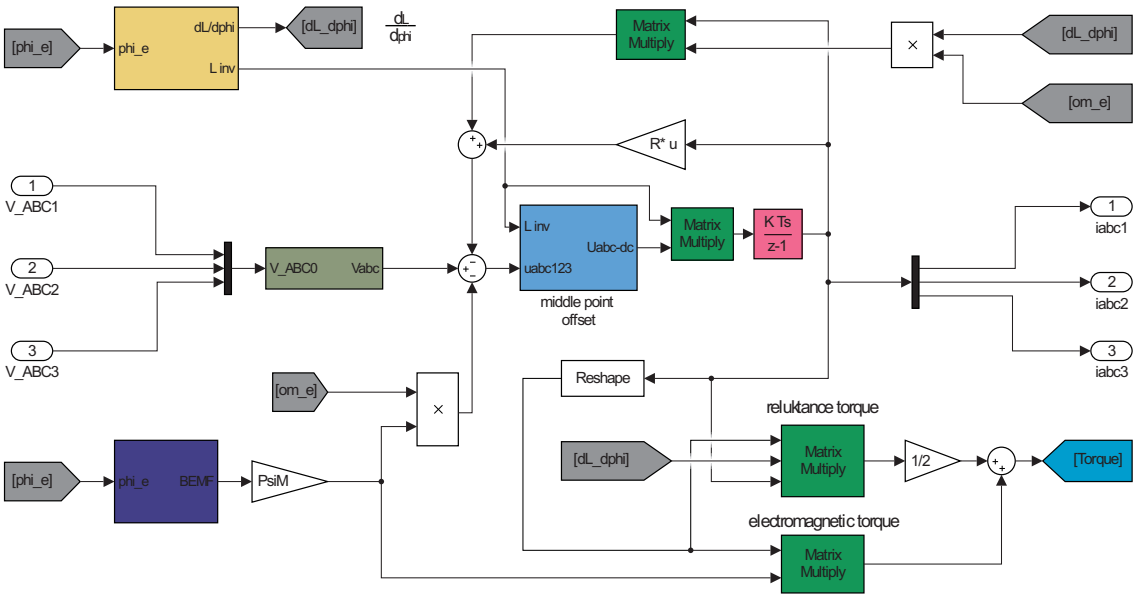

Fig. 4.7: Triple three-phase motor modeling scheme with middle point voltage calculation.

block. Yellow block of modeling scheme calculates actual motor inductances. An inductance matrix inversion is required as seen in the equation (4.32). The inversion is calculated in this block as well. Inductances and mutual inductances are function of rotor position. Derivative of inductance with respect to rotor position is also calculated by this block.

Blue block in combination with additional multiplications calculate back-EMF voltage as actual rotor angle function. Torque generated by motor is calculated using equation (4.34)

$$T_e = Pp\left(\frac{1}{2}\boldsymbol{i}_{abc}^{\mathsf{T}}\frac{d\boldsymbol{L}_{abc}}{d\theta}\boldsymbol{i}_{abc} + \frac{\boldsymbol{i}_{abc}^{\mathsf{T}}\boldsymbol{e}_{abc}}{\omega_e}\right) \tag{4.34}$$

The model of symmetrical motor can be implemented in dq coordinates. Motor middle point voltage cannot be calculated as motor terminal voltages average for an asymmetrical motor arrangement. The asymmetry in motor inductances or windings resistance causes problems with the sum of currents (4.33). The middle point voltage u_m which guarantee the zero sum of phase currents for three-phase motor can be added to the equation (4.32). The resulting equation (4.35) describes calculation of middle point voltage for asymmetry three-phase motor. One middle point voltage

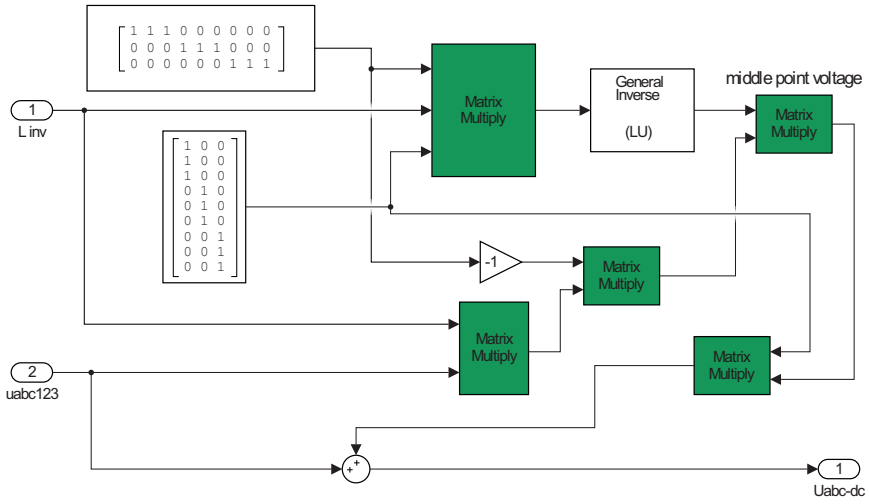

Fig. 4.8: Triple three-phase motor middle junction voltage compensation.

is calculated for three-phase motor. $\boldsymbol{u}^c_{abc}$ as substitution.

$$0 = \begin{bmatrix}1 & 1 & 1\end{bmatrix} \frac{d\boldsymbol{i}_{abc}}{dt} = \begin{bmatrix}1 & 1 & 1\end{bmatrix} \boldsymbol{L}^{-1}_{abc} \left(\boldsymbol{u}^c_{abc} + \begin{bmatrix}1\\1\\1\end{bmatrix} u_m \right)$$

$$u_m = -\frac{\begin{bmatrix}1 & 1 & 1\end{bmatrix} \boldsymbol{L}^{-1}_{abc} \boldsymbol{u}^c_{abc}}{\begin{bmatrix}1 & 1 & 1\end{bmatrix} \boldsymbol{L}^{-1}_{abc} \begin{bmatrix}1\\1\\1\end{bmatrix}} \tag{4.35}$$

$$\text{where} \qquad \boldsymbol{u}^c_{abc} = \boldsymbol{u}_{abc} - \boldsymbol{R}_{abc}\boldsymbol{i}_{abc} - \omega_e \frac{d\boldsymbol{L}_{abc}}{d\theta}\boldsymbol{i}_{abc} - \boldsymbol{e}_{abc}$$

The voltage equation for triple three-phase motor (4.36) is similar to the three-phase motor equation. The middle point voltage is given by the motor electrical connection. $\boldsymbol{u}_{m_{123}}$ represents a middle point voltage vector. This vector consists of three middle point voltages. One for each middle junction. $\boldsymbol{u}_{m_{123}} = [u_{m1}\ u_{m1}\ u_{m1}\ u_{m2}\ u_{m2}\ u_{m2}\ u_{m3}\ u_{m3}\ u_{m3}]^\intercal$

$$\boldsymbol{u}_{abc_{123}} = \boldsymbol{R}_{abc_{123}}\boldsymbol{i}_{abc_{123}} + \frac{\mathrm{d}\boldsymbol{L}_{abc_{123}}\boldsymbol{i}_{abc_{123}}}{\mathrm{d}t} + \boldsymbol{e}_{abc_{123}} + \boldsymbol{u}_{m_{123}} \tag{4.36}$$

The middle point voltage for triple three-phase motor can be calculated using similar equation (4.37). One middle point voltage u_m is calculated for each three-phase sub-system. The middle point voltages cannot be calculated individually for each sub-system due to mutual inductances.

Light blue block of triple three-phase modeling scheme 4.7 calculates the middle point voltages. Figure 4.8 shows internal structure of the modeling scheme for the middle point voltages calculation. Middle point voltages are subsequently added to the voltage vector.

$$\begin{bmatrix}0\\0\\0\end{bmatrix} = \begin{bmatrix}1&1&1&0&0&0&0&0&0\\0&0&0&1&1&1&0&0&0\\0&0&0&0&0&0&1&1&1\end{bmatrix} \boldsymbol{L}_{abc_{123}}^{-1} \left(\boldsymbol{u}_{abc_{123}}^{c} + \begin{bmatrix}1&0&0\\1&0&0\\1&0&0\\0&1&0\\0&1&0\\0&1&0\\0&0&1\\0&0&1\\0&0&1\end{bmatrix} \begin{bmatrix}u_{m1}\\u_{m2}\\u_{m3}\end{bmatrix} \right)$$

$$\begin{bmatrix}u_{m1}\\u_{m2}\\u_{m3}\end{bmatrix} = - \left(\begin{bmatrix}1&0&0\\1&0&0\\1&0&0\\0&1&0\\0&1&0\\0&1&0\\0&0&1\\0&0&1\\0&0&1\end{bmatrix}^{\mathsf{T}} \boldsymbol{L}_{abc_{123}}^{-1} \begin{bmatrix}1&0&0\\1&0&0\\1&0&0\\0&1&0\\0&1&0\\0&1&0\\0&0&1\\0&0&1\\0&0&1\end{bmatrix} \right)^{-1} \left(\begin{bmatrix}1&0&0\\1&0&0\\1&0&0\\0&1&0\\0&1&0\\0&1&0\\0&0&1\\0&0&1\\0&0&1\end{bmatrix}^{\mathsf{T}} \boldsymbol{L}_{abc_{123}}^{-1} \boldsymbol{u}_{abc_{123}}^{c} \right) \tag{4.37}$$

$$\textit{where} \qquad \boldsymbol{u}_{abc_{123}}^{c} = \boldsymbol{u}_{abc_{123}} - \boldsymbol{R}_{abc_{123}} \boldsymbol{i}_{abc_{123}} - \omega_e \frac{d\boldsymbol{L}_{abc_{123}}}{d\theta} \boldsymbol{i}_{abc_{123}} - \boldsymbol{e}_{abc_{123}}$$

The *abc* model is suitable for both, symmetrical and asymmetrical structures. Fault simulation can be problematic when using *abc* model. Classical Simulink models operate with inputs and outputs. The signal cannot flow in the opposite way. Causality is clearly defined in this type of models. All input voltages need to be defined for simulation.

Some inverter faults can cause phase connection to positive or negative DC-link voltage. This type of fault can be easily modeled without modeling scheme modification by configuring corresponding input voltage. Open-circuit faults allow zero currents through phase. This fault can be generated by increased winding resistance of damaged phase. Another motor faults with inter-turn short-circuits or phase connection to motor case cannot be modeled.

Disconnection of damaged sub-system from inverter can be also problematic. The sub-system disconnection can be generated by increasing windings resistance of

whole sub-system. However, faulty sub-system of motor generates voltages. Thus current can flow from motor to inverter. Sub-system voltage should be the output variable of the motor model during fault state for this reason. In classical Simulink model the variable cannot be changed from input to output.

4.4 The Simscape *abc* coordinates model

The Simscape allows to build physical component models based on physical connections that directly integrate with block diagrams and other modeling paradigms. Individual Simscape components interact with each other. This mutual interaction between blocks allows dynamically change model causality. Each Simscape block consists of equations which describe physical behaviour of component. Equations are automatically processed during model compilation process.

The motor converts electrical energy into the mechanical rotating energy. The mechanical rotating component as the moment of inertia or friction block can be used to create the simple model of motor mechanical part. The motor connection to complex mechanical model is also possible. The Simscape interface allows for complex modeling schemes to be created. The Simscape also allows to create complex models with temperature dependencies. For example, motor cooling system and thermal dependencies can be modeled using this modeling mechanism.

Power sources, switches and other electronic components are prepared in basic Simscape library. Electrical switch can be used to disconnect one phase for example. External faults (inverter faults or power-lines faults) can be simulated with simple Simscape motor model. Modeling of internal motor faults requires extended model structure.

The Simscape allows to define custom blocks and describe physical behaviour of this model by set of equations. Equations can be used directly in matrix form to increase model source code transparency. Already mentioned motor equations for triple three-phase motor (4.36) or general multi-phase motor (4.6) can be used to define custom Simscape blocks behaviour. Equation (4.7) can be used to calculate motor torque in *abc* coordinates.

The equation (4.36) describes behaviour of nine motor coils. This equation can be used directly to create simple Simscape model of triple three-phase motor. Electrical connection of this motor is shown in figure 4.9. Middle point voltage which causes problem in case of asymmetry using classical Simulink model is automatically solved by electrical connection of coils in Simscape model. Electrical and mechanical connection of Simscape block can be seen in figure 4.10. Middle point junctions are visible in this figure. Sum of all currents is equal to zero according to Kirchhoffs

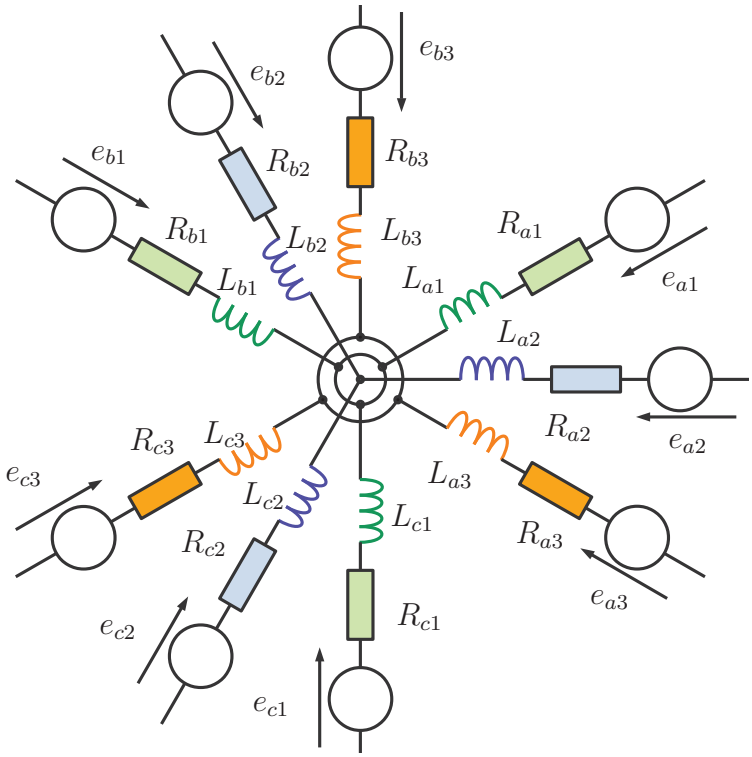

Fig. 4.9: Electrical scheme of triple three-phase motor.

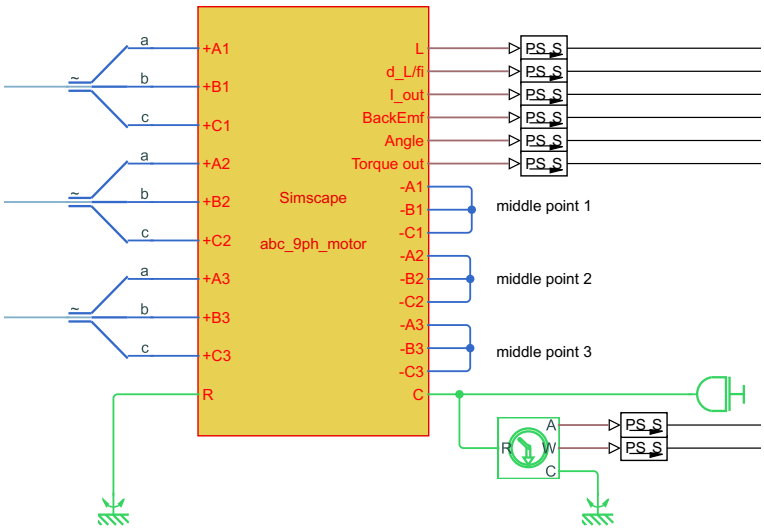

Fig. 4.10: Simple triple three-phase Simscape model.

circuit law. General multi-phase motor model can be also very simply implemented using Simscape.

The model operates internally with phase to phase voltages. Physical variables of model, for example middle point voltage, can be measured using Simscape sensors

which are part of fundamental Simscape library. The middle point can be also connected to negative or positive DC-link to simulate connected middle point to motor case. However windings of real motor can be connected to motor case in a random place. A single winding can be separated into two serially connected windings. Serial connection of the coils has the same behaviour as original coil. This principle is demonstrated in figure 4.11. Voltage potential of any place of original coil can be subsequently used to simulate electrical fault.

The variable M represents mutual inductance between coils L and other motor windings. R represents windings resistance. Variable e denotes influence of back-EMF voltage to windings. Parameter σ represents dividing ratio. The position of fault join can be customised using this parameter. Middle point of serial connected coils can be connected to any voltage potential. This method can be used to simulate windings connection to motor case, or even mutual connection between two motor phases. Interturn short-circuit can be also easily simulated. Coil splitting process is demonstrates by the following equation (4.38).

$$\begin{gathered} u = Ri + \frac{\mathrm{d}Li}{\mathrm{d}t} + e \\ \begin{bmatrix} u_{1\_1} \\ u_{1\_2} \end{bmatrix} = \begin{bmatrix} R_{1\_1} & 0 \\ 0 & R_{1\_2} \end{bmatrix} \begin{bmatrix} i_{1\_1} \\ i_{1\_2} \end{bmatrix} + \frac{\mathrm{d} \begin{bmatrix} \sigma^2 L & \sigma(1-\sigma)L \\ \sigma(1-\sigma)L & (1-\sigma)^2 L \end{bmatrix} \begin{bmatrix} i_{1\_1} \\ i_{1\_2} \end{bmatrix}}{\mathrm{d}t} + \begin{bmatrix} e_{1\_1} \\ e_{1\_2} \end{bmatrix} \end{gathered} \tag{4.38}$$

Demonstrated process is used to extend nine equations written in matrix form (4.36) into twelve equations required by extended model. Three windings in two sub-systems are split into serial connected coils. Electrical scheme of the extended model is shown in Fig. 4.12. Equation (4.39) reflects the behaviour of extended Simscape model.

$$\boldsymbol{u}^e_{abc_{123}} = \boldsymbol{R}^e_{abc_{123}} \boldsymbol{i}^e_{abc_{123}} + \frac{\mathrm{d}\boldsymbol{L}^e_{abc_{123}} \boldsymbol{i}^e_{abc_{123}}}{\mathrm{d}t} + \boldsymbol{e}^e_{abc_{123}} \tag{4.39}$$

The individual matrices for extended model are calculated from parameters of triple three-phase motor. Split ratio for phases a_1 a_2 and c_1 can be configured by

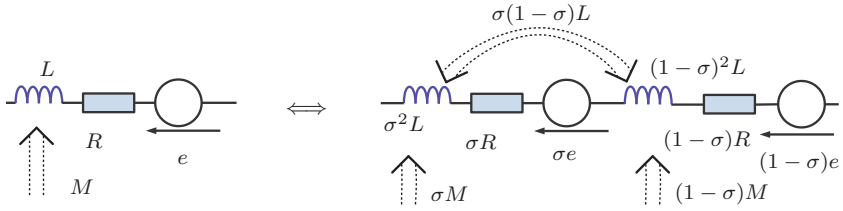

Fig. 4.11: Winding equivalent for extended motor model.

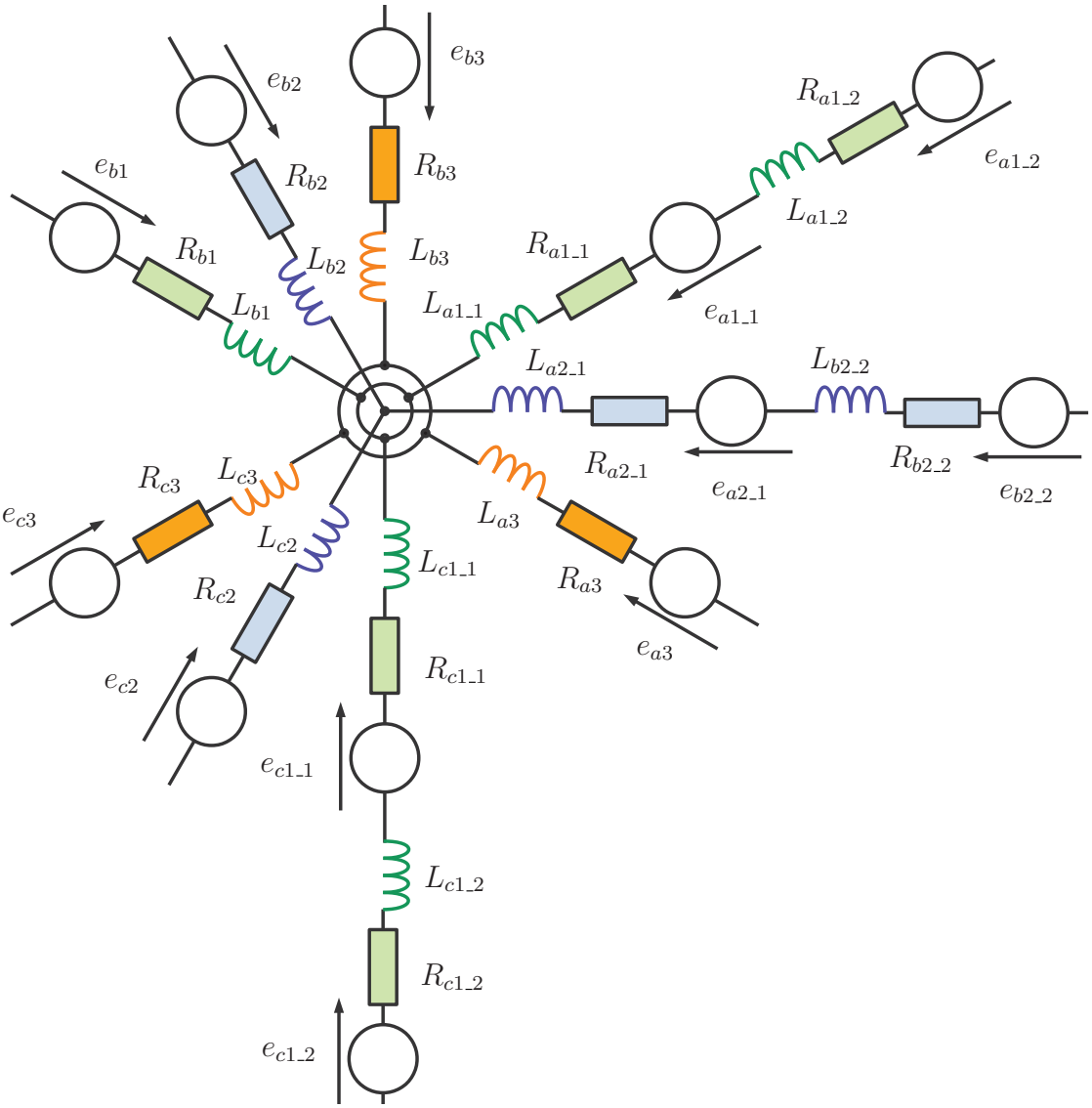

Fig. 4.12: Electrical scheme for triple three-phase motor adapted to faults modeling.

parameters σ_1 σ_2 and σ_3. These parameters are used to transform triple three-phase motor parameters into extended model parameters. Appendix A shows detailed form of matrixes.

Inductances for extended model are recalculated from inductance constant value L_{s_i}, inductance fluctuation amplitude $L_{\Delta m_i}$ and phase shift L_{p_i}. These variables can be set for every self inductance and mutual inductance independently. Each element of the inductance matrix $\boldsymbol{L}^{e}_{abc_{123}}$ is calculated by the following equation (4.40).

$$L_i = L_{s_i} + L_{\Delta m_i} \cos(2 * \theta + L_{p_i}) \tag{4.40}$$

The model can be used for motors with different coil geometrical arrangement.

The variable L_{p_i} includes also phase shift between stator reference and individual winding. The amplitude of back-EMF voltage is the same for every motor phase. Phase angle of back-EMF voltage can be configured individually for each winding. The phase shift between coils within one sub-system can be also customized for this reason.

Extended motor model uses the serial connection of two coils for phase winding instead of one simple coil. This method is required to simulate an interturn short-circuit and other motor internal faults. Fault can be generated during normal motor run using switches. The transient state is also simulated using this method. All realised control algorithm tests and motor simulations use the already mentioned Simscape motor model. Dual three-phase motor uses similar model without the last sub-system.

5 MULTI-PHASE MOTOR STRUCTURES

The motor behaviour depends on motor parameters. Mutual inductances and motor symmetry is defined by the stator construction in particular. The stator can be constructed using several methods. Non-overlapping concentrated winding is one possible arrangement. In this case each coil is rotated around one stator tooth. Individual coils are connected in series or in parallel to create phase windings A, B and C for three-phase motors, with the correct number of pole-pairs and phase shifts. Back-EMF waveforms are displaced by 120 electrical degrees. Dual or triple three-phase motor can be also created easily using this method. Coils are evenly distributed into individual sub-systems. The mutual inductances between phases within sub-systems are the same. Back-EMF waveforms are displaced by 120 electrical degrees within individual sub-systems. However, back-EMF phase shift between sub-systems can exist [26].

The advantage of non-overlapping concentrated winding arrangement comes from the low mutual inductances between sub-systems. In this way sub-systems can operate in different operating points without additional compensation. The mutual inductances between sub-systems can improve motor behaviour during some faults. However, mutual inductance can also cause problems during some faults. The motor behaviour during individual faults is analysed in the following section 6.

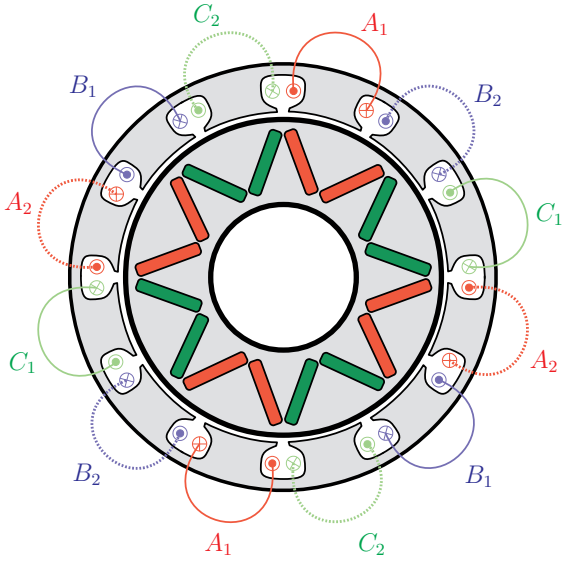

Fig. 5.1: Dual three-phase motor with non-overlapping concentrated winding and interlaced sub-systems.

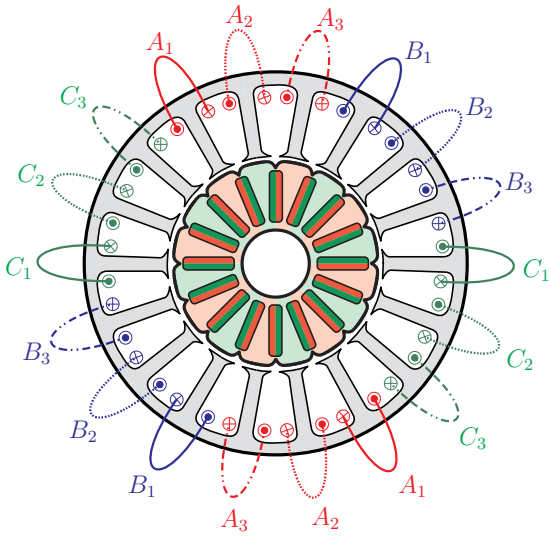

Fig. 5.2: Triple three-phase motor with non-overlapping concentrated winding and interlaced sub-systems.

From the symmetry point of view, individual sub-systems are symmetrical, typically using non-overlapping concentrated winding arrangement. Control algorithms

typically used for three-phase motors can be used for symmetrical structures with little modifications [27] due to low mutual inductances which can be ignored. The phase shift between sub-systems can influence symmetry of the whole system. This asymmetry should be considered during the control algorithm design to reach optimal control algorithm.

The winding factor using non-overlapping concentrated winding is typically lower in comparison with the distributed winding arrangement. This disadvantage can be partially compensated using proper pole-pairs and stator slots numbers combinations. The phase shift between sub-systems can increase the winding factor and increase the power density of the motor in comparison with classical three-phase arrangements [28, 29]. Figures 5.1 and 5.2 show motors with non-overlapping concentrated winding. This arrangement is also defined as the motor with interlaced sub-systems because each coil of the first sub-system is located next to the coil of another one.

The back-EMF voltage generated by non-overlapping concentrated winding arrangement contains harmonic distortion. Proper rotor pole geometry reduces harmonic distortion of back-EMF voltages.

Field weakening index (FWI) is another important parameter of the motor. This parameter is defined as the ratio of the characteristic current I_{ch} over the maximum allowed motor current I_s defined by equation (5.1). I_s is also defined as the motor rated current [30].

$$FWI = \frac{I_{ch}}{I_s} \tag{5.1}$$

The characteristic current I_{ch} is defined as the ratio of magnet flux linkage, λ_m, over d-axis inductance, L_d as shown in equation (5.2).

$$I_{ch} = \frac{\lambda_m}{L_d} \tag{5.2}$$

I_{ch} is also the center of voltage-limit ellipses in the rotor referred dq current plane. The rated current is defined as maximum allowed stator current I_s [31]. The field weakening index defines machine performances in the field weakening area. For instance, when I_{ch} is equal to the rated current of a PM machine (FWI = 1), the constant power region can be extended theoretically to infinite motor speed. The maximum speed of the motor is defined by DC-link voltage for machines with FWI larger than one.

The field weakening index is also important from point of view of failure operation. One motor sub-system can be field weakened completely ($i_d = -i_{ch}$) whereas the second sub-system generates torque. This mechanism can be used during motor

failure. However, the field weakening index needs to be lower than one. Mutual inductances should be also taken into account.

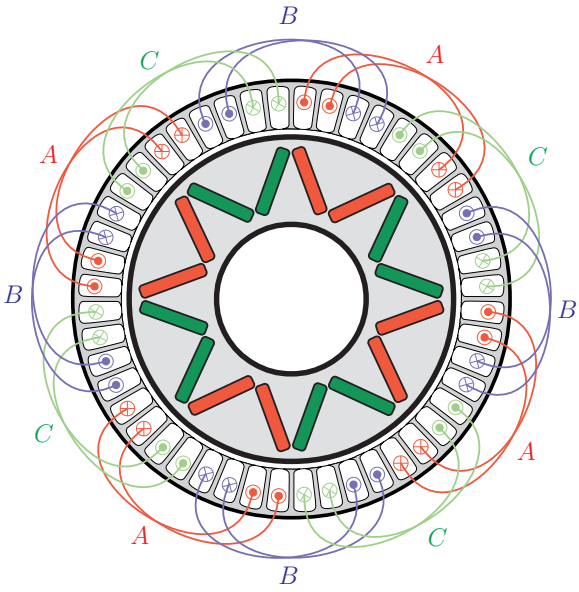

Fig. 5.3: Three-phase motor with distributed winding arrangement.

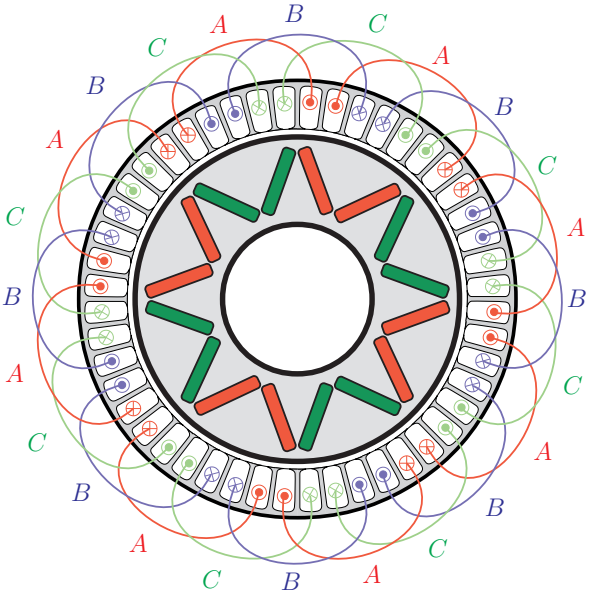

Fig. 5.4: Three-phase motor with distributed winding arrangement.

Second possible stator winding arrangement is distributed winding. Distributed windings produce back-EMF waveforms which are almost sinusoidal in comparison with the concentrated windings arrangement. This windings arrangement is typically used in motor production. Distributed windings are divided into multiple armature slots [32]. One armature slot can contain coils of different phases or even coils of different sub-systems using this arrangement. Mutual inductances between phases are higher in comparison to non-overlapping concentrated winding arrangement. Figures 5.3 and 5.4 shows three-phase stators with distributed windings.

Distributed winding can be also divided into multiple sub-systems to form multiple three-phase systems. Mutual inductances between the coils lead to the motor with strong magnetic coupling between sub-systems. Multiple three-phase system can be created using several methods.

Individual coils can be evenly distributed into multiple sub-systems to form a fully symmetrical structure. The coils of different sub-systems are strongly coupled in this case. Mutual inductances between sub-systems are much higher in comparison to multiple three-phase structure with non-overlapping concentrated windings. Dual three-phase motor with interlaced sub-systems is shown in Figure 5.5. The motor can operate using only one sub-system without any problems during a fault because individual three-phase sub-systems are symmetrical. Mutual inductances between all three phases is same ($M_{ab} = M_{bc} = M_{ca}$). The main disadvantage of

this structure comes from high mutual inductances. Currents of one sub-system influence another sub-system. These effects cause problems during the motor short-circuit faults.

The second method to form multiple three-phase motor uses coil groups. Individual sub-systems are geometrically separated. We can speak about the motor with segregated sub-systems in this case. Mutual inductances between sub-systems are significantly lower in comparison to the interlaced structure. Dual three-phase motor with segregated windings is shown in Figure 5.6. This motor structure can operate during the short-circuit faults of one sub-system. However, control algorithm for this structure is more complex and all asymmetries need to be considered.

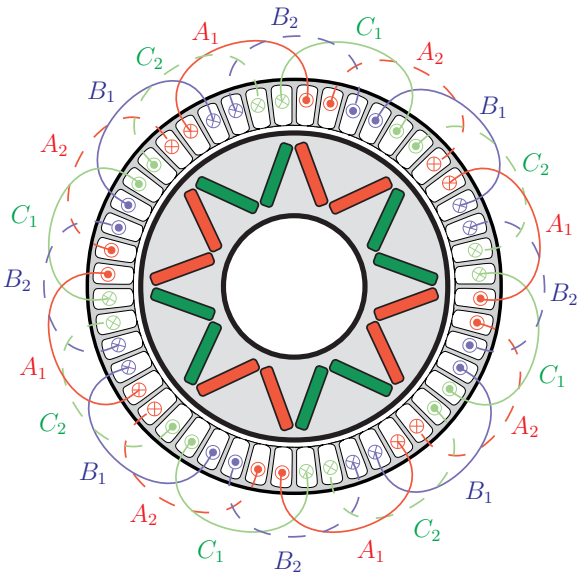

Fig. 5.5: Dual three-phase motor with distributed winding and interlaced sub-systems.

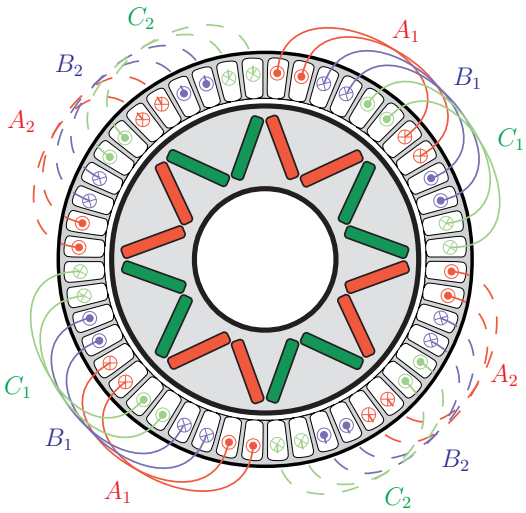

Fig. 5.6: Dual three-phase motor with distributed winding and segregated sub-systems.

The mutual inductances between phases within the sub-system are not the same. The mutual inductances between boundary windings (M_{ac}) are lower in comparison with other inductances within the sub-system (M_{ab}, M_{bc}). This asymmetry causes problems during motor faults. As such, a special algorithm is required for the single sub-system operation. Further problems are caused by asymmetrical mutual inductances between sub-systems.

Individual stator structures can be compared with each other. Simulation results using different structures are shown in the following chapters. Fundamental motor parameters are the same for every stator coil arrangement. The motor parameters are shown in Table 5.1. Test conditions for individual structures are also the same. Different motor behaviour is caused by different inductances.

Tab. 5.1: Fundamental motor parameters

Specification	Symbol	Value
Continuous power	P_c	68 kW
Peak power	P_{pk}	160 kW
Nominal speed	ω_n	8000 rpm
Maximum speed	ω_M	20000 rpm
Maximum continuous current	I_s	120 A (rms)
Maximum current for 10 s	I_m	300 A (rms)
Continuous Torque	T_c	81 Nm
Maximum Torque	T_M	200 Nm
Back-EMF constant	λ_m	40 mV/(rad s^{-1})
Number of pole pairs	Pp	4
Number of phases	p_h	6 (2 $\times$ ⅄)

5.1 The motor with interlaced windings and low mutual inductances

Low mutual inductances between sub-systems can be achieved using non-overlapping concentrated winding. This stator arrangement is shown in Figures 5.1 and 5.2.

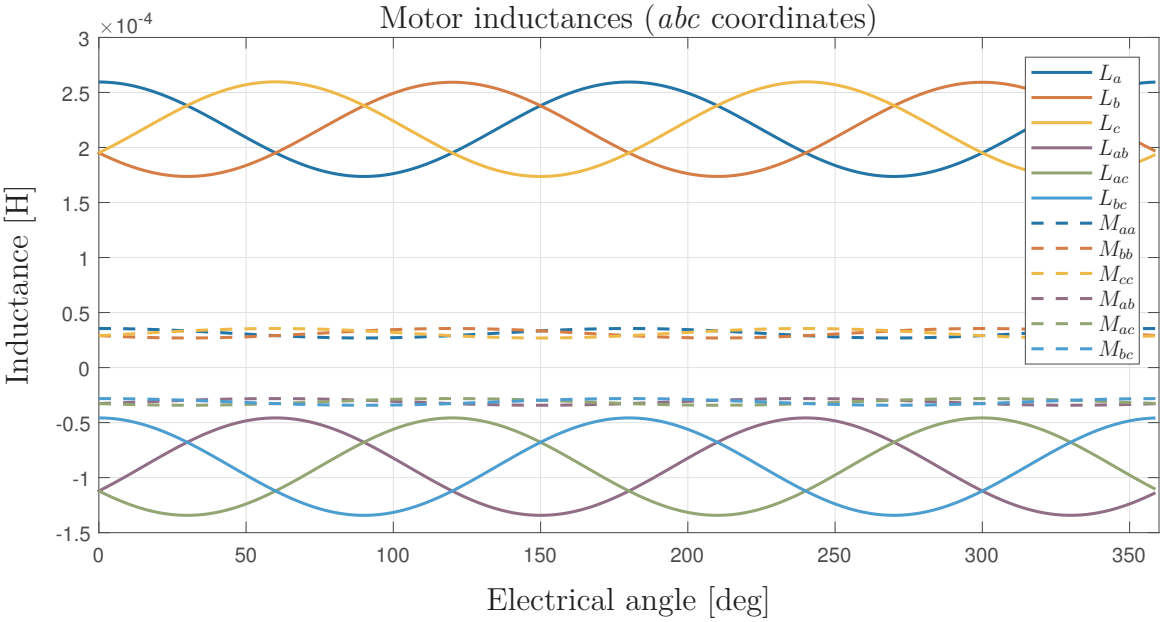

Fig. 5.7: The inductances of analysed dl three-phase motor with low mutual inductances between sub-systems.

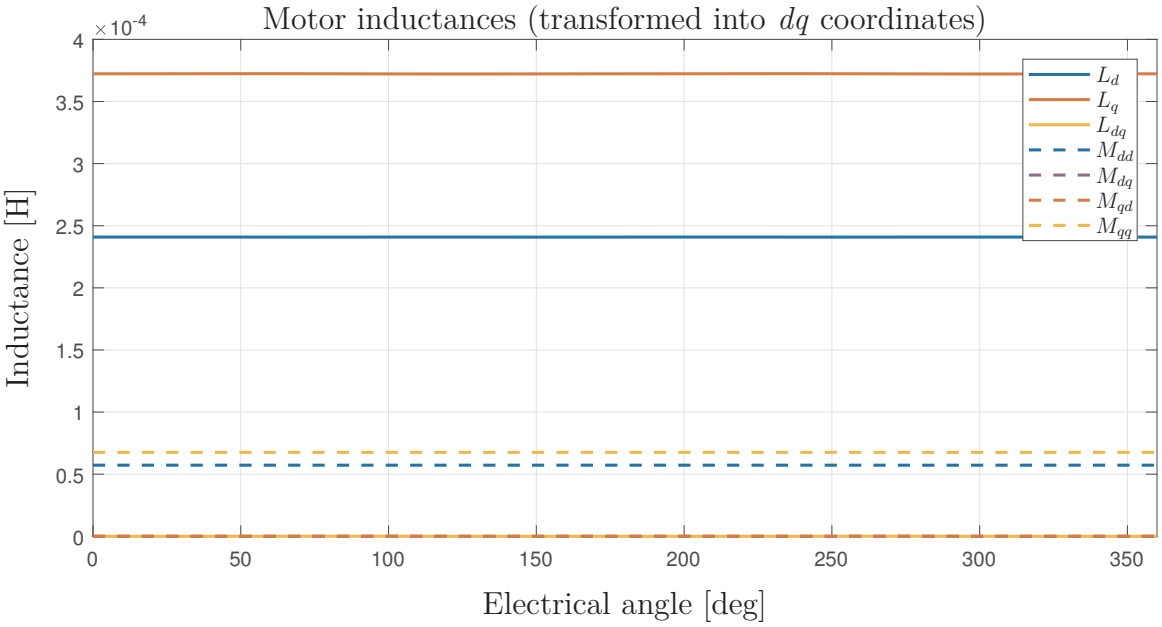

Fig. 5.8: The inductances of analysed dual three-phase motor with low mutual inductances between sub-systems transformed into dq coordinates.

Inductance fluctuation can be seen in Figure 5.7. The fluctuation is caused by rotor geometry. The inductance fluctuation referred to here leads to different L_d and L_q inductances. Motors with different dq inductances can generate reluctance torque. The higher inductance difference leads to higher reluctance torque.

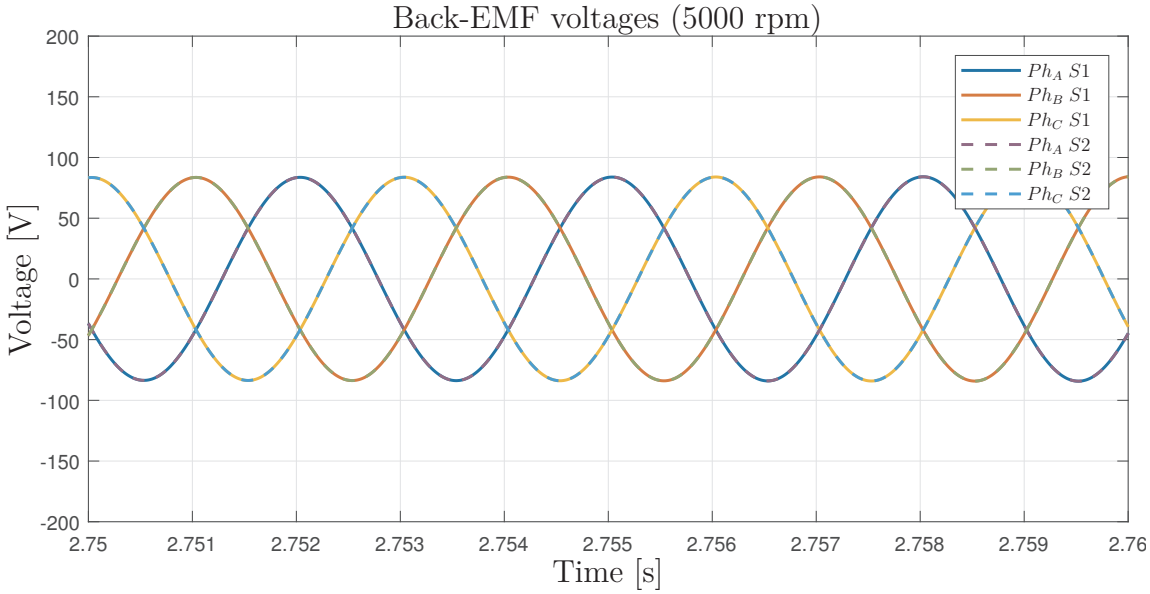

Fig. 5.9: Back-EMF phase voltages of dual three-phase motor with low mutual inductances between sub-systems.

Inductances presented in Figure 5.7 are transformed into dq coordinates and shown in Figure 5.8. q axis inductance is approximately 5.8 µH, However, d axis inductance is only proximately 4.4 µH. Mutual inductances between sub-systems are roughly 20 % of self-inductances and therefore the interaction between sub-systems is very low. Inductances transformed into dq coordinates have zero mutual inductances between d and q axis. The model described in chapter 4.2.2 can be used for this type of motor without modifications for this reason.

The back-EMF voltage of the motor is shown in Figure 5.9. Back-EMF voltages of both sub-systems are the same without the phase shift.

5.1.1 Active short-circuit simulations

The active short-circuit (ASC) mode is very important during motor or inverter faults. For instance one of inverter transistors can be short-circuited. The damaged phase is subsequently connected to negative or positive DC-link voltage. Other phases of the damaged sub-system can be connected to the same potential to reduce the influence of the damaged transistor. The field weakening index of the motor needs to be lower than one. The motor currents during ASC are lower than nominal motor currents due to low FWI. This operating mode does not cause thermal damage to the motor for this reason.

ASC currents of the three-phase motor can be calculated using the equation (5.3). R_s denotes phase winding resistance. Variables L_q and L_q represents motor inductances in dq coordinates. ω_e denotes electrical motor speed. Back-EMF constant is defined by λ_m. Variables i and u represent currents and voltages in dq coordinates.

$$\begin{aligned} u_d &= R_s i_d + L_d \frac{\mathrm{d}i_d}{\mathrm{d}t} - \omega_e L_q i_q \\ u_q &= R_s i_q + L_q \frac{\mathrm{d}i_q}{\mathrm{d}t} + \omega_e \lambda_m + \omega_e L_d i_d \end{aligned} \tag{5.3}$$

Voltages are equal to zero during ASC. dq currents are a function of speed. Steady state currents can be calculated using following equation (5.4). $i_{d_{\mathrm{ASC}}}$ and $i_{q_{\mathrm{ASC}}}$ denote motor currents during ASC operation.

$$\begin{aligned} i_{d_{\mathrm{ASC}}} &= -\frac{\omega_e^2 L_q \lambda_m}{\omega_e^2 L_d L_q + R_s^2} \\ i_{q_{\mathrm{ASC}}} &= -\frac{R_s \omega_e \lambda_m}{\omega_e^2 L_d L_q + R_s^2} \end{aligned} \tag{5.4}$$

The breaking torque T_{ASC} during ASC for the three-phase motor can be subse-

quently calculated using equation (5.5).

$$T_{\mathrm{ASC}} = \frac{3Pp}{2} R_s \lambda_m^2 \left(\frac{-\omega_e}{\omega_e^2 L_d L_q + R_s^2} + (L_d - L_q) \frac{-\omega_e^3 L_q}{(\omega_e^2 L_d L_q + R_s^2)^2} \right) \tag{5.5}$$

ASC currents of the dual three phase motor with low mutual inductances can be calculated using equations (4.19) and (4.20). These equations are suitable for motor with zero mutual inductance between d and q axis. This criterion is fulfilled according to Figure 5.8. Motor currents in case of ASC of both sub-systems are defined by (5.6). Variables $i_{d_{\mathrm{ASC\_ALL}}}$ and $i_{q_{\mathrm{ASC\_ALL}}}$ represent currents of individual sub-systems during full ASC operation. Here both sub-systems operate in ASC mode.

$$\begin{aligned} i_{d_{\mathrm{ASC\_ALL}}} &= -\frac{\omega_e^2 (L_q + M_{qq}) \lambda_m}{\omega_e^2 (L_d + M_{dd})(L_q + M_{qq}) + R_s^2} \\ i_{q_{\mathrm{ASC\_ALL}}} &= -\frac{R_s \omega_e \lambda_m}{\omega_e^2 (L_d + M_{dd})(L_q + M_{qq}) + R_s^2} \end{aligned} \tag{5.6}$$

However, only one sub-system can be switched into ASC mode using dual three-phase arrangement. In this case, ASC current of one sub-system can be calculated using the equation (5.7). The equation is for the case of the first short-circuited sub-system. Another sub-system operates with currents i_{d2} and i_{q2}.

$$\begin{aligned} i_{d1,\mathrm{ASC}} &= \frac{R_s \omega_e M_{qq} i_{q2} - \omega_e^2 L_q (M_{dd} i_{d2} + \lambda_m)}{\omega_e^2 L_d L_q + R_s^2} \\ i_{q1,\mathrm{ASC}} &= -\frac{R_s \omega_e (M_{dd} i_{d2} + \lambda_m) + \omega_e^2 L_d M_{qq} i_{q2}}{\omega_e^2 L_d L_q + R_s^2} \end{aligned} \tag{5.7}$$

The motor torque of the dual three-phase motor can be calculated using the simplified equation (4.25). The motor torque during operation with one ASC sub-system can be calculated using the equation (5.8).

$$\begin{aligned} T_e &= \tfrac{3}{2} Pp(\lambda_m (i_{q2} + i_{q1,\mathrm{ASC}}) + (i_{d2} i_{q2} + i_{d1,\mathrm{ASC}} i_{q1,\mathrm{ASC}})(L_d - L_q) + \\ &+ (i_{d2} i_{q1,\mathrm{ASC}} + i_{d1,\mathrm{ASC}} i_{q2})(M_{dd} - M_{qq})) \end{aligned} \tag{5.8}$$

ASC current of one sub-system is shown in Figure 5.10. Currents of second sub-system are equal to zero. The amplitude of phase currents is almost 160 A in this case. This value represents approximately 113 A rms. Table 5.1 defines maximum continuous current to 120 A. A motor can operate in this mode continuously.

The mutual influence between sub-systems slightly reduces the back-EMF voltage of the second sub-system. During all phase open simulation, the amplitude of back-EMF voltage is approximately 83 V. However, the back-EMF voltage of all

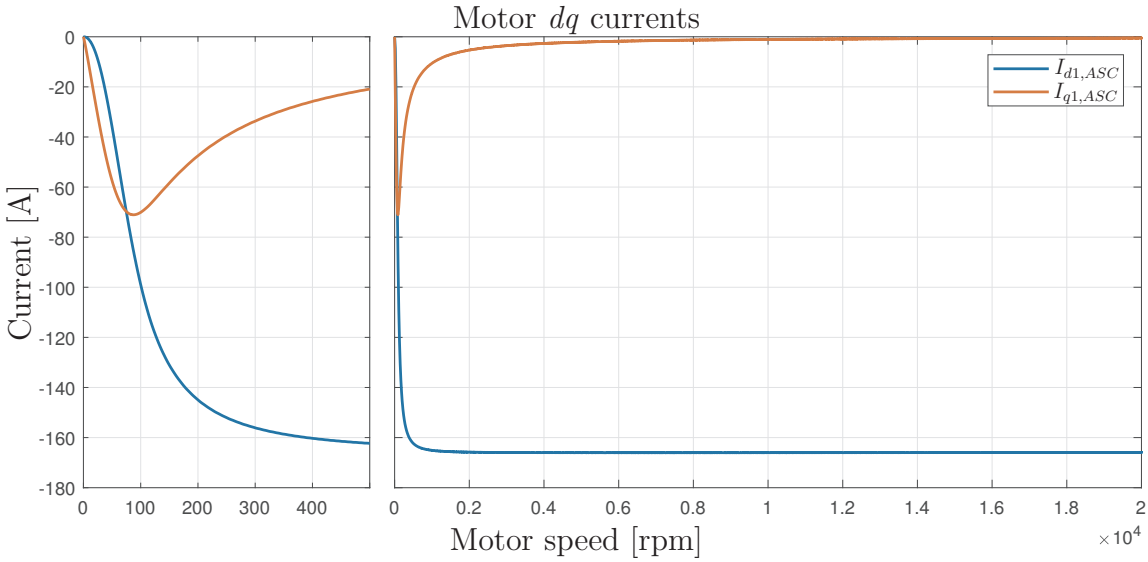

Fig. 5.10: dq currents of ASC sub-system with second sub-system disconnected.

phase open (APO) sub-system is reduced by ASC currents. This influence can be seen in figure 5.11. The voltage amplitude is reduced to approximately 65 V.

On the other hand, ASC currents are influenced by running a sub-system during the operation with one ASC sub-system. The influence can be determined by the equation (5.9) during a high speed operation.

$$\begin{aligned} \lim_{\omega_e \to \infty} i_{d1,\mathrm{ASC}} &= -\frac{M_{dd} i_{d2} + \lambda_m}{L_d} \\ \lim_{\omega_e \to \infty} i_{q1,\mathrm{ASC}} &= -\frac{M_{qq} i_{q2}}{L_q} \end{aligned} \tag{5.9}$$

Thus the mutual inductance between sub-systems can be used to reduce currents of ASC currents. However, the breaking torque generated by $i_{q1,\mathrm{ASC}}$ can be increased with the increasing generated torque. All these relationships need to be considered during the control algorithm design.

The whole motor can be switched into ASC too. In this case, ASC current of one sub-system is reduced due to the mutual inductances. The current of both sub-systems is shown in Figure 5.12. The value during the high speed operation can be calculated using the following equation (5.10)

$$\begin{aligned} \lim_{\omega_e \to \infty} i_{d_{ASC\_ALL}} &= -\frac{\lambda_m}{(L_d + M_{dd})} \\ \lim_{\omega_e \to \infty} i_{q_{ASC\_ALL}} &= 0 \end{aligned} \tag{5.10}$$

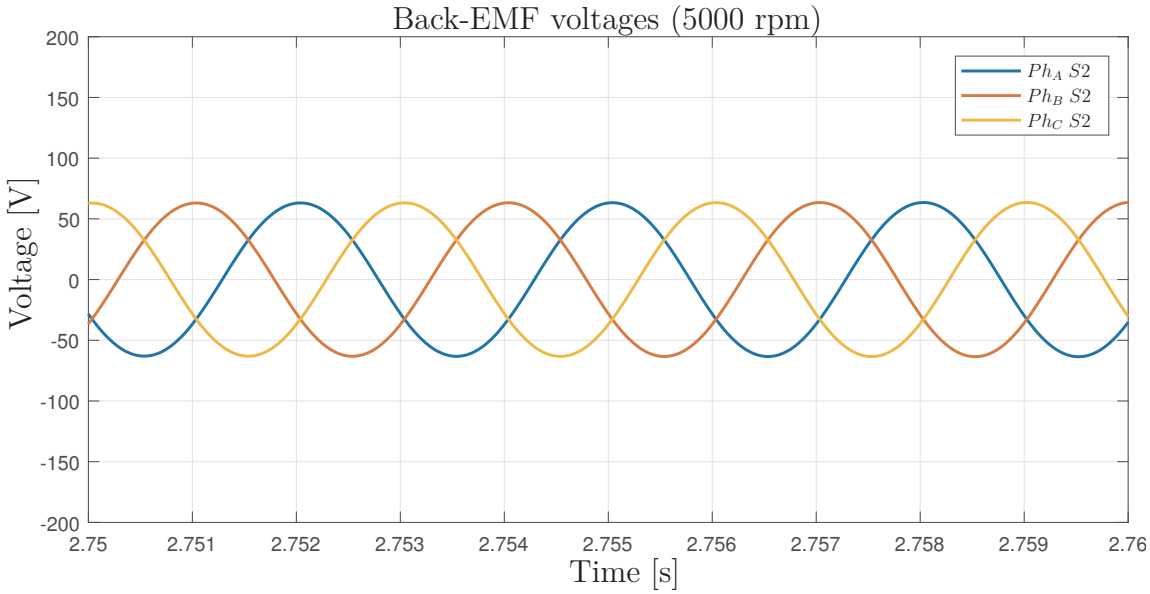

Fig. 5.11: Back-EMF phase voltages of dual three-phase motor with low mutual inductances between sub-systems while operating with one ASC sub-system.

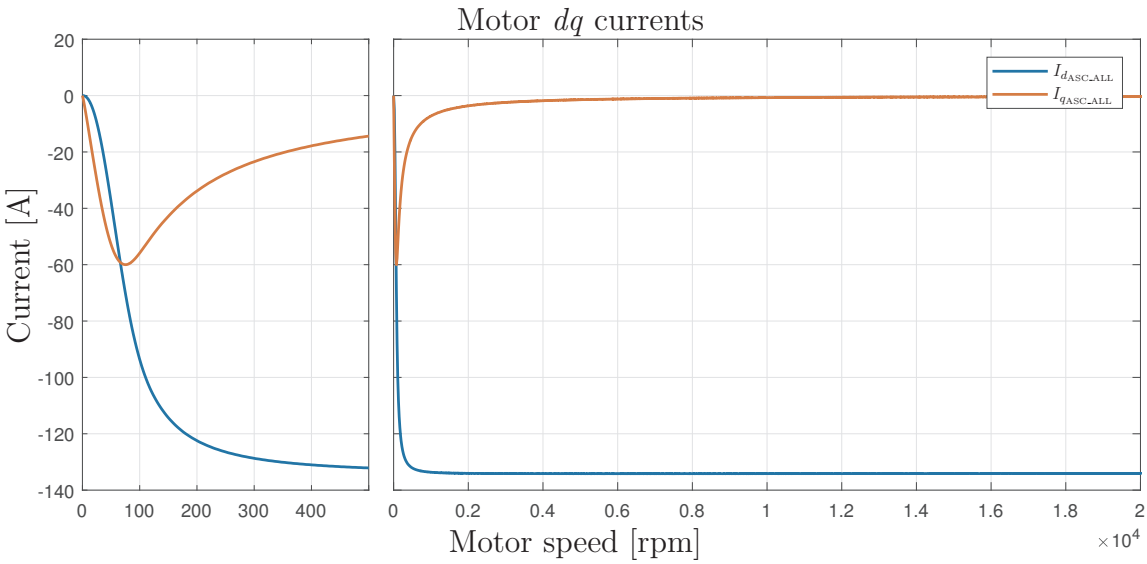

Fig. 5.12: Motor currents during both sub-systems ASC.

The motor current amplitude is reduced to approximately 130 A. This value represents roughly 90 A rms.

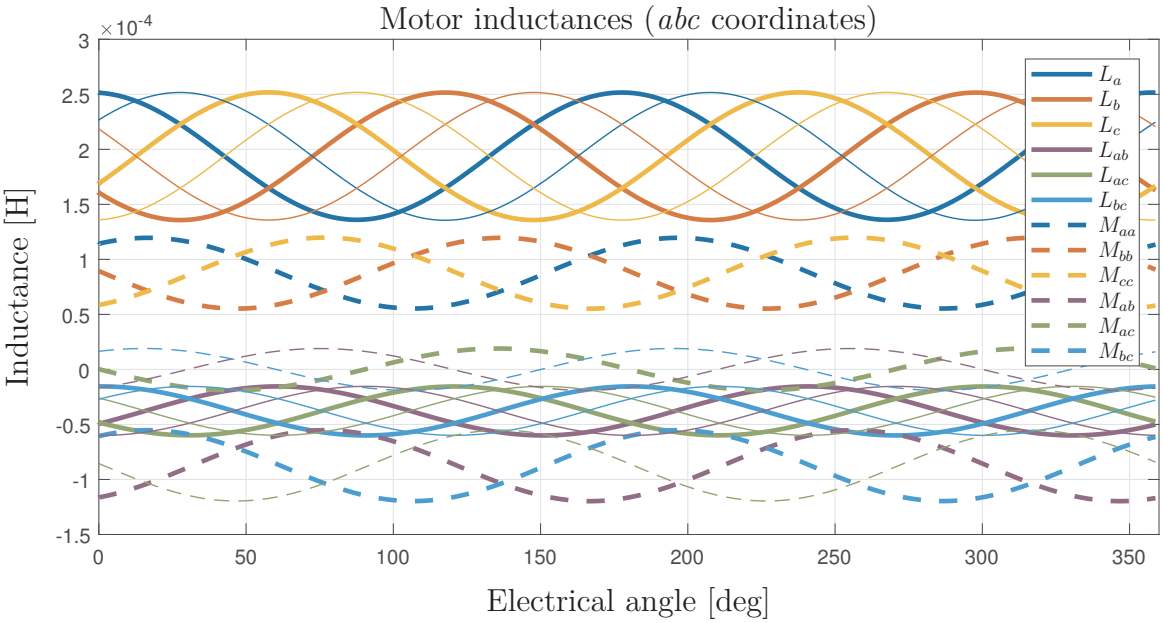

Fig. 5.13: Inductances of dual three-phase motor with high mutual inductances between sub-systems.

5.2 The motor with interlaced windings and high mutual inductances

High mutual inductances between motor parts is a typical feature of motors with distributed winding arrangement and interlaced sub-systems. This stator arrangement is shown in Figure 5.5. Coils of individual sub-systems overlaps each other using this stator arrangement and therefore there is a strong magnetic coupling between coils.

All motor inductances are shown in Figure 5.13. Inductances, as shown by the width of the curve, represent inductances related to the first sub-system. A narrow curve denotes inductances related to the second sub-system. Inductances reflect the phase shift between sub-systems caused by the mechanical arrangement.

Inductances can be transformed into dq coordinate system. The transformation principle is described in detail in chapter 4.2.3. Phase shift between sub-systems is taken into account by transformation. Inductances transformed into dq coordinates are shown in Figure 5.14. The motor is fully symmetrical and inductances are transformed into constants.

The mutual inductances represents approximately 65 % of self-inductances. Mutual inductances fluctuation is significantly higher compared to non-overlapping concentrated winding arrangement.

Back-EMF voltage of both sub-systems is shown in Figure 5.15. The electrical

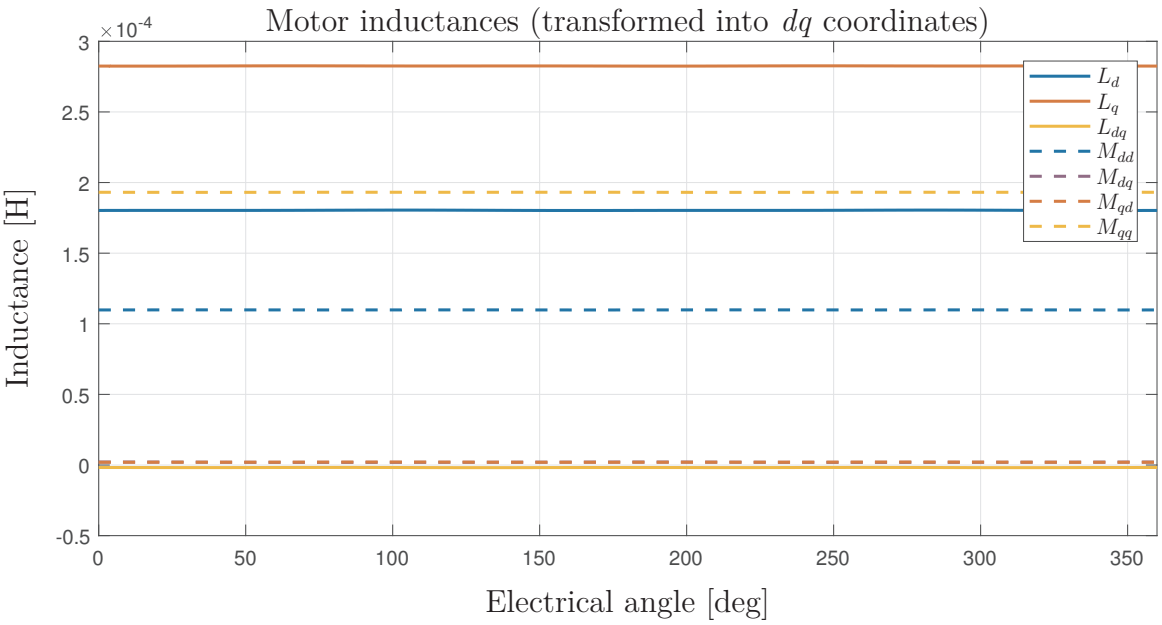

Fig. 5.14: Inductances of the dual three-phase motor with high mutual inductances between sub-systems transformed into *dq* coordinates.

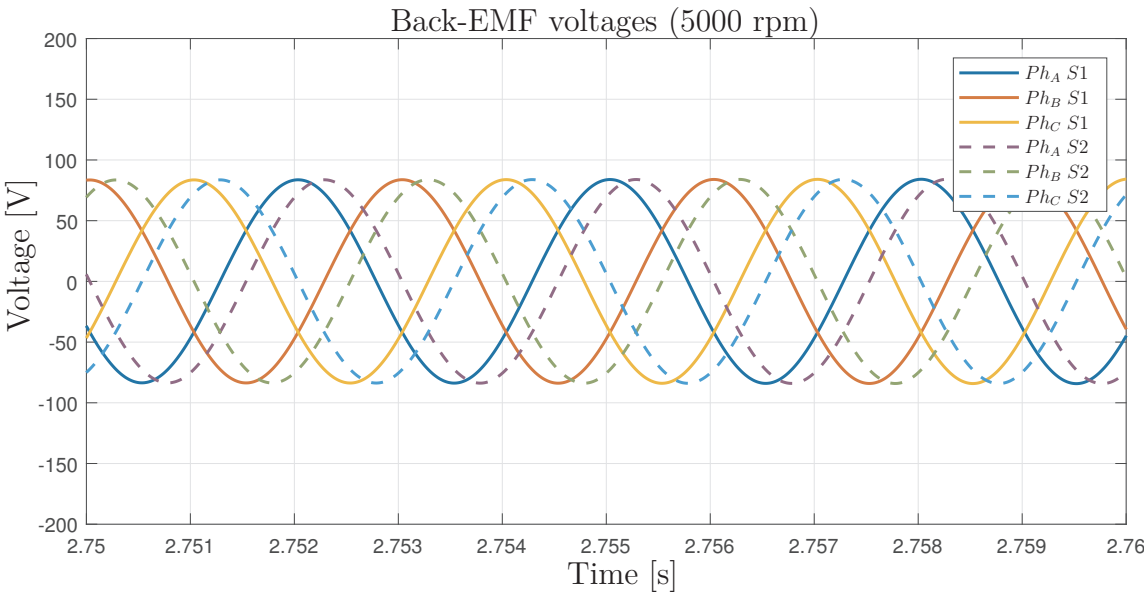

Fig. 5.15: Back-EMF phase voltages of dual three-phase motor with phase shift between sub-systems.

angle between sub-systems is 30 electrical degrees. Back-EMF constant is the same for each coil arrangement. Amplitude of back-EMF voltage is same as in previous arrangement for this reason.

5.2.1 Active short-circuit simulations

Simulation results of motor switched into ASC are almost the same in comparison with the previously analysed arrangement. This behaviour is caused by the same sum of mutual and self-inductances in all arrangements. The equation (5.7) can be used to calculate ASC currents also for this arrangement because the mutual inductance between d and q axis is almost zero (Figure 5.14). The motor currents are shown in Figure 5.16

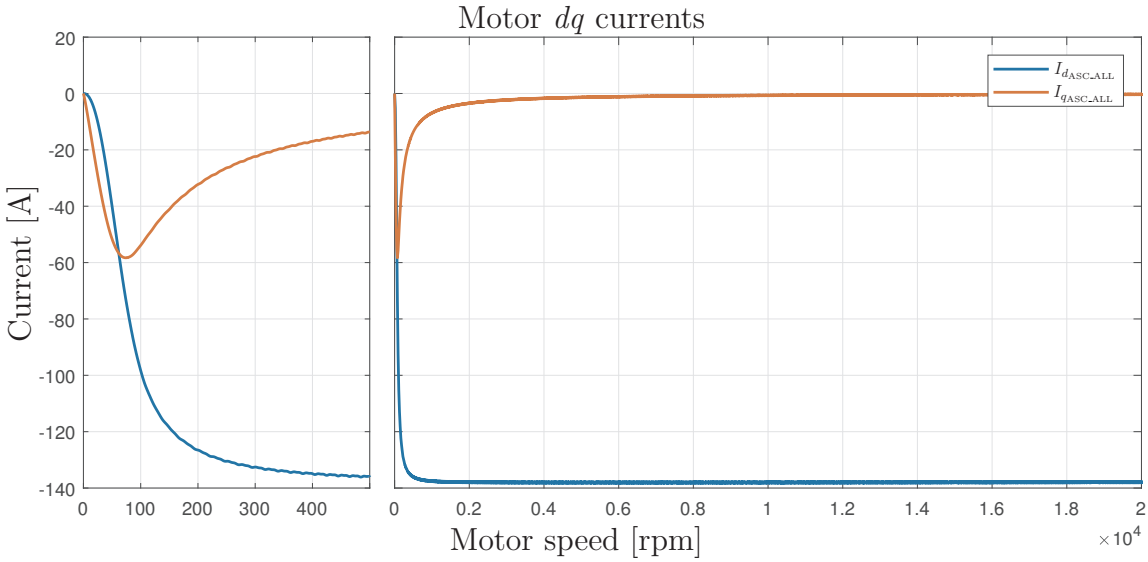

Fig. 5.16: Motor currents during both sub-systems ASC.

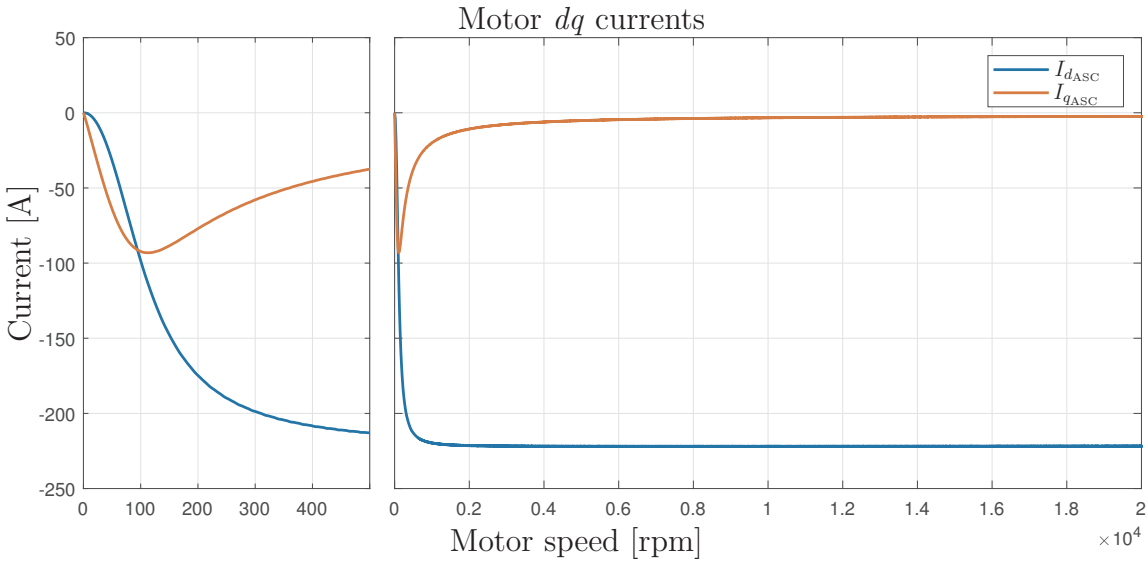

Fig. 5.17: dq currents of ASC sub-system with second sub-system disconnected.

The main difference between arrangements can be seen during ASC of one sub-system. Coils of one sub-system are evenly distributed over entire stator surface as shown in the Figure 5.5. Inductances of one sub-systems are lower comparing with other arrangements.

ASC current is roughly 220 A in dq coordinates as shown in Figure 5.17. This value represents approximately 155 A rms. The value is higher than the maximum continuous current. The motor cannot operate continuously in this mode.

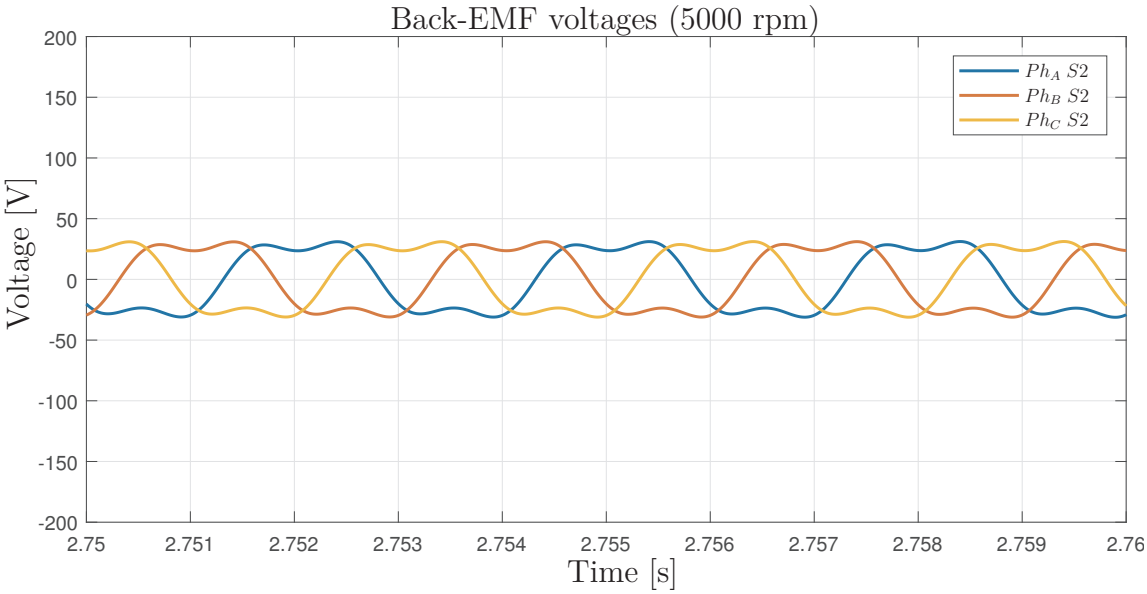

Fig. 5.18: Back-EMF phase voltages of dual three-phase motor with phase shift between sub-systems while operating with one ASC sub-system..

Another disadvantage of this arrangement comes from field weakening of the whole motor. Back-EMF voltage of the second sub-system is significantly reduced for this reason. Figure 5.18 shows back-EMF voltages of the second sub-system.

The voltage deformation is caused by the electrical shift between sub-systems, however, harmonic distortion of the voltage can be solved using the proper control algorithm. The principal problem is the motor power reduction. Theoretical maximum torque can be calculated using the equation (5.8).

ASC currents of one sub-system depend on currents of the second sub-system. The maximum motor torque for different phase currents of the second sub-system is shown in Figure 5.19. Field weakening angle was configured to reach the maximum torque using the actual current value. The values represent currents amplitude.

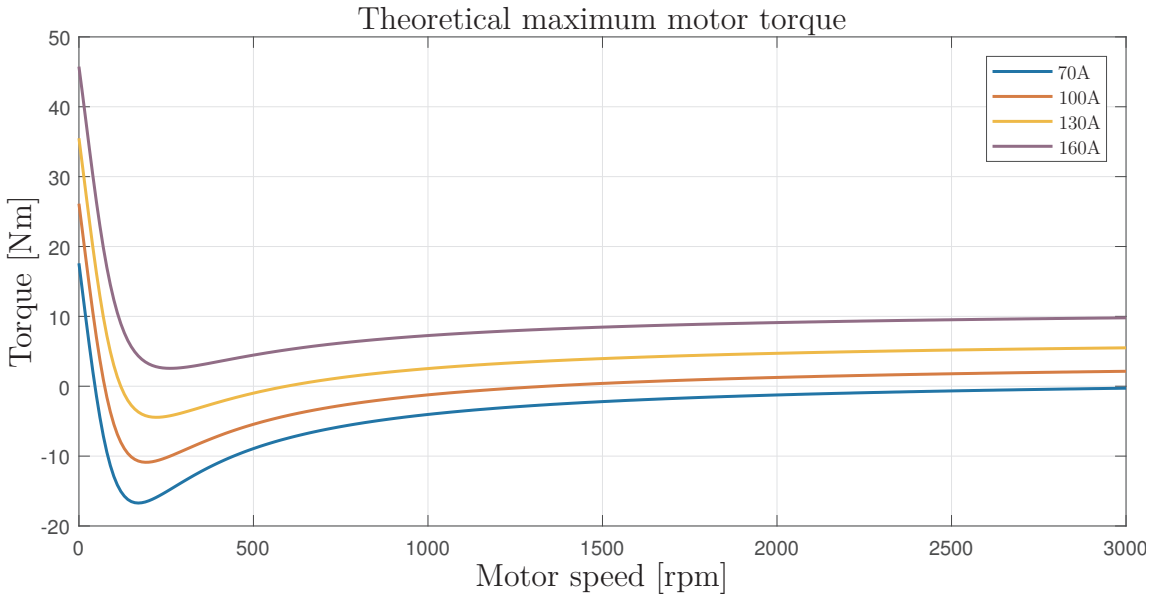

Fig. 5.19: Maximum achievable motor torque for different stator currents of active sub-system (second sub-system in ASC mode).

5.3 The motor with segregated windings

High mutual inductances between motor parts can be reduced using segregated structure. It uses a group of coils for each sub-system which are geometrically separated from other sub-systems. Segregated structure is shown in Figure 5.6. Mutual inductances between sub-systems are significantly reduced by the geometrical distance.

Geometrical separation is the main advantage of this structure. A short-circuit between the sub-systems can hardly occur. The fault is thus always situated in one sub-system. However, such a structure has also disadvantages. There is a strong magnetic coupling between phases within the sub-system. The mutual inductances between individual phases are not the same as already mentioned. This feature can be problematic during the motor operation.

The inductances of the dual three-phase motor with segregated windings are shown in Figure 5.20. Inductances of one sub-system are not symmetrical in contradistinction to previous structures. Transformation into dq coordinates can be performed, however, the inductances transformed into dq coordinates are not constant. The inductances transformed into dq coordinates are shown in Figure 5.21.

The entire motor structure is symmetrical and the combination of mutual inductances and self-inductances form fully symmetrical structure. This can be seen in

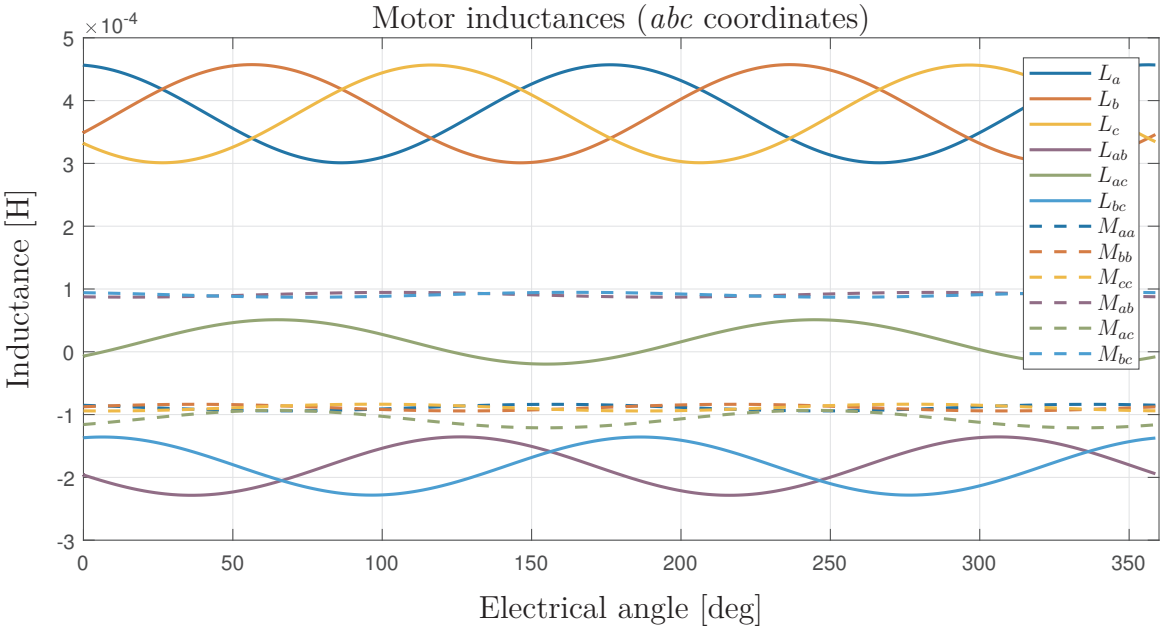

Fig. 5.20: The inductances of dual three-phase motor with segregated sub-systems.

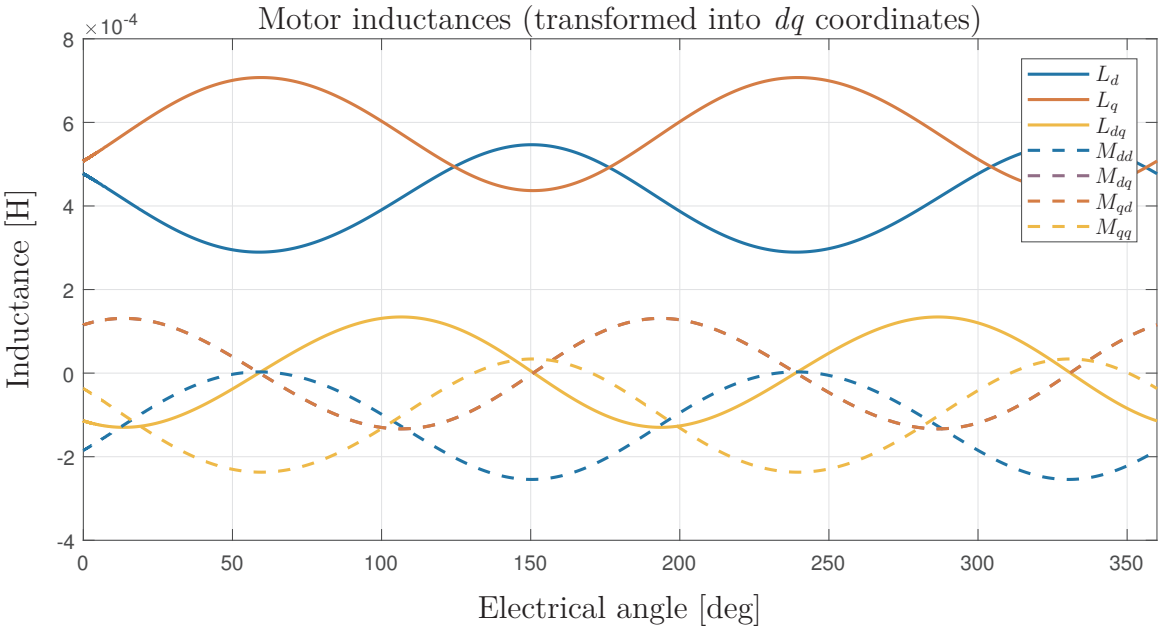

Fig. 5.21: The inductances of dual three-phase motor with segregated sub-systems transformed into dq coordinates.

the following statement (5.11)

$$\begin{aligned} M_{dq_{(\theta)}} + L_{dq_{(\theta)}} &\approx 0 \\ L_{d_{(\theta)}} + M_{dd_{(\theta)}} &= L_d^{eq} \\ L_{q_{(\theta)}} + M_{qq_{(\theta)}} &= L_q^{eq} \end{aligned} \tag{5.11}$$

The sum of self-inductances and the mutual inductances in dq coordinates is constant. The motor structure can be considered symmetrical if both sub-systems operate with the same phase currents. The motor behaviour during normal operations is symmetrical for this reason, but the behaviour of this structure during the fault is problematic. Another problematic behaviour can be caused by operating with the different phase currents. Back-EMF voltage of this structure is the same as back-EMF voltage of first analysed structure. This back-EMF voltage can be seen in the Figure 5.9

5.3.1 Active short-circuit simulations

The whole motor can be switched into ASC, as well as previous structures. The behaviour is almost the same. ASC currents can be seen in the Figure 5.22. If both sub-systems are switched into ASC, the equation (5.7) can be used to calculate the motor currents. An absence of torque ripples proves the motor symmetry.

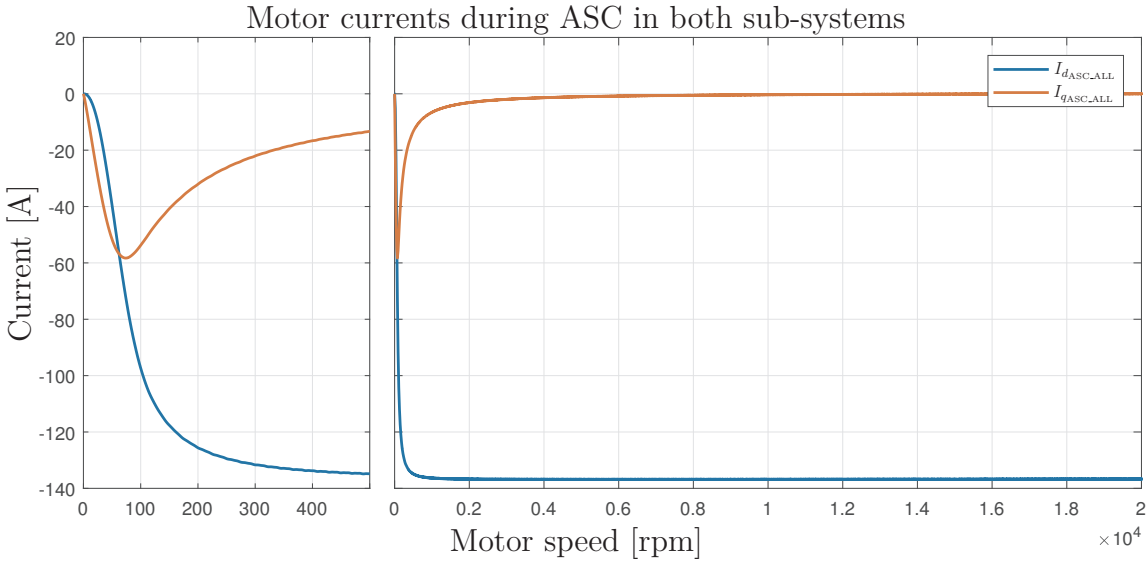

Fig. 5.22: dq currents of ASC in both sub-systems.

Problematic behaviour is caused by an asymmetry inductances within the sub-system. Fully balanced and harmonic back-EMF voltage do not generate fully harmonic currents during the ASC of one sub-system. Current amplitude is the same for boundary phases, however, current amplitude of the middle phase is lower. This behaviour can be seen in the Figure 5.23. The harmonic distortion of phase currents is also visible.

Currents of ASC sub-system can be transformed into dq coordinates. However dq currents contain ripples. The current ripples subsequently generate undesirable torque ripples. The motor dq currents can be seen in Figure 5.24.

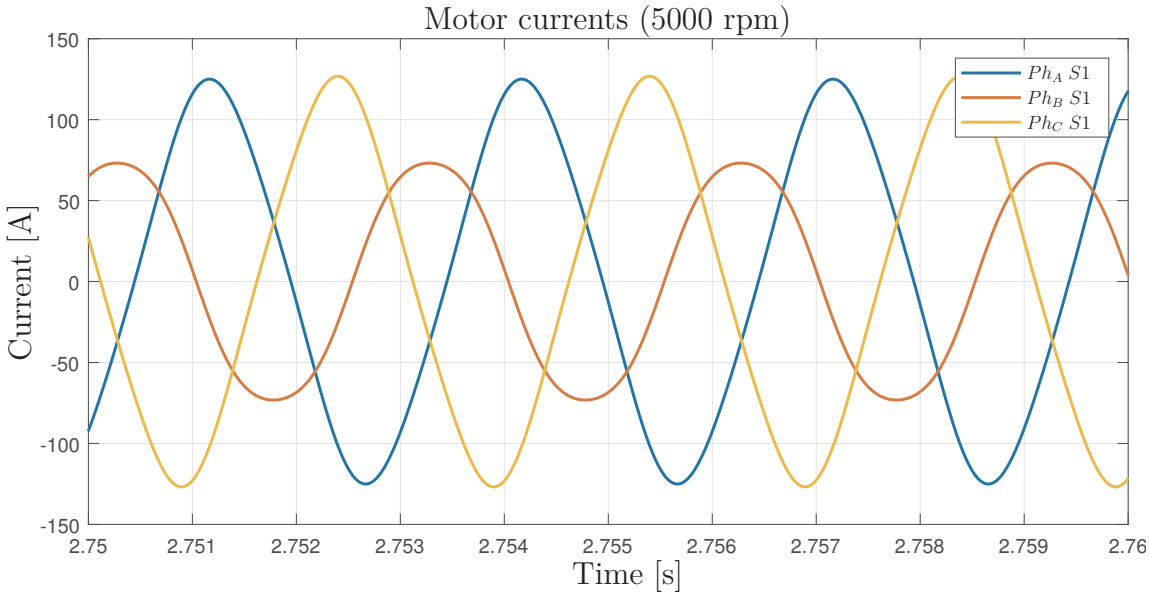

Fig. 5.23: Motor currents during ASC operation in one sub-system.

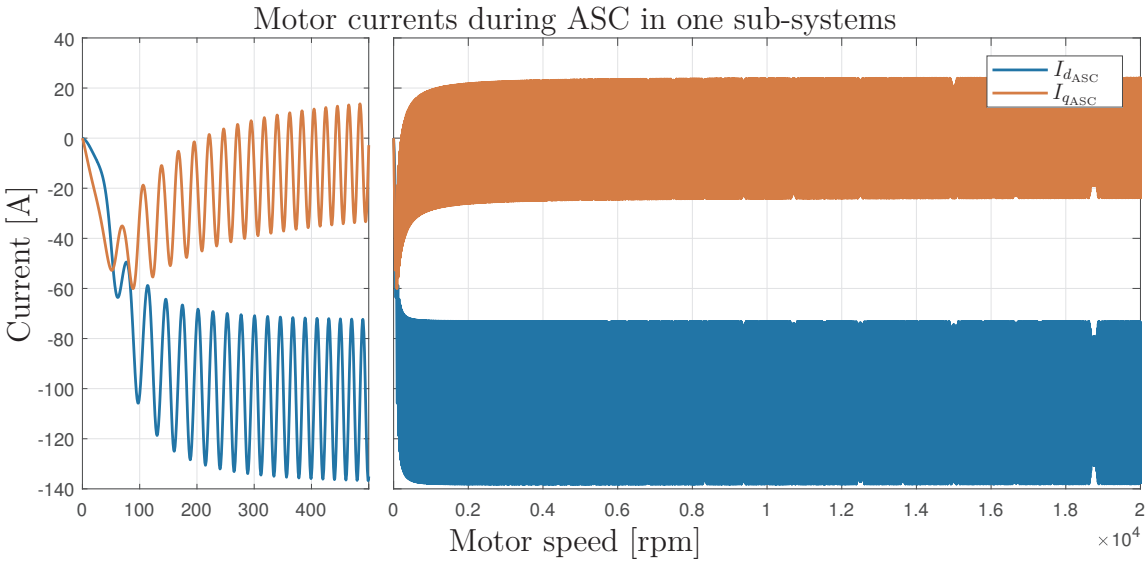

Fig. 5.24: *dq* currents of ASC sub-system.

Currents amplitude is lower than 140 A. This value represents approximately 100 A rms. The value is lower in comparison with the maximum continuous motor current. The motor can operate continuously in this operation mode. Back-EMF of the second sub-system is influenced by ASC currents. The voltage amplitude is not reduced. However, the voltage waveform is distorted. Figure 5.25 shows back-EMF waveform of the second sub-system during an operation at 5000 rpm. The voltage deformation and torque ripples must be considered during the control algorithm design. The motor can operate using only one sub-system, but the control algorithm

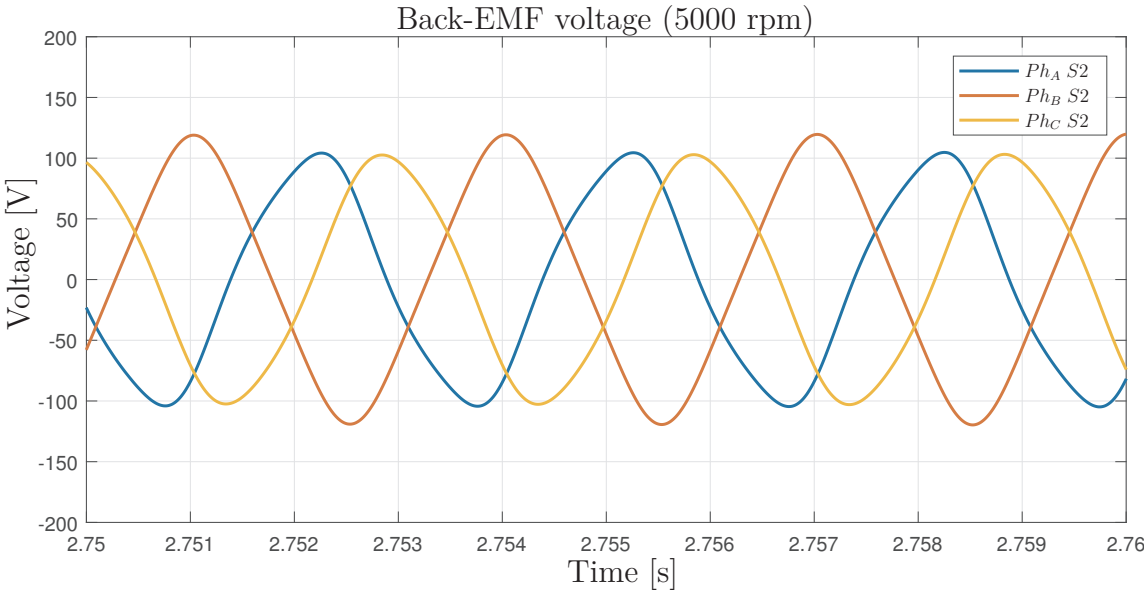

Fig. 5.25: Back-EMF phase voltage of dual three-phase motor with segregated sub-systems and one ASC sub-system.

needs to be adapted to the motor asymmetry. Mutual inductances between sub-systems are also asymmetric. The control algorithm for this type of motor is dealt with in chapter 7.

6 FAULT ANALYSIS

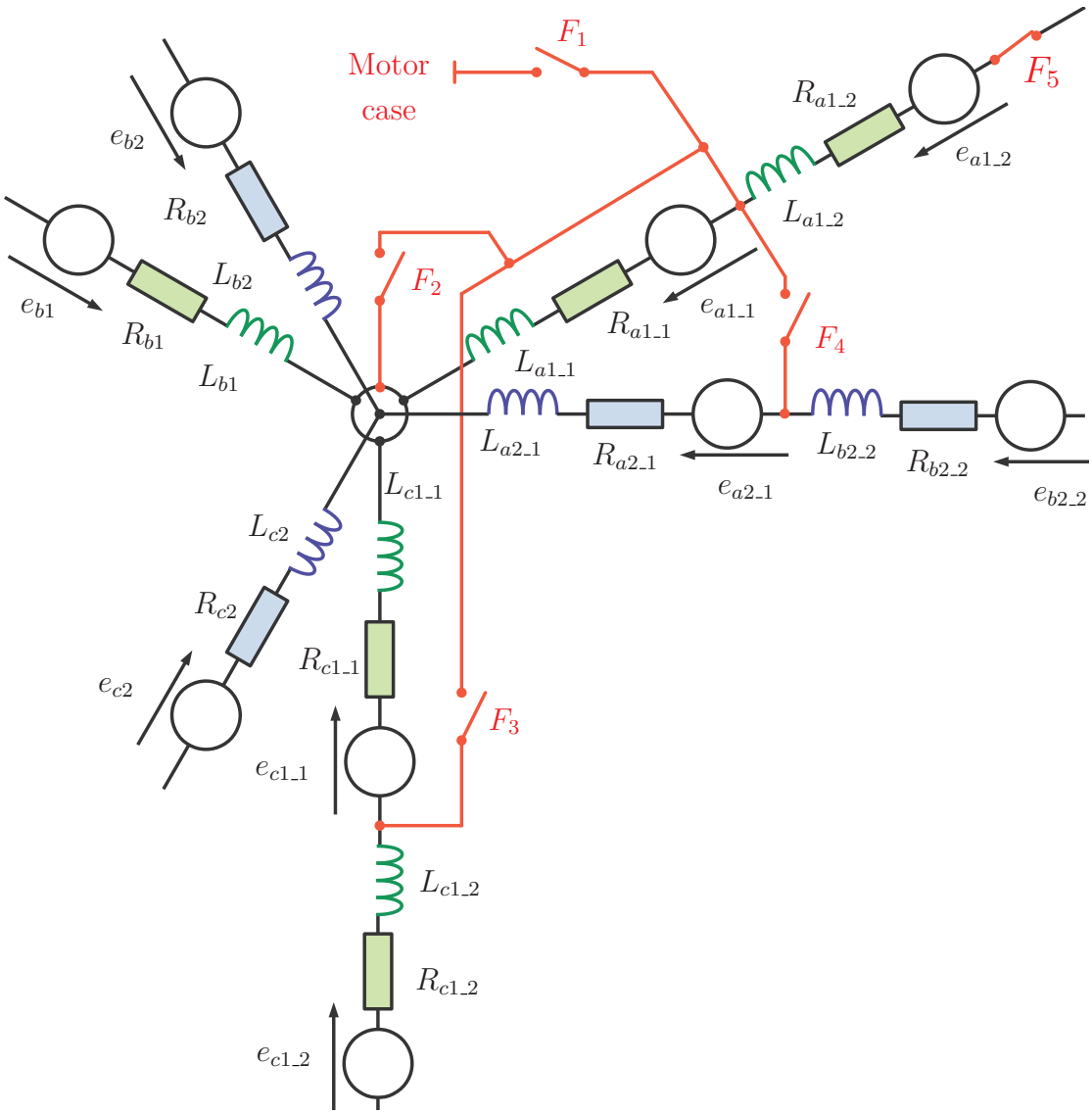

Fig. 6.1: Simulated motor faults.

This chapter deals with electrical faults of dual three-phase PMS motors. Analysed faults are shown in Figure 6.1. Stator winding short-circuits represent the most typical electrical faults of the motors. The short-circuit can appear in one subsystem or even between sub-systems. Another possible fault is phase disconnection due to mechanical damage of the wire.

The most typical short-circuit is between the motor phase and the motor case [33]. This fault can be simulated by activating fault switch F_1. The motor case potential can vary depending on the application. Optional motor case's potential

can be used during simulations. In some cases the motor case can be galvanically isolated from the inverter DC-link.

Inter-turn short-circuit is another problematic fault of stator winding. Rapid local increase in temperature is caused by this fault. Damage of other windings can be caused by the increased temperature subsequently. This fault can be simulated using fault switch F_2. The phase winding L_a can be divided into the coils L_{a1_1} and L_{a1_2} with customizable ratio. Inter-turn short-circuit of one coil turn or even more turns can be simulated.

The short-circuit between different phases can occur in some stator configurations. Two variants can appear and can be modeled. The first variant represents short-circuits within one sub-system. This type of fault can be simulated using the fault switch F_3. The second variant is closely related to a multiple three-phase arrangement. Individual three-phase sub-systems are electrically separated during normal operation. However, the short-circuit between different sub-system phases is also possible especially using the multiple three-phase motor with distributed winding and interlaced sub-systems. This fault can be simulated using the fault switch F_4.

The last fault is a disconnected wire. This fault can be located inside of the motor, or disconnected wire between the motor and inverter. Fault consequences are the same in both cases. The fault position is not relevant during this fault because the current can not flow through disconnected winding. This fault can be simulated using the fault switch F_5.

6.0.1 Short-circuit to motor case

This fault represents the most typical fault of the stator winding [34]. The motor behaviour during this fault depends on the motor case potential. The standard industry three-phase inverters use three-phase power of the electrical grid. The inverter uses the rectifier bridge to form a DC-link. The DC-link middle voltage potential is the same as the potential of ground and the electrical grid neutral point. In this case, the motor case is typically connected to the ground.

The motor case can be connected to the negative (or even positive) pole of DC-link in other applications. This situation is typical for battery powered systems. For example battery tools.

Another possibility is to use the galvanic separation between the motor case and DC-link. Motor currents do not change during this fault. The insulation monitoring device can be used to detect the fault in this case. This solution is suitable especially for safety-critical systems.

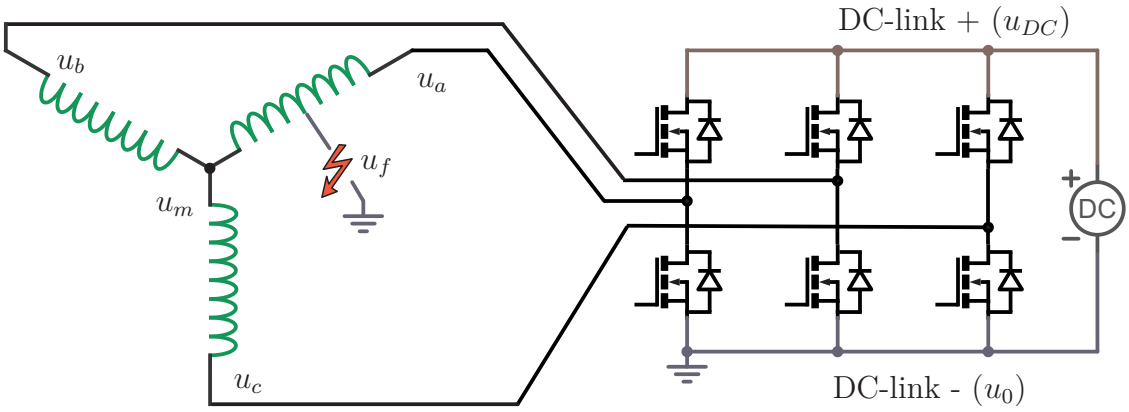

Fig. 6.2: Damaged winding connected to grounded motor case.

The motor case connected to DC-link potential

The voltage between the fault point and the motor case depends on several aspects. Motor structure analysis in chapter 5 shows the behaviour of different motor structures. All analysed structures are symmetric during normal operation. Motor middle point voltage u_m can be calculated using an arithmetic mean of phase voltages (6.1).

Phase voltages u_a, u_b and u_c represents motor terminal voltages. Negative DC-link voltage represents voltage reference u_0. The connection is shown in Figure 6.2.

$$u_m = \frac{u_a + u_b + u_c}{3} \tag{6.1}$$

$$u_f = (1 - \sigma)u_a + \sigma u_m \tag{6.2}$$

The fault voltage u_f represents the voltage between the motor case and the damaged wire. Model parameter σ defines the position of the fault. Value $\sigma = 0$ represents the fault situated in the motor terminal. Value $\sigma = 1$ represents the fault in motor middle point.

The control algorithm can add offsets to the phase voltages to suppress the fault currents. However, the fault voltage is always positive in this case. The current flows from the inventer into the motor case during this fault. This current is represented by variable i_f. The fault voltage can be reduced by configuring all phase voltages to zero. Zero voltage represents ASC of the sub-system.

This fault was simulated using dual three-phase motor with interlaced subsystems and low mutual inductances. The parameter σ was set to 1 (motor middle junction connected to the motor case). The DC-link voltage was configured to 800 V.

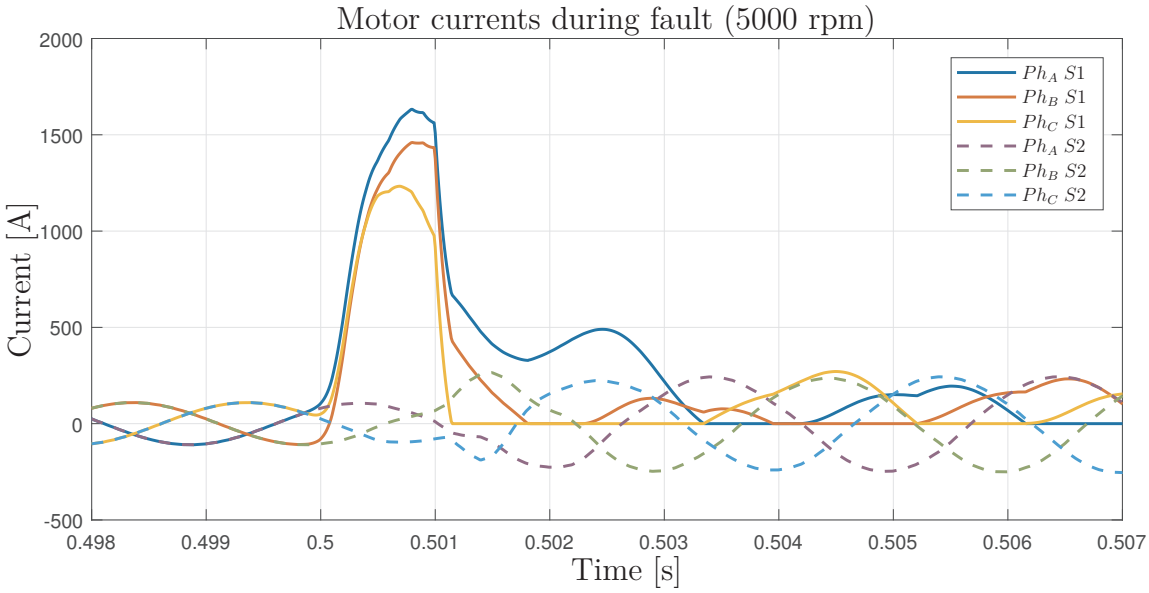

Fig. 6.3: Motor currents during the short-circuit to DC-link negative pole fault.

The current increase is rapid during the fault. This type of fault can be detected using the overcurrent flag. Hardware detection using transistor desaturation fault can be also used. The sum of currents must be monitored as well to detect this fault.

Figure 6.3 shows motor currents. The fault switch F_1 was activated in time of 0.5 s. Damaged sub-system is switched into APO mode one millisecond after the fault. Motor currents after the sub-system disconnection are not zero due to motor back-EMF voltage. Motor currents depend on fault position. The fault current i_f is approximately 230 A (Figure 6.4).

Damaged sub-system can be also switched into ASC to reduce the fault voltage as follows from equation (6.1) as already mentioned. ASC must be realised using bottom transistors to configure a zero voltage on motor terminals. The fault current is significantly reduced using this method. Fault current i_f oscillates around zero with the amplitude of 10 A (Figure 6.5).

Motor case connected to DC-link middle potential

This fault is similar to previously mentioned faults. However, the fault voltage u_f can be either positive or negative in this case. The fault voltage can be calculated using the equation (6.3).

$$u_f = (1 - \sigma)u_a + \sigma u_m - \frac{u_{DC}}{2} \tag{6.3}$$

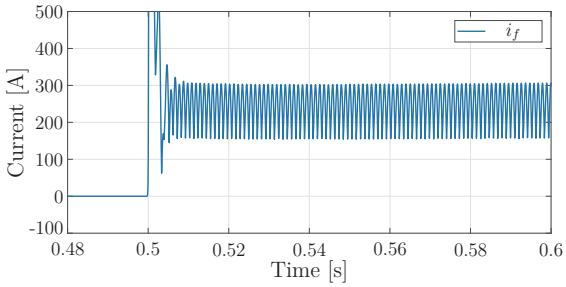

Fig. 6.4: Damaged sub-system switched into APO mode.

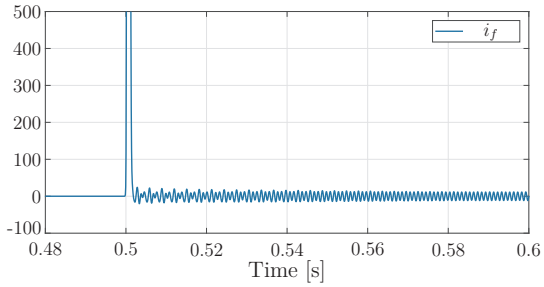

Fig. 6.5: Damaged sub-system switched into ASC mode.

In normal operation, the middle point voltage u_m depends on used pulse width modulation (PWM) technique to generate phase voltages. Several different methods are typically used. The sinusoidal pulse-width modulation (SPWM) is the first method. SPWM is the simplest modulation, however, this modulation is not able to effectively use all the available DC-link voltage. The motor middle point voltage is equal to the center of the DC-link voltages in this case [35].

The third-harmonic injection pulse-width modulation (THIPWM) represents the second possible method to generate phase voltages. This technique can improve the inverter performance due to the motor middle point voltage changes.

The third method is the space vector pulse-width modulation (SVPWM) [36]. This method adds triangular voltage.

The phase voltage waveforms and the middle point voltage for all three modulation techniques are shown in Figure 6.6.

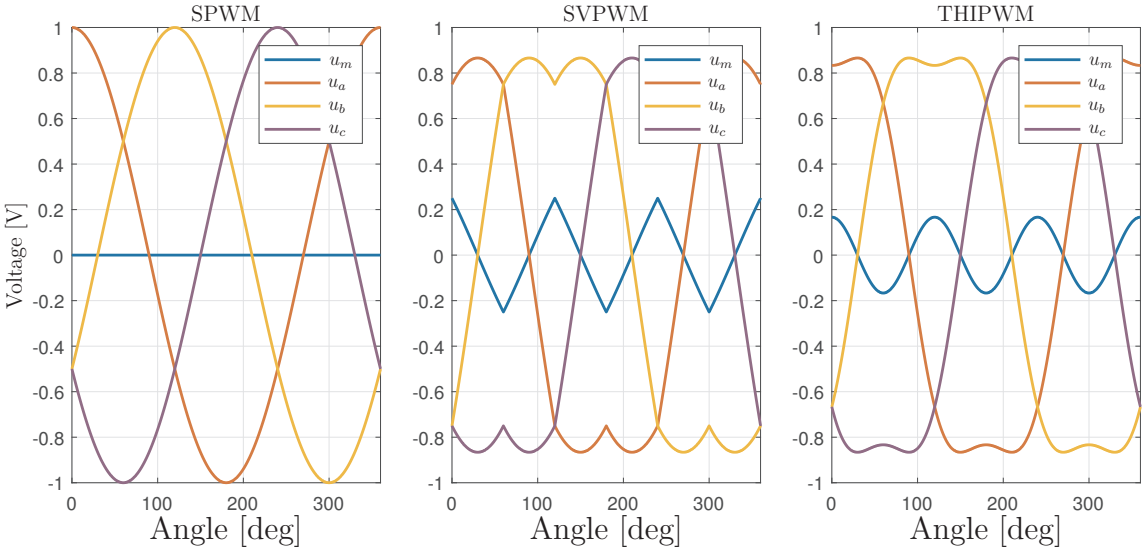

Fig. 6.6: Differences in PWM modulation techniques.

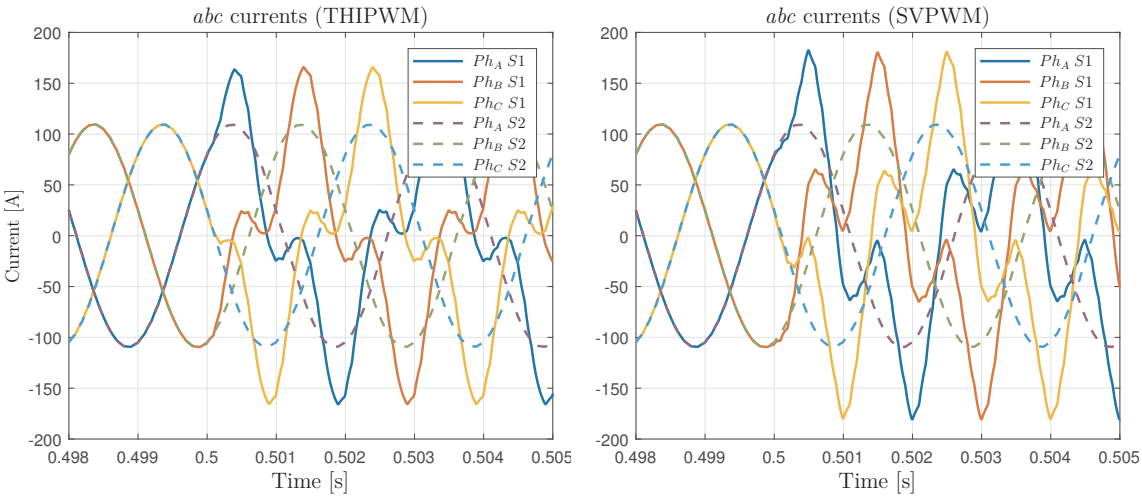

Fig. 6.7: Motor currents during the middle point short-circuit to motor case.

The fault current depends on the selected voltage modulation technique. The figure 6.7 shows motor phase currents for different voltage modulations during the middle point short-circuit to the motor case. Harmonic distortion using THIPWM is lower in comparison to a harmonic distortion using SVPWM. Only these two methods are compared because the fault current using SPWM is equal to zero. The damaged sub-system can be switched into APO mode or fed up with 50 % duty cycles to reduce the fault current.

6.0.2 The interturn short-circuit

This type of fault may occur in every type of electric machine. This fault can be described as short-circuit between two turns of one motor winding. Created current-turn is located inside of the motor and the fault current flowing through it cannot be measured. Changes in back-EMF voltage can be used to detect this type of fault. Changes in magnetic flux generated by the rotor rotation induce high currents into current-turn. The fault current amplitude depends on a number of short-circuited turns and the fault point resistance. Fault current amplitude for motor with zero currents depends on the following equation (6.4). This equation does not reflect the influence of mutual inductances between sub-systems. Variable n_{it} denotes a number of coil turns which are short-circuited. Variable n_o represents overall number of turns in one motor phase. The inductance of the short-circuited part is represented by L_{it}. R_{it} denotes the resistance of the whole short-circuited part.

$$I_f = \frac{\omega_e \lambda_m n_{it}/n_o}{\sqrt{R_{it}^2 + L_{it}^2 \omega_e^2}} \tag{6.4}$$

Taking into account the mutual inductance to the sub-system currents, following equation (6.5) can be derived. Variable M_{it} denotes the mutual inductance between the shorted part and the rest of the damaged winding.

$$I_f = \frac{\sqrt{\omega_e^2(\lambda_m n_{it}/n_o + M_{it} i_d)^2 + M_{it}^2 i_q^2}}{\sqrt{R_{it}^2 + L_{it}^2 \omega_e^2}} \tag{6.5}$$

More complex form of the equation (6.5) can be derived considering mutual inductances between short-circuited winding part and the other motor sub-systems. However, because of its small value, this mutual inductance can be neglected.

High fault current amplitude is caused especially by the low resistance and inductance of short-circuited part. This current causes a local increase in temperature and can cause other winding faults due to over-heating. Therefore, a rapid detection of this fault is essential. Changes in magnetic flux need to be reduced in order to decrease the fault current. The reduction can be reached by switching sub-system into ASC or by active field weakening. The mutual inductance between damaged part of coil and the rest of winding is typically higher in comparison to the self inductance of a damaged coil part. The mutual inductance in combination with the field weakening current reduces the fault current.

Figure 6.8 (left side) presents measured motor current of both sub-systems transformed into dq coordinates. The right side of the figure presents unmeasurable interturn current.

Switching into ASC is shown in Figure 6.9. Left side of the figure shows motor dq currents and the right side shows reduction of fault currents. The fault current value is reduced and the motor can continuously operate with reduced power.

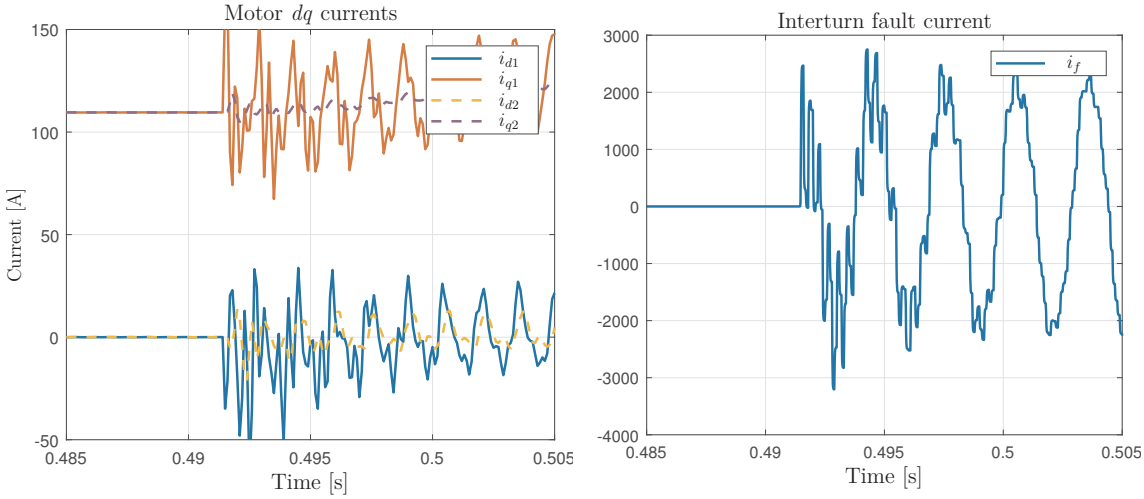

Fig. 6.8: Motor currents during interturn short-circuit scenario.

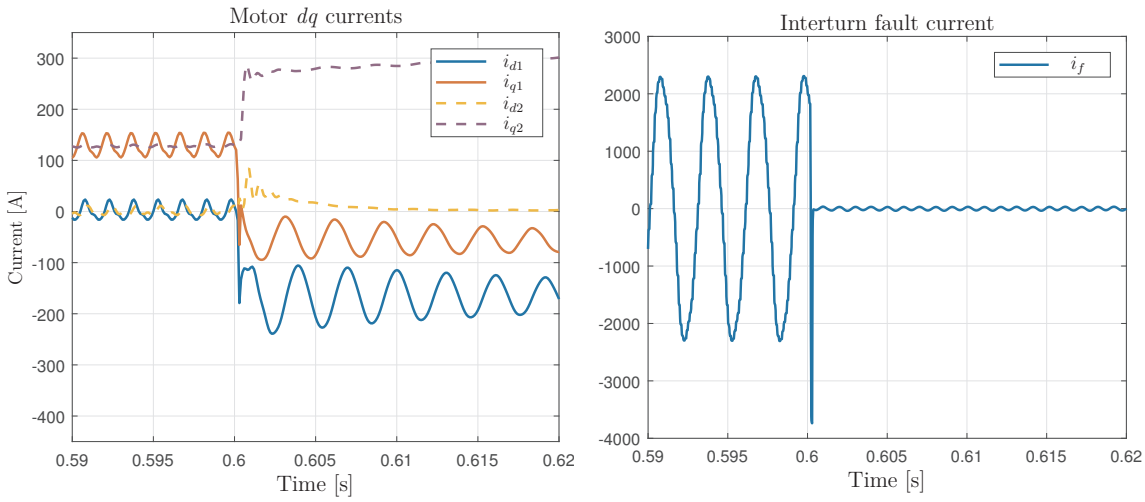

Fig. 6.9: Motor currents during interturn short-circuit (with active compensation).

6.0.3 Short-circuit between phases within one sub-system

This fault can be divided into two variants: The first variant is an interconnection of two phases of one sub-system inside of the motor. The second variant is the shunt located between motor and inverter. The first fault can be detected using current distortion; The second variant must be detected using inverter hardware. If two inverter phases are connected together, the transistor desaturation fault occurs. (One phase connected to DC Bus+ and the second phase connected to DC Bus-). In both cases, the sub-system can be easily switched into ASC.

The first variant of this fault is a connection of two windings inside the motor. The behaviour depends on the position of a winding connection point. This fault creates a closed circuit which cannot be directly controlled. The fault current of this closed circuit is also unmeasurable. The fault current can generate torque ripples or a rapid local increase of temperature.

The behaviour can be similar to the interturn short-circuit fault. This behaviour is typical if the connection of two windings is close to the sub-system middle junction. Local increase in temperature is problematic in this case. On the other hand, a short-circuit in a bigger distance from the middle junction can cause significant torque oscillations. Instability of the control algorithm can appear due to the reduced phase to phase inductance and resistance between damaged phases. An active short-circuit mode can be used to reduce fault impact in this case.

The second variant causes high transistor currents and damage to the inverter is possible. This fault needs to be detected by the hardware, because a software detection is too slow. Desaturation error leads to switching inverter into APO mode typically. Inverter can be subsequently switched into ASC after inverter fault reset. During operation in ASC mode, the voltage potential of both phases is the same.

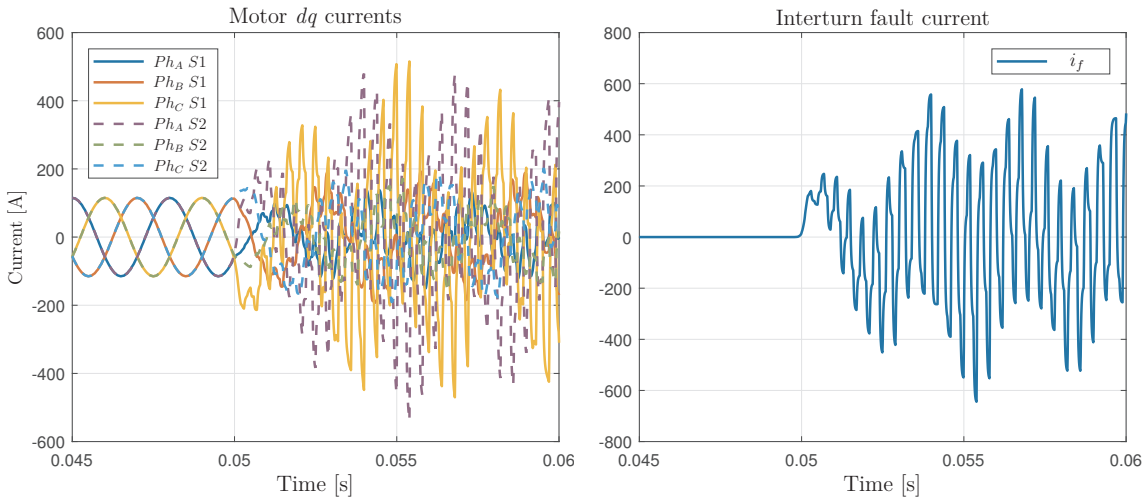

Fig. 6.10: Motor currents during short-circuit between sub-systems.

6.0.4 Short-circuit between sub-systems

Sub-system to sub-system short-circuit can occur in multiple k-phase motors. Such multi-phase motors consist of several electrically separated sub-systems. The closed circuit is not created inside of the motor in comparison to the faults described previously. On the other hand, a current can flow from one sub-system to another during this fault. This fault affects both motor sub-systems.

Electrical connection between sub-systems can be located between the inverter and motor or inside of the motor similar to previously described fault. The fault located between the power inverter and motor must be diagnosed using and inverter hardware. Simple switching of one sub-system into APO mode can solve this fault during low speed operation. However, back-EMF voltages can generate currents within the switched off sub-system. Both sub-systems can be switched into active short-circuit to decrease fault currents during high speed operation. However, motor cannot generate torque during ASC of the whole motor. The last option is to use compensation to reduce the current flow between sub-systems.

During the simulation, the first sub-system winding B middle point was connected to another sub-system winding A middle point in order to create example fault. The resistance of connection was configured to 0.5 Ω to reduce fault current amplitude during simulation. Because a high fault current amplitude causes overcurrent fault in both sub-systems. The fault was simulated at time t = 0.05 s. Motor currents of both sub-systems (left) and the fault current which flows from one sub-system into another (right) are shown in Figure 6.10.

The fault compensation control method can be used to reduce the fault current if the position of the fault is known. Both motor sub-systems can be controlled as one complex six-phase system, instead of two electrically isolated three-phase

systems. Voltages of individual phases are configured to reduce current flow from one sub-system to another by keeping the connection point at an equal potential. This control method is relatively simple, however, the exact position of the electrical connection between sub-systems is required for proper operation. Figure 6.11 shows the principle of the compensation algorithm.

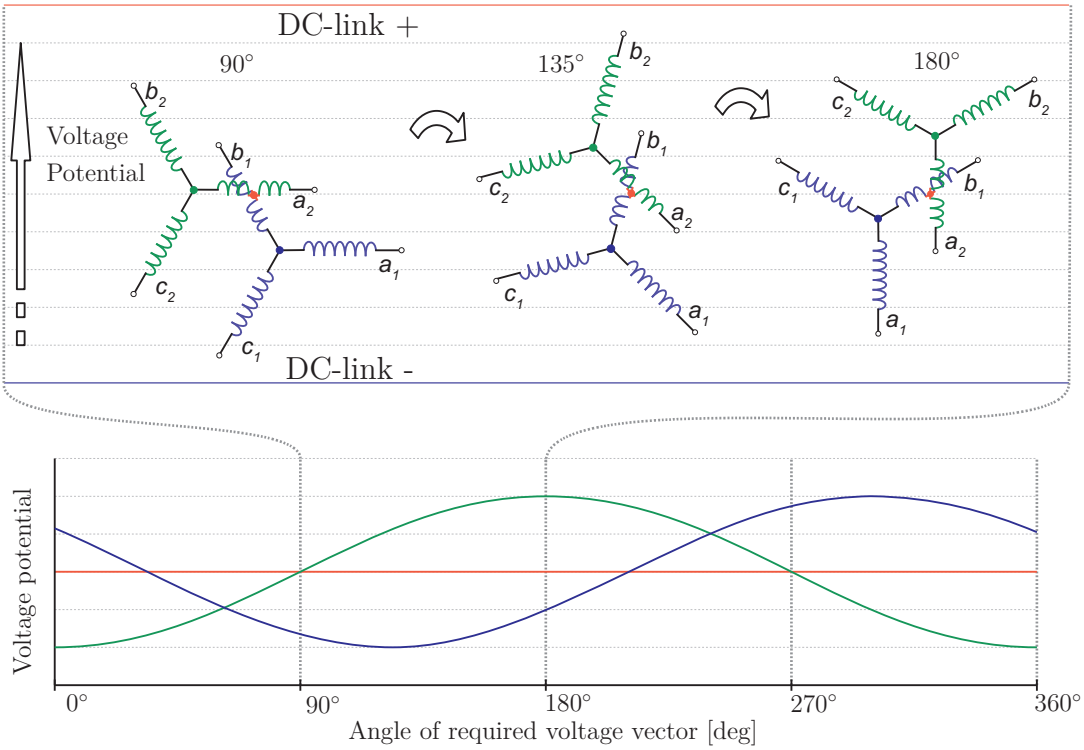

Fig. 6.11: Principe of compensating algorithm to keep the same voltage potential of short-circuit point between sub-systems.

The winding endpoint position represents required voltage potential. Both sub-systems are now electrically connected and voltage vectors of individual sub-systems cannot rotate independently. SPWM with voltage offset is used to reduce fault current instead of SVPWM. Red point represent the connection between sub-systems. Position of green and blue points represent changes in middle point potential of individual sub-systems. Sub-system middle points (blue and green line) and fault point (red line) voltage potentials as a function of voltage vector angle are shown in Figure 6.11 (bottom). Voltage values needs to be adapted according to the actual rotor position and required voltage amplitude.

Motor currents and motor voltages with an active compensation are shown in Figure 6.12. Phase to phase voltages of individual sub-systems are not changed. Field weakening and other control algorithm features can be used. DC-link usage

during the compensation is 49 % higher in this case. However, this value depends on a contact point between sub-systems.

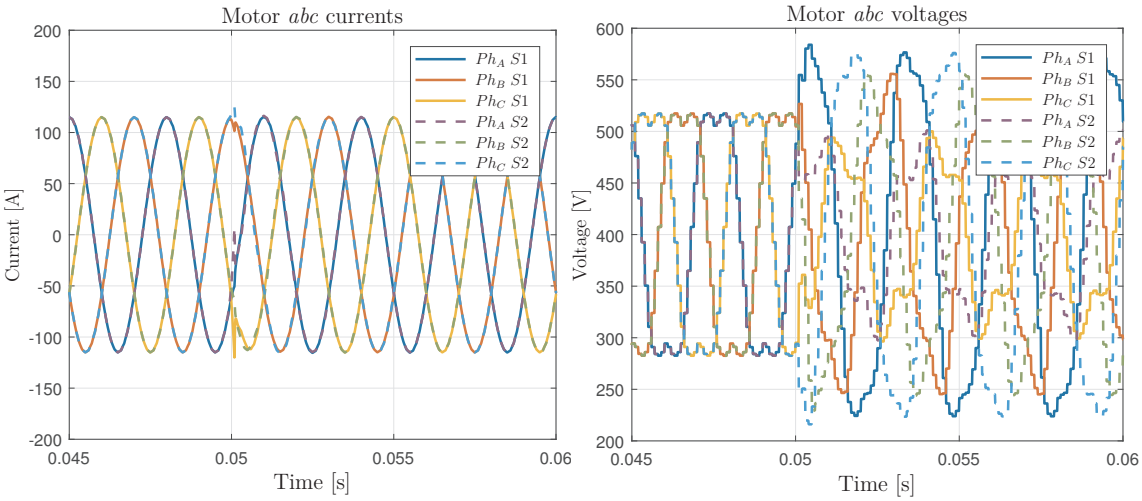

Fig. 6.12: Motor currents and voltages during short-circuit between sub-systems with active compensation.

6.0.5 Disconnected winding

This type of fault can be caused by the mechanical damage of a power cable between motor and inverter. The phase can be also disconnected inside of the motor due to the mechanical damage. The current cannot flow through damaged phase during the fault. The damaged sub-system cannot be switched into ASC because one phase is disconnected and currents during ASC are not balanced. Unbalanced currents generate torque oscillations. This behaviour can be problematic especially during high speed operation. Motor can operate up to the nominal speed with damaged sub-system in APO mode.

The field weakening of active sub-system can be used to partially decrease back-EMF voltage of damaged sub-system. Mutual interaction between sub-systems is described in detail in chapter 5. Torque ripples can be suppressed by active sub-system using mutual inductances.

Motor back-EMF constant used in simulations allows to switch damaged sub-system into APO up to maximum motor speed. For this reason, the DC-link voltage used in simulation was decreased to 100 V. The motor was operated at 5000 rpm. The phase to phase back-EMF voltage of the motor is approximately 150 V at this speed. The current can flow from APO sub-system through power inverter diodes into DC-link. The required torque was set to zero during simulation. The simulation

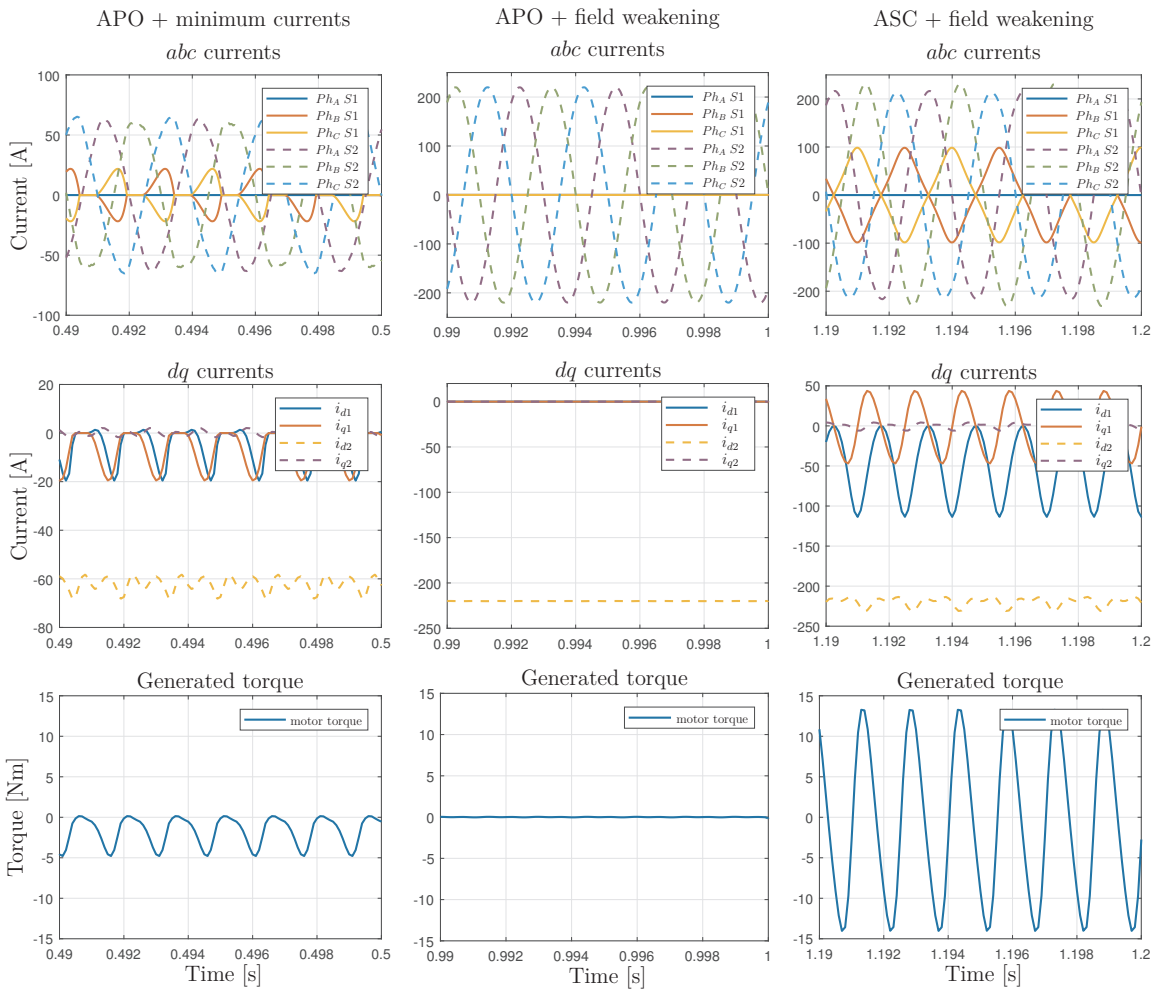

Fig. 6.13: Disconnected phase simulation results (no generated torque).

results are shown in set of Figures 6.13. The behaviour of motor with damaged sub-system switched into APO is shown in left column. The active sub-system does not generate torque, hoverer, field weakening needs to be active due to the higher back-EMF voltage compared to low DC-link voltage.

Mutual inductances between sub-systems are used to reduce the back-EMF voltage of the disconnected sub-system. This simulation is shown in the middle column. Active sub-system d current is significantly higher than required.

The last column shows damaged sub-system switched into ASC in combination with additional field weakening. Torque oscillations are the highest in this case. Therefore, the damaged sub-system should not be switched into ASC during this type of fault.

The motor generates zero torque during simulations. Another set of Figures 6.14 shows behaviour of damaged motor during torque generation. Motor required torque was set to 20 Nm during simulation.

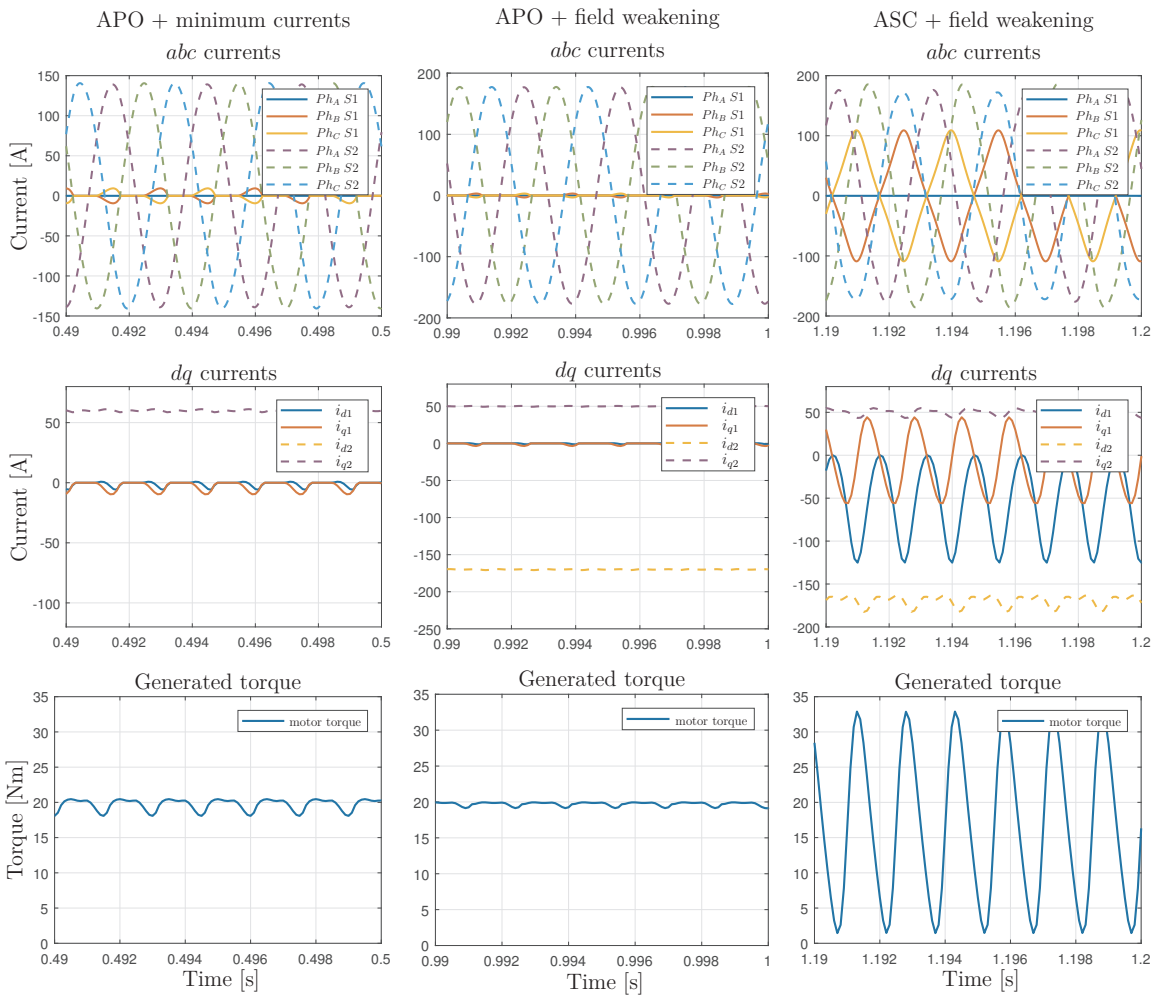

Fig. 6.14: Disconnected phase simulation results (20 Nm produced).

7 CONTROL METHOD FOR SEGREGATED MOTOR STRUCTURE OPERATING DURING THE FAULT

This chapter deals with the control algorithm for dual three-phase motor with segregated sub-systems. All figures included in this chapter are from real measurements.

The behaviour of the dual three-phase motor depends on its mechanical construction, as mentioned earlier. The parameters of the tested motor are given in Table 5.1. This motor was designed as a fault tolerant machine. The back-EMF voltage generated by the machine during maximum motor speed is lower than used DC-link voltage. The Inverter can be switched into an all phase open mode without undesirable current flow into the DC-link. During the motor inter-turn short-circuit or phase to phase short-circuit, the damaged motor sub-system can be switched to an active short-circuit mode as presented in chapter 6. Currents generated by the back-EMF voltage cause field weakening of the damaged sub-system. The current through the inter-turn short is narrowed by the field weakening.

The stator coil arrangement of the analyzed motor is shown in Figure 5.6. The behaviour of this motor can be simplified and described by the three-phase equivalent as it was already mentioned. An asymmetric behaviour can be observed especially during the faults. All six-phases need to be considered during the faults.

The motor winding is divided into six phases. Each phase has its self-inductance and also mutual inductances to all other phases. Inductances can be described by the following matrix

$$\boldsymbol{L}_{abc_{12}} = \begin{bmatrix} L_a & L_{ab} & L_{ac} & M_{aa} & M_{ab} & M_{ac} \\ L_{ba} & L_b & L_{bc} & M_{ba} & M_{bb} & M_{bc} \\ L_{ca} & L_{cb} & L_c & M_{ca} & M_{cb} & M_{cc} \\ M_{aa} & M_{ab} & M_{ac} & L_a & L_{ab} & L_{ac} \\ M_{ba} & M_{bb} & M_{bc} & L_{ba} & L_b & L_{bc} \\ M_{ca} & M_{cb} & M_{cc} & L_{ca} & L_{cb} & L_c \end{bmatrix} = \begin{bmatrix} \boldsymbol{L}_{abc} & \boldsymbol{M}_{abc} \\ \boldsymbol{M}_{abc} & \boldsymbol{L}_{abc} \end{bmatrix} \quad (7.1)$$

Individual items of $\boldsymbol{L}_{abc_{12}}$ are not constants. The inductance of each phase is a

function of rotor position. Individual values are defined in (7.2).

$$\begin{aligned} L_a &= L_s + L_{\Delta m}\cos(2\theta) \\ L_b &= L_s + L_{\Delta m}\cos\left(2\theta - \tfrac{4\pi}{3}\right) \\ L_c &= L_s + L_{\Delta m}\cos\left(2\theta + \tfrac{4\pi}{3}\right) \\ L_{ab} &= L_{ba} = L_{S1} + L_{\Delta m}\cos\left(2\theta - \tfrac{2\pi}{3}\right) \\ L_{ac} &= L_{ca} = L_{S2} + L_{\Delta m}\cos\left(2\theta + \tfrac{2\pi}{3}\right) \\ L_{bc} &= L_{cb} = L_{S1} + L_{\Delta m}\cos\left(2\theta\right) \end{aligned} \tag{7.2}$$

L_s denotes the constant part of the inductance. Value $L_{\Delta m}$ corresponds to the inductance fluctuation magnitude which is given by the rotor geometry and used material permeability. The magnets are inserted inside the rotor. This type of the motor is known as the interior permanent magnet synchronous machine (IPMSM). Variable θ denotes the actual electrical position of the rotor. Maximum inductance is in rotor q axis. Individual inductances are shown in Figure 5.20.

Variables L_{S1} and L_{S2} describe the constant part of mutual inductances within one sub-system. Indexes take into the account distances between coils. (e.g. L_{S1} is for phases $a_1 - b_1$ and $b_1 - c_1$, L_{S2} is for phases $a_1 - c_1$)

Mutual inductances of sub-system border coils a and c differ from mutual inductances between the middle coil b and border coils. Mutual inductances between sub-systems can be seen in (7.3).

$$\begin{aligned} M_{aa} &\approx L_{sm} \\ M_{bb} &\approx L_{sm} \\ M_{cc} &\approx L_{sm} \\ M_{ab} &= M_{ba} \approx L_{M1} \\ M_{ac} &= M_{ca} \approx L_{M2} \\ M_{bc} &= M_{cb} \approx L_{M1} \end{aligned} \tag{7.3}$$

The geometrical distance between phase a of the first sub-system and phase a of another sub-system is the same as the geometrical distance between sub-systems. This holds for all three phases. The mutual inductance between coils with the same electrical angle is described by variable L_{sm}. Variables L_{M1} and L_{M2} denote other mutual inductances between sub-systems. These two values are not equal. The mutual inductance fluctuation between sub-systems is small enough to be neglected.

Equation (7.4) shows the relationship between the value of mutual inductances within a sub-system and the mutual inductance between sub-systems. This condition is given by the motor structure and is responsible for motor symmetry during normal operation.

$$L_{S1} + L_{M1} = L_{S2} + L_{M2} \tag{7.4}$$

The torque generated by the dual three-phase motor can be calculated using (7.5) as already mentioned in chapter 4.

$$T_e = Pp\left(\frac{1}{2}\boldsymbol{i}_{abc_{12}}^{\intercal}\frac{\mathrm{d}\boldsymbol{L}_{abc_{12}}}{\mathrm{d}\theta}\boldsymbol{i}_{abc_{12}} + \frac{\boldsymbol{i}_{abc_{12}}^{\intercal}}{\omega_e}\frac{\mathrm{d}\boldsymbol{\Psi}_{m_{abc_{12}}}}{\mathrm{d}t}\right) \tag{7.5}$$

Motor generated torque T_e consists of two parts. The first part in the brackets represents reluctance torque. The second part represents magnetic torque. Variable ω_e denotes the electrical speed of the motor. Pp represents the number of motor pole pairs.

7.0.1 Control Algorithm for Healthy Motor

During normal operation, both sub-systems operate with the same currents, $\boldsymbol{i}_{abc_1}$ equals to $\boldsymbol{i}_{abc_2}$. The motor behaviour of one sub-system can be described by its three phase equivalent. Standard approaches to the configuration of controller parameters can be used. The control algorithm uses maximum torque per ampere (MTPA) curve. The field weakening algorithm uses also maximum torque per volt (MTPV) curve. These methods improve behaviour in the high-speed region. The field weakening algorithm is based on [37, 38]. Decoupling or other advanced control method can be used for this type of motor during normal operation.

This behaviour is the advantage of multiple three-phase arrangements. The classical three-phase control algorithm in combination with the multiple three-phase inverters can be used for the healthy motor. Motor current is distributed into multiple sub-systems.

Both motor sub-systems were connected to one three-phase inverter during tests because high power six-phase inverter was not available at the time of experiments. The control algorithm was modified to operate with half of measurement currents to trace properly the MTPA curve. Motor currents were measured with an oscilloscope for verification. Measurement confirmed an even distribution of the current to both sub-systems. This behaviour was also predicted in simulations.

The testing operating point was chosen with regard to dynamometer capabilities. Mechanical speed was set to 3000 rpm. The torque generated by the motor was set to 50 Nm per one sub-system. The motor generates 100 Nm during normal operation, but only approximately 50 Nm during the fault.

Figure 7.1 shows measured motor currents during the test. The motor currents of both sub-systems are the same. The voltage vector trajectory generated by the inverter can be seen in Figure 7.2. The voltage vector trajectory for the classical motor is typically circular. Deviation from ideal circular shape is caused by harmonic distortion of back-EMF voltages and by the dead-time effect.

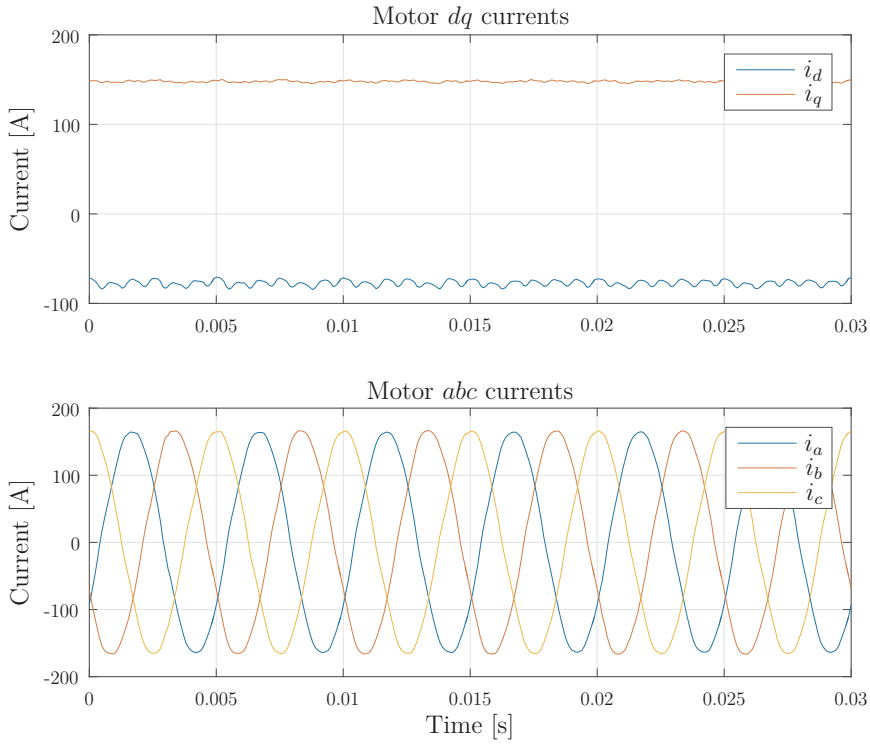

Fig. 7.1: Motor currents during normal operation (currents of both sub-systems are same).

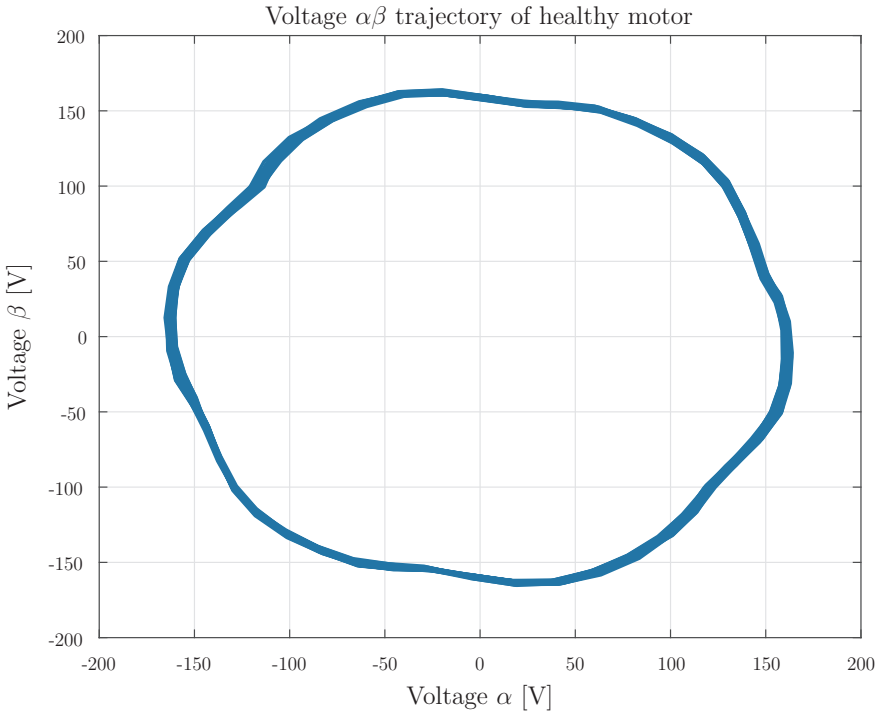

Fig. 7.2: Voltage vector trajectory during normal operation.

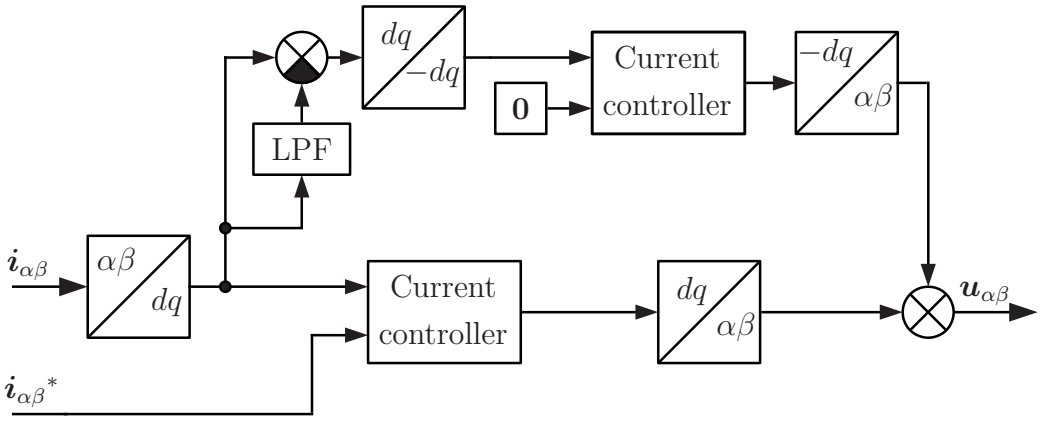

Fig. 7.3: The structure of proposed current controller with compensation.

7.0.2 Control algorithm for one active sub-system

This operating state is required if some part of the inverter is broken or if one motor phase is disconnected from the inverter. In this case one motor sub-system is switched to APO mode. The currents in this sub-system are equal to zero. The second sub-system can continue to operate.

The motor should generate smooth torque during fault state. $\boldsymbol{i}_{dq}$ should be constant without oscillations to generate smooth constant torque on the motor shaft. This condition comes from (7.5).

For inductances of the active motor part see (7.2). These inductances are not symmetric as required by the classical control algorithm. The voltage required to operate the motor with constant dq currents during this fault state is calculated using (7.6).

$$\boldsymbol{u}_{dq} = \boldsymbol{R}_{dq}\boldsymbol{i}_{dq} + \boldsymbol{T}\frac{\mathrm{d}\boldsymbol{L}_{abc}\boldsymbol{T}^{-1}}{\mathrm{d}t}\boldsymbol{i}_{dq} + \boldsymbol{L}_{dq}\frac{\mathrm{d}\boldsymbol{i}_{dq}}{\mathrm{d}t} + \boldsymbol{e}_{dq} \tag{7.6}$$

The time derivative of inductance matrix $\boldsymbol{L}_{abc}$ in combination with the transformation to dq coordinates defines cross-coupling. However, cross-coupling is the function of the rotor position in the asymmetrical system. Cross-coupling oscillations need to be taken into account by the control algorithm for the asymmetrical motor arrangement.

The inductance and transformation time derivative for one active sub-system can be simplified as described by (7.7). It consists of a rotor position dependent part and a constant part. The back-EMF voltage and resistance of coils are also symmetrical and can be considered as constants in dq coordinates.

Motor currents in abc coordinates have different amplitudes without the compensation. The influence of asymmetry is proportional to actual motor currents amplitude and operating speed - see (7.6) and (7.7).

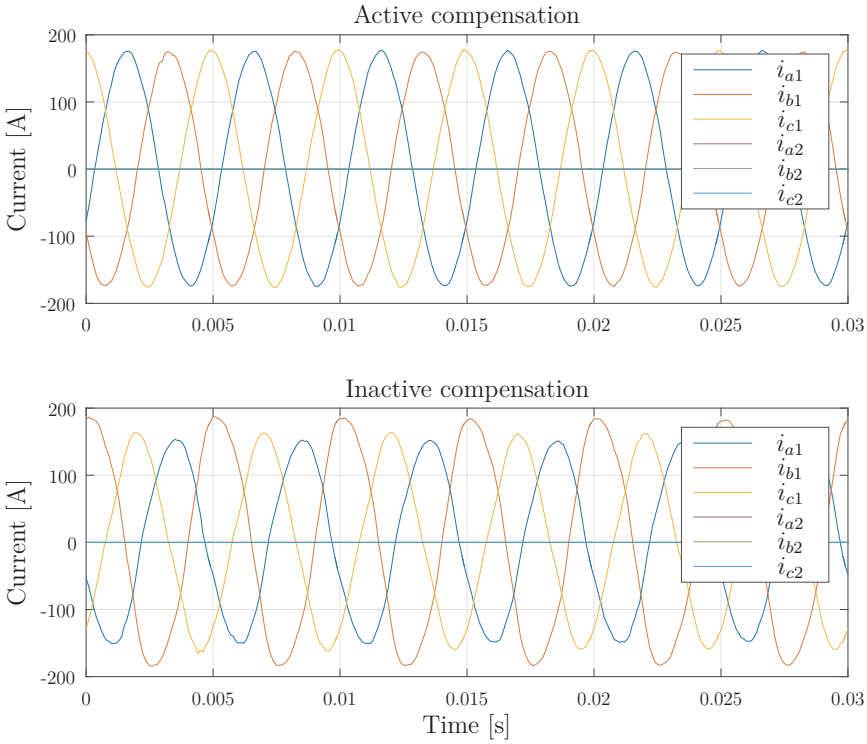

Fig. 7.4: Motor currents in *abc* coordinates.

$$\boldsymbol{T}\frac{\mathrm{d}\boldsymbol{L}_{abc}\boldsymbol{T}^{-1}}{\mathrm{d}t} = \boldsymbol{L}_{dq}^{S} + \boldsymbol{L}_{dq}^{A}$$
$$\boldsymbol{L}_{dq}^{A} = \frac{4\omega_e(L_{S1}-L_{S2})}{3}\begin{bmatrix} -\sin(2\theta-\frac{\pi}{3}) & \cos(2\theta-\frac{\pi}{3}) \\ \cos(2\theta-\frac{\pi}{3}) & \sin(2\theta-\frac{\pi}{3}) \end{bmatrix} \tag{7.7}$$
$$\boldsymbol{L}_{dq}^{S} = \omega_e\begin{bmatrix} 0 & \frac{2L_{S1}+L_{S2}}{3} - L_s + \frac{3}{2}L_{\Delta m} \\ L_s - \frac{2L_{S1}+L_{S2}}{3} + \frac{3}{2}L_{\Delta m} & 0 \end{bmatrix}$$

Motor terminal voltage $\boldsymbol{u}_{dq}$ can be divided into two parts. The first part is the symmetric voltage (7.8). The second part is asymmetric and calculated as in (7.9)

$$\boldsymbol{u}_{dq}^{s} = \boldsymbol{R}_{dq}\boldsymbol{i}_{dq} + \boldsymbol{e}_{dq} + \boldsymbol{L}_{dq}^{S}\boldsymbol{i}_{dq} \tag{7.8}$$

$$\boldsymbol{u}_{dq}^{a} = \boldsymbol{L}_{dq}^{A}\boldsymbol{i}_{dq} + \boldsymbol{L}_{dq}\frac{\mathrm{d}\boldsymbol{i}_{dq}}{\mathrm{d}t} \tag{7.9}$$

Currents in *dq* coordinates are constant in steady state. The time derivative of *dq* currents is thus neglected. The result after transformation from *dq* coordinates

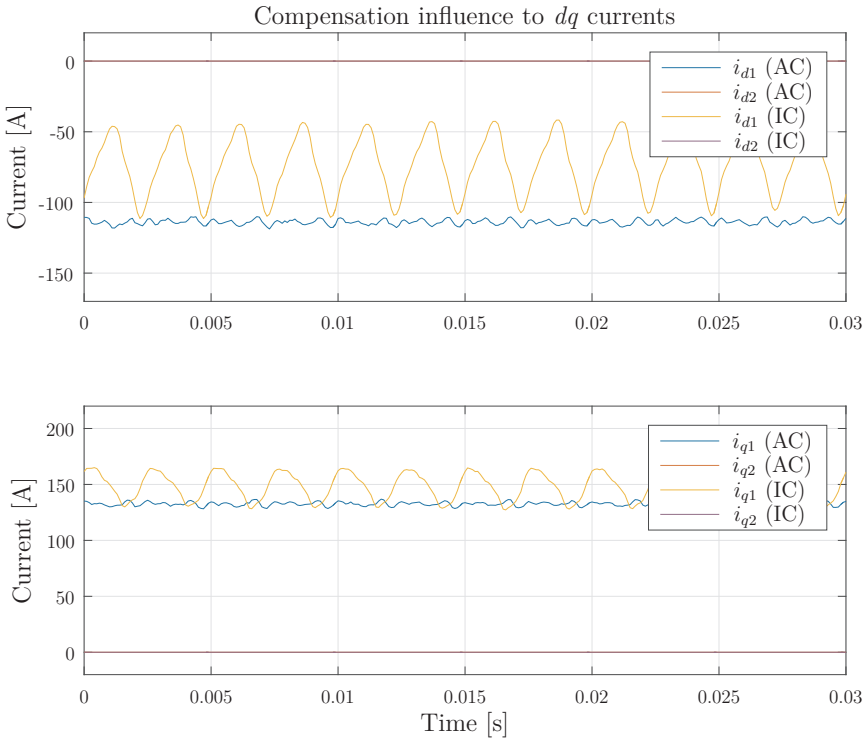

Fig. 7.5: Motor currents in dq coordinates (AC for active compensation IC for inactive compensation).

into stator $\alpha\beta$ coordinates is given in (7.10).

$$\boldsymbol{u}_{\alpha\beta} = \begin{bmatrix} -\sin(\theta - \frac{\pi}{3}) & \cos(\theta - \frac{\pi}{3}) & \cos(\theta) & \sin(\theta) \\ \cos(\theta - \frac{\pi}{3}) & \sin(\theta - \frac{\pi}{3}) & -\sin(\theta) & \cos(\theta) \end{bmatrix} \begin{bmatrix} u_d^a \\ u_q^a \\ u_d^s \\ u_q^s \end{bmatrix} \tag{7.10}$$

$$\text{where} \quad u_d^a = {}^4\!/_3 I_d \omega_e (L_{S1} - L_{S2}) \text{ and } u_q^a = {}^4\!/_3 I_q \omega_e (L_{S1} - L_{S2}).$$

Variables u_d^s and u_q^s give the amplitude of the circular voltage trajectory for the motor as shown in (7.10). The other two items u_d^a and u_q^a generate a second circular voltage trajectory. This second trajectory is shifted and the direction of this circular trajectory is the opposite. The sum of both trajectories generates an ellipse. From the geometrical point of view, ideal motor currents are generated by ellipsoidal voltage trajectory. Ellipsoidal distortion is proportional to the speed and to actual motor currents as seen from u_d^a and u_q^a. Ellipsoidal distortion compensation is calculated for the control algorithm using additional counter-directional controller. The first controller calculates u_d^s and u_q^s values. The second controller calculates u_d^a and u_q^a voltages. The block diagram of the controller with compensation is shown in Figure 7.3.

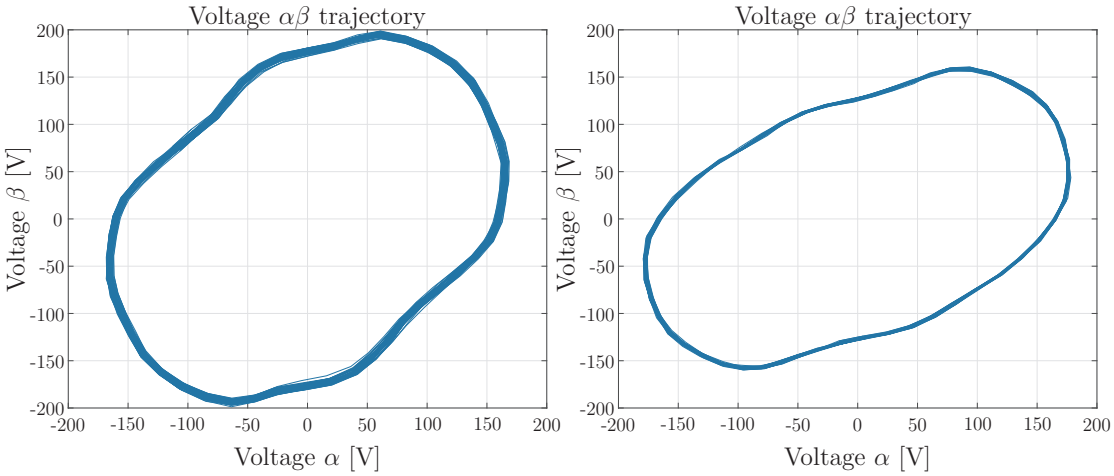

(a) Inactive compensation (b) Active compensation

Fig. 7.6: Voltage trajectories for a run with and without compensation.

For easier comparison, the test was carried out at the same operating point as during normal operation tests. The influence of additional compensation can be seen in Figure 7.4. It is also well demonstrated by currents in *dq* coordinates shown in Figure 7.5. Motor currents with active compensation are smoother than currents without compensation. The voltage generated by the control algorithm without compensation is deformed as shown in Figure 7.6 (a). However, the classical control algorithm is not fast enough to generate the required elliptical distortion. Voltage trajectory generated by the control algorithm with compensation is shown in Figure 7.6 (b). The control algorithm is able to adaptively compensate for different inductance asymmetry without online inductance identification.

7.0.3 Compensation of ASC sub-system

Motor sub-system needs to be switched into ASC during some fault. One sub-system of this motor can be switched into ASC, however, motor currents of damaged sub-system are not balanced due to an asymmetry inductances within the sub-system. This behaviour is shown in chapter 5.3.1. A damaged sub-system generates torque ripples, however ASC is required during some type of fault as inter-turn short-circuit or phase to phase short-circuit.

ASC sub-system currents cannot be controlled. However, the construction of the motor takes this information into account, so that ASC mode of one sub-system does not cause overcurrent or thermal damage to the motor. This ASC mode is very important in a view of the field weakening of a defective sub-system. Back-EMF voltage is significantly reduced in this case.

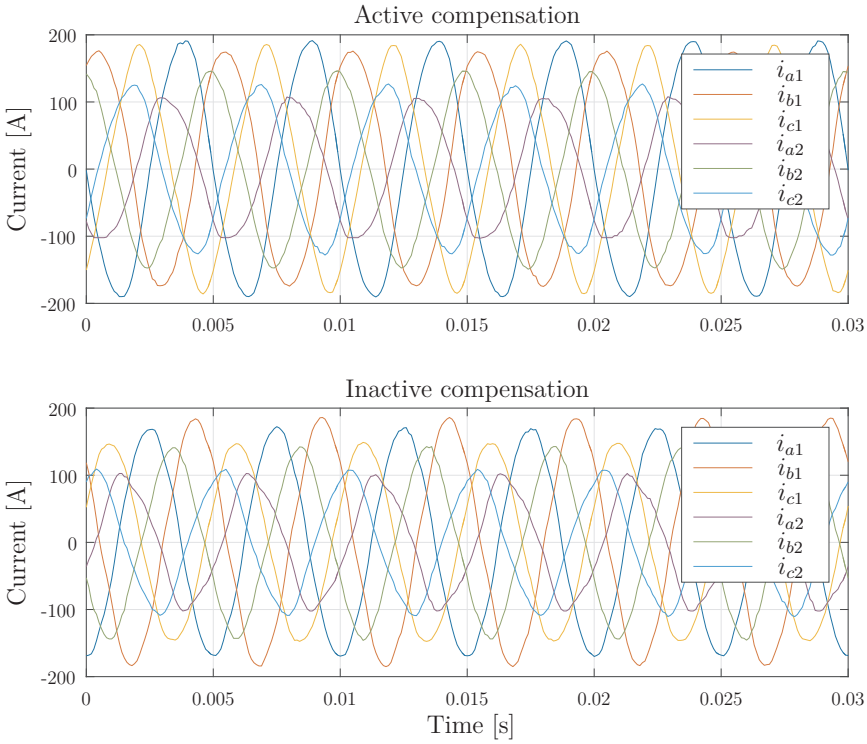

Fig. 7.7: Motor currents in *abc* coordinates.

Torque ripples generated by ASC current can be reduced using the active sub-system. The control algorithm is adapted to generate torque ripples with the same magnitude and opposite phase.

$$T_e = Pp\,(T_r + T_m) \tag{7.11}$$

The motor torque in (7.5) can be divided into a reluctance T_r and magnetic T_m part (7.11). The magnetic torque of the whole motor is composed of the sum of the magnetic torques of all sub-systems. The same principle applies to reluctance torque as the mutual inductance fluctuation is low. Controlled current i_{q_1} oscillations must have the same amplitude and opposite phase as the ASC sub-system current i_{q_2} according to (7.12).

$$T_m = \frac{\boldsymbol{i}_{abc_{12}}^{\intercal}}{\omega}\frac{\mathrm{d}\boldsymbol{\Psi} m_{abc_{12}}}{\mathrm{d}t} = \boldsymbol{i}_{dq_{12}}^{\intercal}\frac{3}{2}\begin{bmatrix}0\\ \lambda_m\\ 0\\ \lambda_m\end{bmatrix} \tag{7.12}$$

$$\frac{\mathrm{d}(i_{q_1})}{\mathrm{d}t} = -\frac{\mathrm{d}(i_{q_2})}{\mathrm{d}t} \tag{7.13}$$

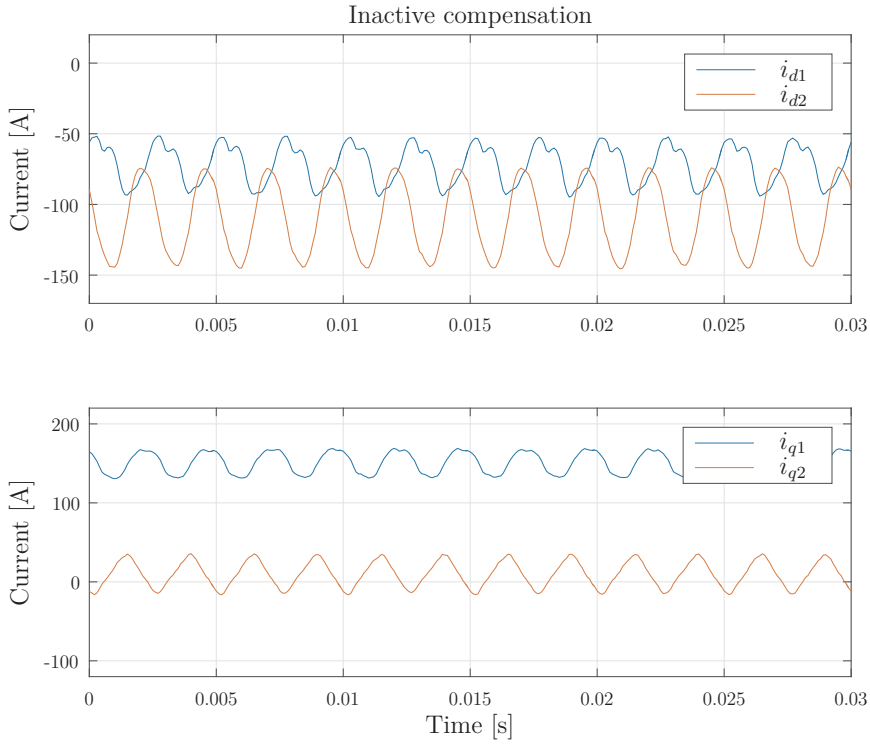

Fig. 7.8: *dq* currents of controlled and ASC sub-systems with classical FOC algorithm.

The condition for magnetic torque oscillations compensation is given in (7.13)

$$T_r = \frac{1}{2}\boldsymbol{i}_{abc_{12}}^{\intercal}\frac{\mathrm{d}\boldsymbol{L}_{abc_{12}}}{\mathrm{d}\theta}\boldsymbol{i}_{abc_{12}} = \frac{1}{2}\boldsymbol{i}_{dq_{12}}^{\intercal}\begin{bmatrix} 0 & -3L_{\Delta m} & 0 & 0 \\ -3L_{\Delta m} & 0 & 0 & 0 \\ 0 & 0 & 0 & -3L_{\Delta m} \\ 0 & 0 & -3L_{\Delta m} & 0 \end{bmatrix}\boldsymbol{i}_{dq_{12}} \tag{7.14}$$

The reluctance torque value depends on a product of i_d and i_q as shown in (7.14). The condition for reluctance torque oscillations reduction is given in (7.15).

$$\frac{\mathrm{d}i_{d_1}i_{q_1}}{\mathrm{d}t} = -\frac{\mathrm{d}i_{d_2}i_{q_2}}{\mathrm{d}t} \tag{7.15}$$

The control algorithm uses the combination of required currents calculated according to derived conditions (7.13, 7.15) and of the earlier mentioned additional counter-directional controller which is able to generate an elliptical stator voltage vector. This combination of control methods makes it possible to follow the required current oscillations for torque ripples reduction. Figure 7.7 shows measured motor *abc* currents using the classical FOC algorithm compared to the algorithm with torque ripples compensation. Current oscillations presented in Figure 7.8 have

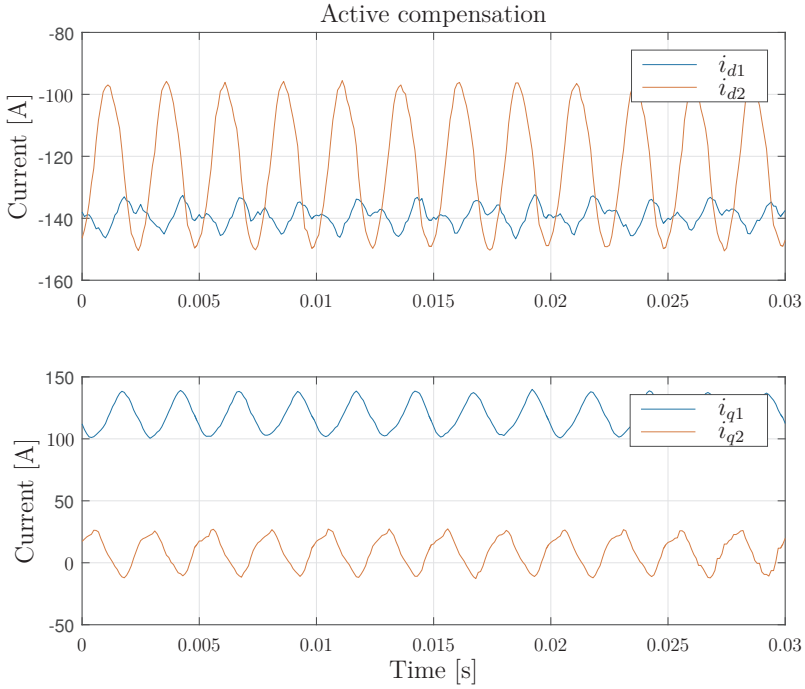

Fig. 7.9: dq currents of controlled and ASC sub-systems with compensation algorithm.

higher amplitudes compared to the current oscillations with active compensation (see Figure 7.9).

i_q current oscillations using the compensation have opposite phases. The second condition stipulated in (7.15) is also fulfilled. Acoustic noise generated by the motor was reduced by the proposed compensation.

The voltage trajectory required to compensate torque oscillations can be seen in Figure 7.10 (b). The voltage vector without additional compensation methods is shown in Figure 7.10 (a).

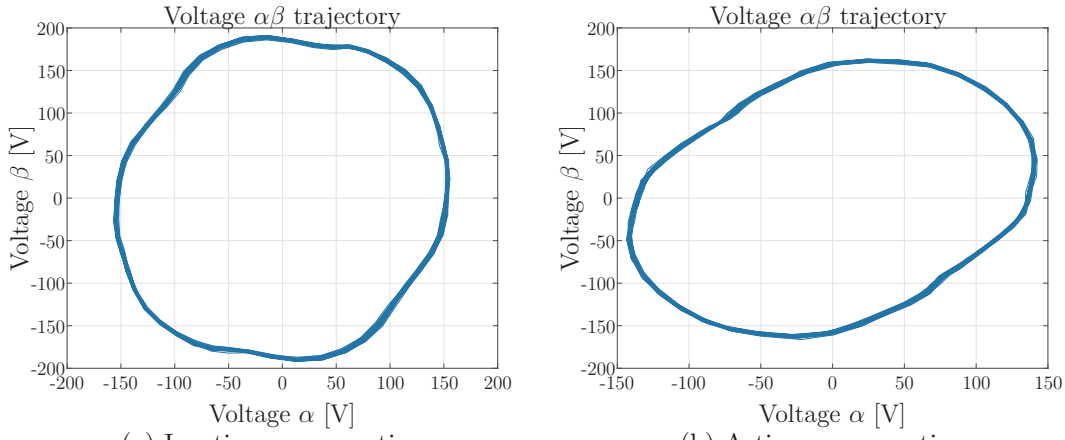

(a) Inactive compensation (b) Active compensation

Fig. 7.10: Voltage trajectories for the operation without and with the compensation

8 FAIL OPERATIONAL CONTROL ALGORITHMS TESTS

The fail operational control algorithm is based on the analysis described in chapter 6. Fail operational control algorithm consists of two essential parts. The first one is a fault detection algorithm and online diagnostics. Online diagnostics is based on algorithms described in [39, 40, 41, 42]. These algorithms provide information about the actual motor fault.

Another part is a control algorithm with implemented compensation strategies. Compensation strategies must respect the motor structure and behaviour during the fault. Proper compensation strategy needs to be selected using the information about the actual motor fault. Control algorithm needs to to be dynamically changed during the motor operation in case of any fault appearance.

Three core microcontroller AURIX TC275 from Infineon is used during the real experiments. The control algorithm is integrated in two cores. Each core is dedicated to one motor sub-system. Internal logical structure of the microcontroller and connection to the power stage and experimental motor can be seen in Figure 8.1.

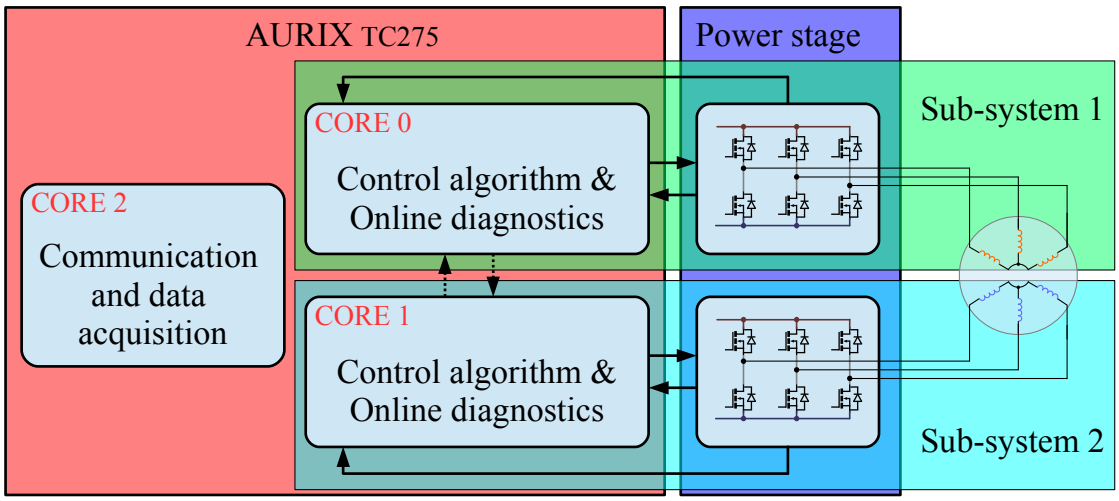

Fig. 8.1: Structure of testing system.

The last core is dedicated to communication and data acquisition. System is connected to PC using Ethernet communication. Individual waveforms are sampled once per PWM cycle. Same communication interface is used to control the system. MATLAB/Simulink is used on the PC to store data and send control commands.

8.1 Control algorithm implementation into microcontroller

The basic principle of control algorithm implementation for a dual three-phase motor does not deviate from an implementation of three-phase motor control algorithm. So as to gain more from the redundancy built in the motor, the controller was also realized as a system with redundancy. The whole control structure is designed as two separable parts. Each part controls one sub-system and each part operates in a separate core of a multi-core microcontroller. This structure enables to finally realize a highly reliable drive system as 1-out-of-2 architecture with diagnostics. A similar approach can be used in an inverter which is created as a combination of two separated three-phase power inverters. Individual parts share position information and measured motor currents. They are also interconnected to share information about actual control algorithm state and required compensation. The interconnection of control algorithms for individual sub-systems is shown in Figure 8.2.

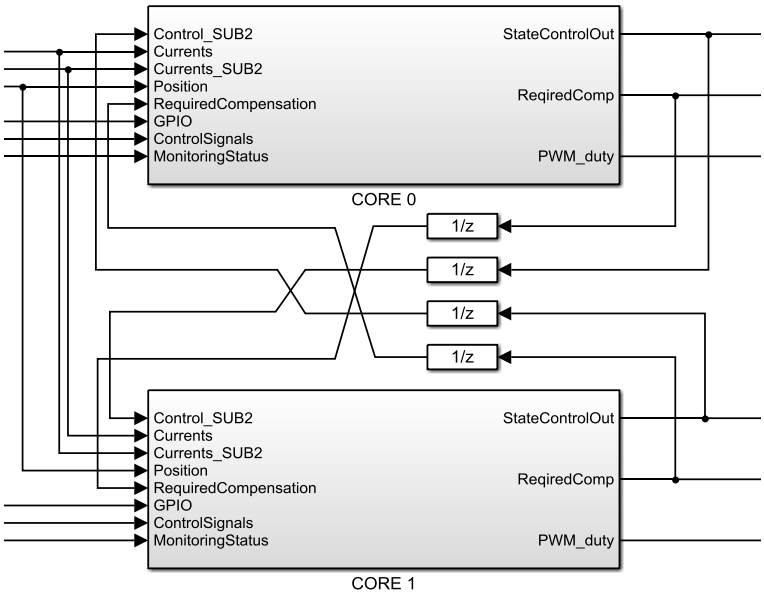

Fig. 8.2: Control algorithm interconnection.

Control signals provided by the supervisor system are distributed into both cores. If both sub-systems are equally loaded, maximum power efficiency is reached. GPIO inputs are used for power stage diagnostics signals. The control algorithm for each sub-system consists of following parts:

- Position pre-processing
- Current pre-processing
- Core state machine

- Control kernel
- Fault controller

8.1.1 Position pre-processing

This algorithm is responsible for the proper position and speed calculation. An angle tracking observer (ATO) is used for this purpose. It is well suited to estimate the motor speed using an encoder sensor. Nevertheless, ATO can also reduce the noise and improve the performance of analog sensors, for instance GMR/AMR sensors. Position pre-processing part calculates two sets of SinCos signals. The first set is used as a motor position during sampling. Another set is shifted by 1.5 sampling periods multiplied with the rotor angular speed. Shifted SinCos signal is used to transform voltage from *dq* coordinates into *abc* coordinates. This method compensates computational and discretization time delay which improves control algorithm behaviour, mainly in a high speed region.

8.1.2 Current pre-processing

The detailed structure of the current pre-processing module is shown in Figure 8.3. This part of the control algorithm can operate in two modes. The first mode is the initialization. The second one is the online sensor diagnostics mode. The offset of individual current sensors is calculated during initialization. The average value is calculated using a filter with a high time constant. The average value is compared with the limits. If the average value is exceeded, corresponding sensor is marked by the fault flag.

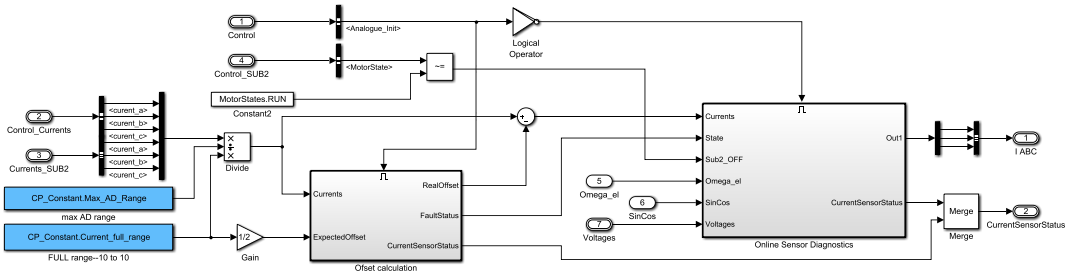

Fig. 8.3: Current pre-processing structure.

Online sensor diagnostics mode converts measured currents from ADC units into amperes and monitors the sensor's performance. If a fault appears, the module detects damaged sensor and calculates correct motor currents using healthy sensors and the motor model. If two motor sensors are damaged or overcurrent is detected, the module sends a request to activate the fault controller module.

8.1.3 Core state machine

The state machine is responsible for the proper initialization of the control algorithm and the power stage. Safety features as HW self-diagnostic can be performed during the start-up process. State machine processing feedback signals from power inverter (GPIO signals) as well as status signals from pre-processing algorithms (current pre-processing, position pre-processing). Control kernel is started after successful HW and SW initialisation. If any critical fault appears during initialisation or during the controller operation, the fault controller algorithm is activated instead of the control kernel part.

8.1.4 Control kernel

The FOC algorithm is evaluated by the control kernel. The internal structure of the control kernel is shown in Figure 8.4. Transformations convert measured currents from the stator *abc* coordinate system into rotor *dq* coordinates.

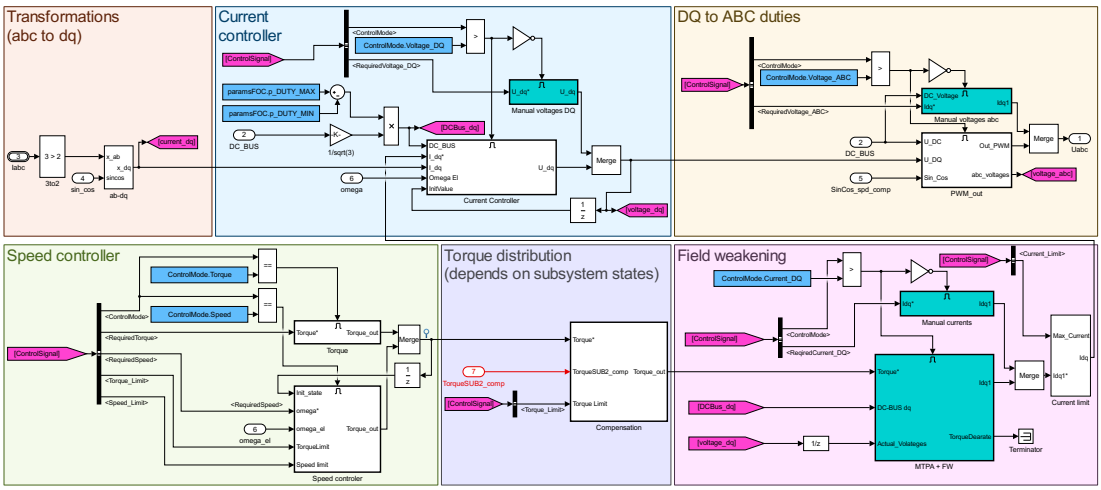

Fig. 8.4: Control kernel structure in Simulink.

The control kernel encompasses compensation features described in chapter 7 and principles for control during the fault described in chapter 6. The decoupling algorithm is also involved to achieve high-speed operation. A field weakening algorithm is necessary to reach the maximum speed of the experimental motor which is

used during the tests. Torque distribution part is active only during the fault. If one sub-system is switched into the fault mode, the torque generated by the healthy sub-system needs to be rapidly increased to replace the torque drop-out caused by the loss of faulty sub-system. Torque oscillations caused by faulty sub-system are compensated by implemented compensation strategies.

8.1.5 Fault controller

The fault controller is active during any critical fault in the sub-system. For example, damaged multiple current sensors, or power inverter fault. The fault controller has information about the fault and chooses an optimal operating mode for the damaged sub-system. Selected operating mode must be achievable. For example, active field weakening (AFW) can be achieved only if the position sensor, currents measurement and the power stage operate properly. This fault mode is suitable especially during the motor electrical faults.

All phase open (APO) and active short-circuit (ASC) modes are suitable for power stage faults. ASC can be used in combination with the short-circuited power transistor. APO can be used up to motor nominal speed in combination with the power transistor driver fault. The ASC mode does not require information about the motor position or even information about the actual motor speed. ASC in both motor sub-systems can be used if multiple faults occur. Table 8.1 shows the combination of faults and recommended operation modes.

Tab. 8.1: Suggested operation modes during faults

Inverter Fault / Motor Fault	No fault	Transistor short-circuited	Transistor open-circuited	Sensor damaged
No fault	Normal operation	ASC	APO	ASC/APO
Open-circuit inside of the sub-system	APO	APO	APO	APO
Short-circuit inside of the sub-system	ASC/AFW	ASC	ASC	ASC

8.2 Control algorithm test

During the test, an experimental dual three-phase motor was used. Experimental motor parameters are shown in appendix B. It has four taps prepared in one coil. This coil with 25 turns is divided in the ratio 1:1:3:6:14. Ten different short-circuit depths can be emulated using this arrangement. The short-circuit is formed by using the fault insertion unit (FIU) based on galvanically separated solid state relay with the internal resistance R_f =0.05 Ω and equipped with the IC for current measurement.

The test bench consists of the experimental dual three-phase motor mechanically coupled with the dynamometer. The power inverter is composed from two three-phase power stages connected to the control board represented by ApplicationKit with Infineon AURIX TC275 microcontroller. The motor operates in a speed mode. The dynamometer generates constant load torque T_L = 0.5 Nm and all tests are executed at electrical speed 2200 rad/s. A detailed look on the experimental motor and test bench is shown in appendix C.

8.2.1 Short-circuited power stage transistor

During the experiment, the bottom transistor in phase C was permanently switched on by the software. This behaviour is equal to short-circuiting the bottom transistor. In Figure 8.5, the time axis is associated with the fault event and the fault is emulated at time $t = 0$ s. Phase current C of damaged sub-system cannot be positive anymore and the current waveform can be seen in Figure 8.5 (a) top. The distorted currents generate torque oscillations.

The current waveforms with activated fault detection can be seen in Figure 8.5 (b). The compensation strategy permanently switches on the bottom transistors in phases A and B, and current can now flow through all of the bottom transistors and the motor is switched into ASC mode.

The damaged sub-system now generates a low breaking torque which is compensated by the active sub-system and the motor can continuously operate under this fault.

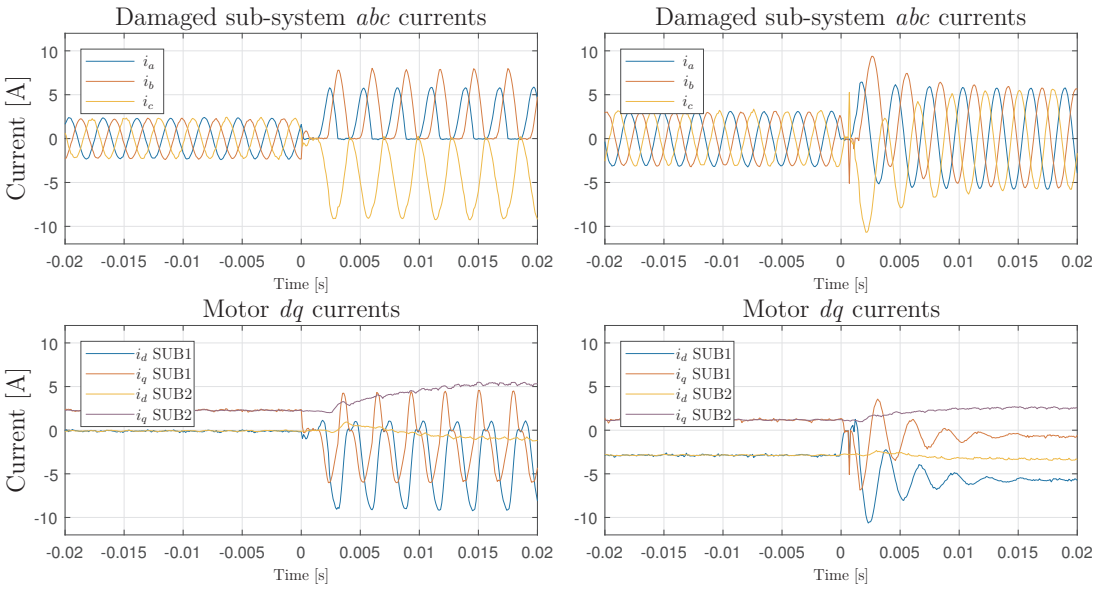

(a) Without fault detection

(b) With fault detection

Fig. 8.5: Motor currents during transistor short-circuit fault.

8.2.2 Disconnected power stage transistor

During the following experiment, the top transistor in phase C was permanently switched off by the software. Influence of this fault is similar to the previously described fault. Phase current C of damaged sub-system cannot be positive for this reason. This current waveform can be seen in Figure 8.6 (a) top. Distorted currents transformed into *dq* coordinates are shown in Figure 8.6 (a) bottom. Torque ripples and vibrations are generated in the damaged sub-system.

This fault is typically detected by the power stage hardware. The fault typically generates desaturation fault which is detected by the transistor driver. Compensation strategy can switch the whole sub-system into APO mode. APO mode results in zero currents in damaged sub-system. Behaviour using the APO mode is almost the same as shown in Figure 8.9 (b). Fault detection time is reduced, because the fault is detected by HW.

ASC compensation strategy should be used for high speed operation. ASC permanently switches on all bottom transistors of the damaged sub-system. In the case of this fault in one of the bottom transistors, all top transistors are switched on. The motor can continuously operate under this fault with an active compensation strategy.

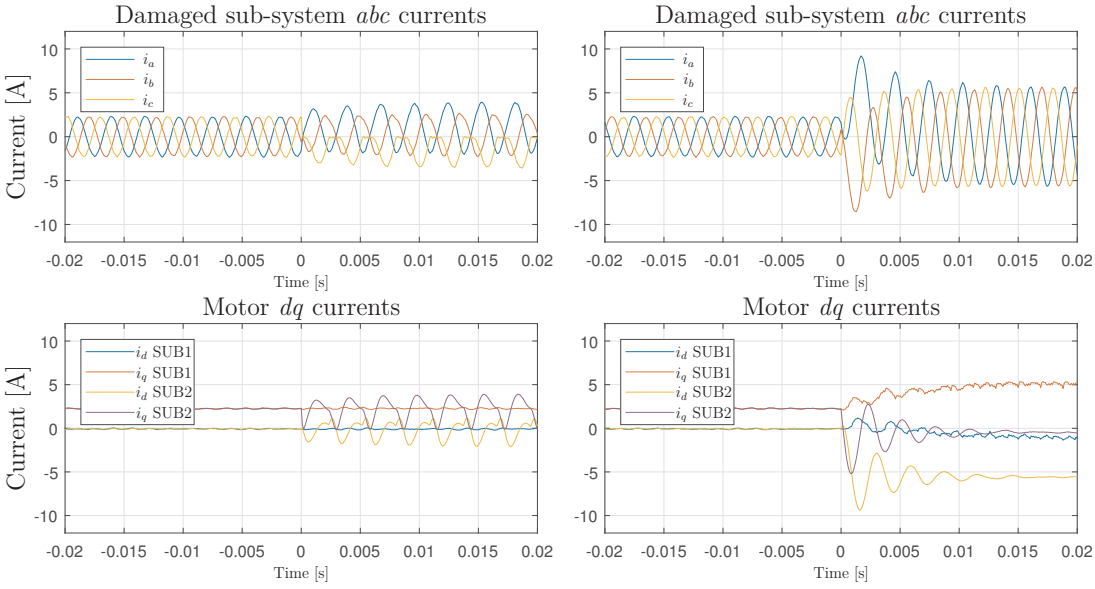

(a) Without fault detection

(b) With fault detection

Fig. 8.6: Motor currents during disconnected transistor fault.

8.2.3 Interturn short-circuit

Interturn fault was emulated using the experimental motor winding taps. Experimental motor has 18 coils. Each coil has 25 turns. One phase winding consists of three stator coils connected in series. During the fault, 6 turns of the coil within the phase C are short-circuited. Current waveforms of the damaged sub-system are distorted by the fault current. This fault generates only relatively small torque ripples, however, the fault current amplitude is in general high enough to generate very fast local increase of the temperature. It subsequently damages other coil turns. Motor currents and a fault current can be seen in Figure 8.7 (a).

Implemented compensation strategy switches damaged sub-system into ASC mode. Sub-system is field weakened and fault current is reduced. Fault detection time was approximately 15 ms. Current waveforms with activated fault detection can be seen in Figure 8.7 (b).

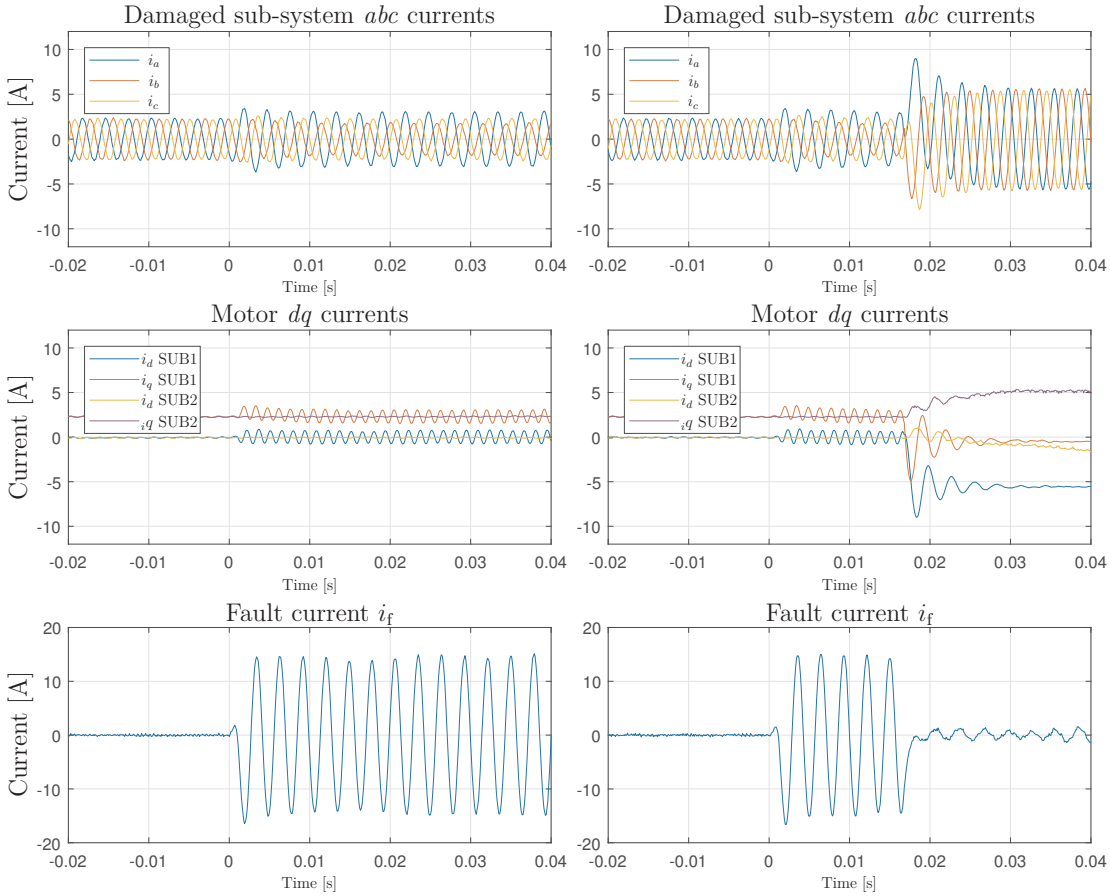

(a) Without fault compensation (b) With fault detection and compensation

Fig. 8.7: Motor currents during interturn short-circuit fault.

8.2.4 Phase to phase short-circuit

This fault is similar to the interturn short-circuit fault. Even the detection algorithm is the same. The phase winding C was connected with the phase winding B. Short-circuit was generated in a distance of 13 turns from the sub-system middle point. Motor currents during the fault are shown in Figure 8.8 (a).

Compensation strategy switches damaged sub-system into ASC. The fault current is significantly reduced and the motor can continuously operate. Motor currents using fault detection and its compensation is shown in Figure 8.8 (b).

AFW compensation strategy can be also used instead of ASC mode to increase motor performance during fail operation. AFW can be used for the interturn short-circuit as well as for the phase to phase short-circuit faults.

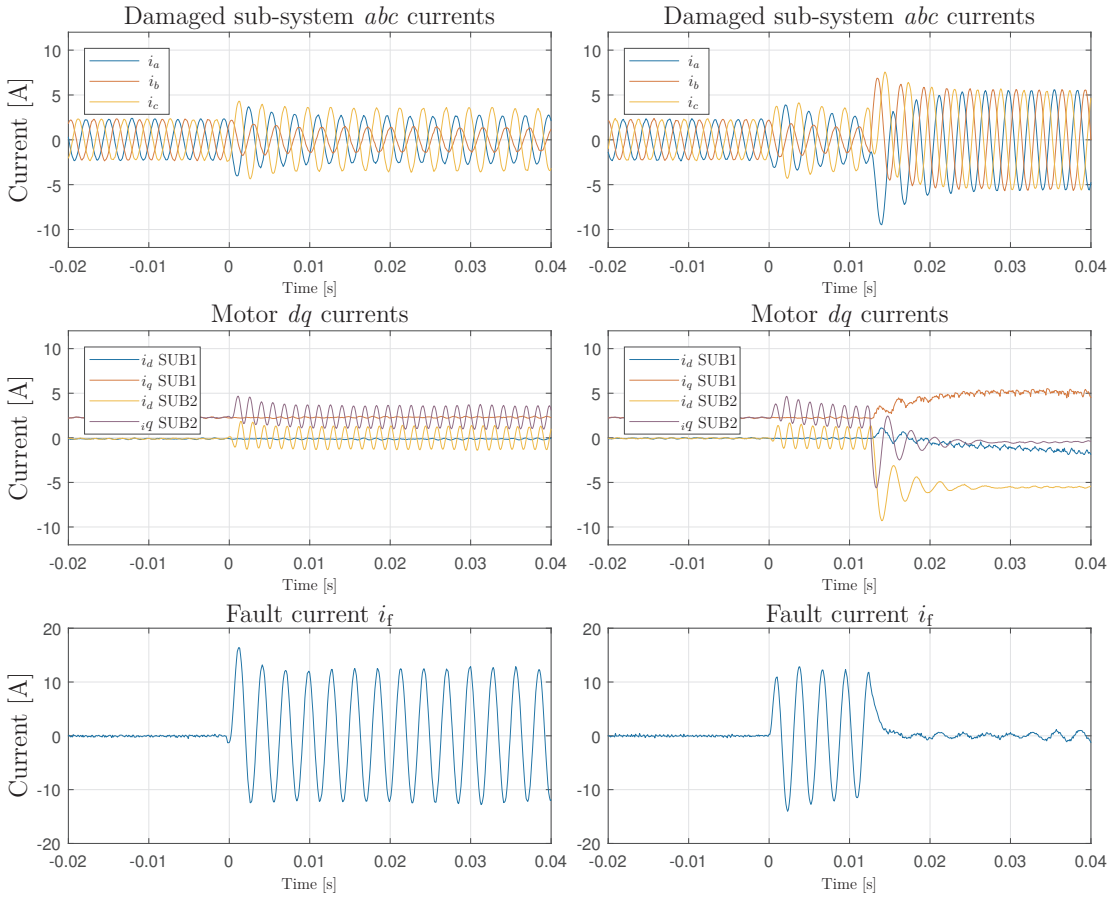

(a) Without fault detection (b) With fault detection and compensation

Fig. 8.8: Motor currents during phase to phase short-circuit fault.

8.2.5 Disconnected phase

This fault was emulated using the FIU in phase C. Phase currents are balanced during the normal operation, however, the current of disconnected phase is zero during the fault. The sum of additional two phase currents is equal to zero. The damaged sub-system can be switched into APO mode to reduce torque oscillations caused by this fault. The torque oscillation amplitude depends on the actual current amplitude and the actual motor speed. If the motor operates with a low load torque and a low speed region, the fault is difficult to detect. Motor phase currents without reaction to a fault can be seen in Figure 8.9 (a).

Reaction to the fault can be seen in Figure 8.9 (b). Currents of damaged sub-system are zero and the whole motor torque is generated by an active sub-system. The additional field weakening is forced into an active sub-system during operation in high-speed region to reduce back-EMF of damaged sub-system. Damaged sub-system cannot be switched into ASC mode in contrast to the fault described in chapter 8.2.2.

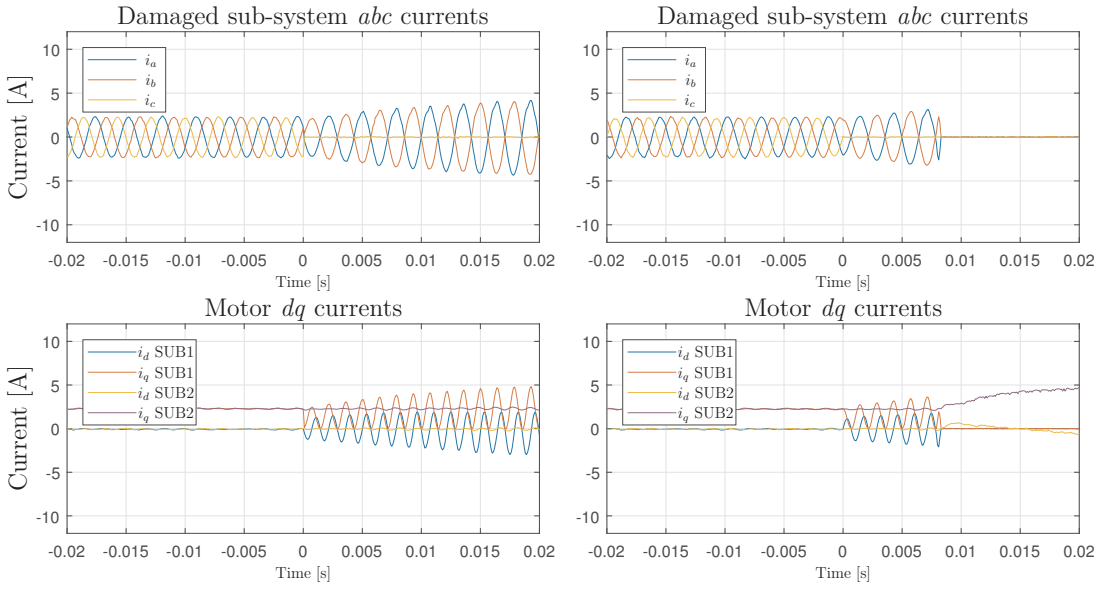

(a) Without the reaction to a fault

(b) With fault detection and reaction

Fig. 8.9: Motor currents during disconnected phase fault.

9 CONCLUSION

The dissertation aimed to analyse PMS motor faults, to design a mathematical model of electrical machines which would be suitable for modeling motor behaviour under fault conditions, and to suggest control strategies for the motor under different fault conditions. The fault detection, which is closely related to the presented topic, is not part of this work. The whole thesis is aimed especially to multi-phase motors with the stress on multiple three-phase configurations.

The thesis includes several multi-phase mathematical model derivations. All presented mathematical models are based on general multi-phase motor equations, which are included. Transformation matrices were used to derive the simplified triple three-phase motor model in dq coordinates. The model was implemented in MATLAB/Simulink. It is suitable especially for control algorithm design without fault. The model can be used to simulate a limited number of faults, for example, short-circuited power stage transistor. The model in combination with additional feedback can be also used to simulate disconnected winding. However, a short-circuit fault inside the motor cannot be simulated. The model with small modifications can be also used to simulate the behaviour of dual three-phase motors. Beyond the thesis objectives, the designed dq model was successfully integrated into one core of AURIX TC397 microcontroller. The optimized computational complexity of the model allows using it in real-time, for instance in HIL simulations.

The complexity of the created models increases with the possibility of modeling more types of faults. The further model was designed in the Simscape environment. It was formulated in stator coordinates to allow simulation of multiple faults. Finally, the model was extended to allow it to simulate different short-circuit faults inside the motor. The model is very general. It can simulate the behaviour of a general multi-phase motor, as well as the behaviour of multiple k-phase motors, up to nine phases. Motor behaviour depends on used parameters and chosen electrical connection in Simulink. This model allows simulating not only the behaviour during the fault but also the transient states. Universality is reached using general equations. However, the model presented here requires complete knowledge of motor inductances. A full motor inductance matrix is required for this model. The inductance matrix is defined as a function of rotor position to increase the model universality. The fault modeling principles to simulate internal short-circuit faults can be also used in the three-phase models.

Next part of this thesis deals with the analysis of different multi-phase structures. Achieved results suggest that the behaviour of different motor structures is almost the same under the normal operation conditions, however, each structure has its specific behaviour under the fault condition. Differences between individual

structures were explained and shown in simulations. Performed simulations have shown that the control algorithm for the operation of only one sub-system in fully symmetrical structures is much easier than the control algorithm for asymmetrical segregated structures. However, it is easier to isolate the fault using segregated structures due to lower magnetic coupling. Also, the motor performance under the fault condition is typically higher in asymmetrical structures.

Derived models were also used to analyse how the fault affects motor behaviour. Motor faults, as well as power inverter faults, were analysed. Detailed fault analysis shows that not every motor can be successfully controlled under all analysed fault conditions. The key factor is the field weakening index. Motor with high FWI cannot operate under the deep field weakening and therefore the maximum speed of the motors under short-circuit faults is significantly reduced. On the other hand, motors with low field weakening index (FWI<1) can be fully field weakened and the fault current caused by short-circuit faults can be significantly reduced.

The last part of this thesis deals with the verification of compensation strategies and designed control algorithms using real hardware. Control and compensation strategies were designed for two different dual three-phase motors. Compensation strategies designed for asymmetry segregated dual three-phase structure were able to generate harmonic currents even if only one sub-system has been working. The designed control algorithm generates lower torque ripples and acoustic noise in comparison with classical FOC. The motor was successfully controlled with one subsystem switched in ASC or APO mode. Results are outlined in chapter 7.

Compensation strategies for symmetry interlaced dual three-phase structures were successfully tested using an experimental dual three-phase motor. Power inverter transistor faults and also various motor short-circuit faults were emulated during the motor run. Implemented fault detection algorithms provide information about the motor fault and designed control algorithm successfully applied a suitable compensation strategy. After applying the proper control strategy the engine continued to operate with reduced peak power. Achieved results are presented in chapter 8.

It can be concluded that all the aims and objectives of the thesis were successfully achieved. Their fulfillment required additional work like programming the drivers for microcontroller peripherals, design of control algorithm for healthy multi-phase motor, becoming familiar with automatic C code generation in MATLAB/Simulink and its conditioning to AURIX microcontroller properties, preparation of test bench and the design of the experimental motor with failure insertion unit. These tasks are not detailed in this thesis because they partially go beyond the scope of this thesis and their inclusion would increase the extent significantly.

Future research could focus on control algorithm verification using a dual three-

phase motor of higher nominal power. The designed model could be also used as a background for current and position observers designed for dual three-phase machines. The model can be also advantageously used for the generation of training sets for learning artificial neural networks for fault detection.

BIBLIOGRAPHY

[1] ERTRAC, "Automated Driving Roadmap," tech. rep., ERTRAC, 2015. Available: https://www.ertrac.org/uploads/documentsearch/id38/ERTRAC_Automated-Driving-2015.pdf.

[2] Y. Chen, S. Liang, W. Li, H. Liang, and C. Wang, "Faults and Diagnosis Methods of Permanent Magnet Synchronous Motors: A Review," *Applied Sciences*, vol. 9, p. 2116, may 2019.

[3] R. Kianinezhad, B. Nahid-Mobarakeh, L. Baghli, F. Betin, and G.-A. Capolino, "Modeling and Control of Six-Phase Symmetrical Induction Machine Under Fault Condition Due to Open Phases," *IEEE Transactions on Industrial Electronics*, vol. 55, pp. 1966–1977, may 2008.

[4] M. Villani, M. Tursini, G. Fabri, and L. Castellini, "High Reliability Permanent Magnet Brushless Motor Drive for Aircraft Application," *IEEE Transactions on Industrial Electronics*, vol. 59, pp. 2073–2081, may 2012.

[5] N. K. Nguyen, F. Meinguet, E. Semail, and X. Kestelyn, "Fault-Tolerant Operation of an Open-End Winding Five-Phase PMSM Drive With Short-Circuit Inverter Fault," *IEEE Transactions on Industrial Electronics*, vol. 63, pp. 595–605, jan 2016.

[6] S.-K. Sul, *Control of Electric Machine Drive Systems (IEEE Press Series on Power Engineering)*. Wiley-IEEE Press, 1 edition ed., 2011.

[7] S. Ivanov, V. Defosse, F. Labrique, and P. Sente, "Control under normal and fault operation of a PM synchronous motor with physically and magnetically decoupled phases," in *2008 International Symposium on Power Electronics, Electrical Drives, Automation and Motion*, pp. 878–883, IEEE, jun 2008.

[8] R. Dobler, T. Schuhmann, R. B. Inderka, and S. V. Malottki, "High performance drive for electric vehicles — System comparison between three and six phase permanent magnet synchronous machines," in *2016 18th European Conference on Power Electronics and Applications (EPE'16 ECCE Europe)*, pp. 1–10, IEEE, sep 2016.

[9] T. Miller and M. McGilp, "Analysis of multi-phase permanent-magnet synchronous machines," in *2009 International Conference on Electrical Machines and Systems*, pp. 1–6, IEEE, nov 2009.

[10] M. de L. Pinheiro and W. I. Suemitsu, "Permanent magnet synchronous motor drive in vessels with electric propulsion system," in *2013 Brazilian Power Electronics Conference*, pp. 808–813, IEEE, oct 2013.

[11] E. Levi, R. Bojoi, F. Profumo, H. Toliyat, and S. Williamson, "Multiphase induction motor drives – a technology status review," *IET Electric Power Applications*, vol. 1, no. 4, p. 489, 2007.

[12] Hyung-Min Ryu, Ji-Woong Kim, and Seung-Ki Sul, "Synchronous-frame current control of multiphase synchronous motor under asymmetric fault condition due to open phases," *IEEE Transactions on Industry Applications*, vol. 42, no. 4, pp. 1062–1070, 2006.

[13] D. Casadei, M. Mengoni, G. Serra, A. Tani, and L. Zarri, "Optimal fault-tolerant control strategy for multi-phase motor drives under an open circuit phase fault condition," in *2008 18th International Conference on Electrical Machines*, pp. 1–6, IEEE, sep 2008.

[14] F. Wu, P. Zheng, and T. M. Jahns, "Analytical Modeling of Interturn Short Circuit for Multiphase Fault-Tolerant PM Machines With Fractional Slot Concentrated Windings," *IEEE Transactions on Industry Applications*, vol. 53, pp. 1994–2006, may 2017.

[15] A. G. Yepes, J. Doval-Gandoy, F. Baneira, D. Perez-Estevez, and O. Lopez, "Current Harmonic Compensation for n -Phase Machines With Asymmetrical Winding Arrangement and Different Neutral Configurations," *IEEE Transactions on Industry Applications*, vol. 53, pp. 5426–5439, nov 2017.

[16] Yashan Hu, Zi-Qiang Zhu, and Kan Liu, "Current Control for Dual Three-Phase Permanent Magnet Synchronous Motors Accounting for Current Unbalance and Harmonics," *IEEE Journal of Emerging and Selected Topics in Power Electronics*, vol. 2, pp. 272–284, jun 2014.

[17] B. Wang, J. Wang, B. Sen, A. Griffo, Z. Sun, and E. Chong, "A Fault-Tolerant Machine Drive Based on Permanent Magnet-Assisted Synchronous Reluctance Machine," *IEEE Transactions on Industry Applications*, vol. 54, pp. 1349–1359, mar 2018.

[18] MOTOR RELIABILITY WORKING GROUP, "Report of Large Motor Reliability Survey of Industrial and Commercial Installations, Part I," *IEEE Transactions on Industry Applications*, vol. IA-21, no. 4, pp. 853–864, 1985.

[19] MOTOR RELIABILITY WORKING GROUP, "Report of Large Motor Reliability Survey of Industrial and Commercial Installations, Part II," *IEEE Transactions on Industry Applications*, vol. IA-21, no. 4, pp. 865–872, 1985.

[20] MOTOR RELIABILITY WORKING GROUP, "Report of Large Motor Reliability Survey of Industrial and Commercial Installations: Part 3," *IEEE Transactions on Industry Applications*, vol. IA-23, pp. 153–158, jan 1987.

[21] D. Tian, L. Chen, L. Hou, and J. Pan, "Modeling and simulation of dual-three-phase induction machine with two opened phases," in *2008 IEEE International Conference on Industrial Technology*, pp. 1–5, IEEE, apr 2008.

[22] P. Giangrande, V. Madonna, S. Nuzzo, C. Gerada, and M. Galea, "Braking Torque Compensation Strategy and Thermal Behavior of a Dual Three-Phase Winding PMSM During Short-Circuit Fault," in *2019 IEEE International Electric Machines & Drives Conference (IEMDC)*, pp. 2245–2250, IEEE, may 2019.

[23] P. Brockerhoff, T. Ehlgen, Y. Burkhardt, and P. Lucas, "Electrical drivetrain without rare earth magnets and integrated inverter with inherent redundancy," in *2013 3rd International Electric Drives Production Conference (EDPC)*, pp. 1–7, IEEE, oct 2013.

[24] A. Glumineau and J. de León Morales, *Sensorless AC Electric Motor Control*. Advances in Industrial Control, Cham: Springer International Publishing, 2015.

[25] M. Villani, M. Tursini, G. Fabri, and L. Castellini, "Multi-phase permanent magnet motor drives for fault-tolerant applications," in *2011 IEEE International Electric Machines & Drives Conference (IEMDC)*, pp. 1351–1356, IEEE, may 2011.

[26] Y. Demir and M. Aydin, "A Novel Dual Three-Phase Permanent Magnet Synchronous Motor With Asymmetric Stator Winding," *IEEE Transactions on Magnetics*, vol. 52, no. 7, pp. 1–5, 2016.

[27] M. Xiong, Z. Liang, S. Hu, F. Li, and X. He, "Implementation of SVM-DTC on the Integration System with Hybrid Energy Storage and Dual Three-Phase PMSM," in *2018 IEEE Energy Conversion Congress and Exposition (ECCE)*, pp. 3375–3379, IEEE, sep 2018.

[28] Sang-Yong Jung, Yong-Jae Kim, Tae-Yong Lee, and Kyung-Won Jeon, "Numerical Shape Design Characteristics of Torque Ripple Reduction for Interior Permanent Magnet Synchronous Motor," in *9th IET International Conference*

on Computation in Electromagnetics (CEM 2014), pp. 5.08–5.08, Institution of Engineering and Technology, 2014.

[29] S. Lee, Y.-J. Kim, and S.-Y. Jung, "Numerical Investigation on Torque Harmonics Reduction of Interior PM Synchronous Motor With Concentrated Winding," *IEEE Transactions on Magnetics*, vol. 48, pp. 927–930, feb 2012.

[30] A. M. EL-Refaie, "Fractional-slot concentrated-windings synchronous permanent magnet machines: Opportunities and challenges," *IEEE Transactions on Industrial Electronics*, vol. 57, pp. 107–121, jan 2010.

[31] A. Pouramin, S. Ekanayake, R. Dutta, and M. F. Rahman, "Challenges for including characteristic current as a design parameter in optimization of IPM machines," in *2017 IEEE International Electric Machines and Drives Conference, IEMDC 2017*, pp. 1–6, IEEE, may 2017.

[32] M. Sanada and S. Morimoto, "Efficiency improvement at high-speed operation using large air-gap configuration for PMSM," in *2008 18th International Conference on Electrical Machines*, pp. 1–6, IEEE, sep 2009.

[33] EP Editorial Staff, "Large Electric Motor Reliability: What Did The Studies Really Say?," 2012.

[34] A. H. Bonnett, "Root cause failure analysis for AC Induction Motors in the petroleum and chemical industry," in *2010 Record of Conference Papers Industry Applications Society 57th Annual Petroleum and Chemical Industry Conference (PCIC)*, pp. 1–13, IEEE, sep 2010.

[35] W. Subsingha, "A Comparative Study of Sinusoidal PWM and Third Harmonic Injected PWM Reference Signal on Five Level Diode Clamp Inverter," *Energy Procedia*, vol. 89, pp. 137–148, jun 2016.

[36] K. B. Nagasai and T. Jyothsna, "Harmonic analysis and application of pwm techniques for three phase inverter," in *International Research Journal of Engineering and Technology*, pp. 1228–1233, 2016.

[37] A. Consoli, G. Scelba, G. Scarcella, and M. Cacciato, "An Effective Energy-Saving Scalar Control for Industrial IPMSM Drives," *IEEE Transactions on Industrial Electronics*, vol. 60, pp. 3658–3669, sep 2013.

[38] L. Sepulchre, M. Fadel, M. Pietrzak-David, and G. Porte, "MTPV Flux-Weakening Strategy for PMSM High Speed Drive," *IEEE Transactions on Industry Applications*, vol. 54, pp. 6081–6089, nov 2018.

[39] L. Otava and L. Buchta, "Implementation and verification of the PMSM stator interturn short fault detection algorithm," in *2017 19th European Conference on Power Electronics and Applications (EPE'17 ECCE Europe)*, pp. P.1–P.10, IEEE, sep 2017.

[40] L. Otava and L. Buchta, "Permanent magnet synchronous motor stator winding fault detection," in *IECON 2016 - 42nd Annual Conference of the IEEE Industrial Electronics Society*, pp. 1536–1541, IEEE, oct 2016.

[41] L. Otava, M. Graf, and L. Buchta, "Interior Permanent Magnet Synchronous Motor Stator Winding Fault Modelling," *IFAC-PapersOnLine*, vol. 48, no. 4, pp. 324–329, 2015.

[42] L. Otava and L. Buchta, "PMSM stator winding faults modelling and measurement," in *2015 7th International Congress on Ultra Modern Telecommunications and Control Systems and Workshops (ICUMT)*, pp. 138–143, IEEE, oct 2015.

PERSONAL PUBLICATION ACTIVITY

[43] M. Kozovský, "Control platform for multiphase motors," in *Proceedings of the 22nd Conference STUDENT EEICT 2016*, (Brno), pp. 416–420, Vysoké učení technické v Brně, Fakulta elektrotechniky a komunikačních technologií, april 2016.

[44] M. Kozovský, "Remote programming and monitoring of industrial devices using nat traversal and usb over ip," in *14th IFAC Conference on Programmable Devices and Embedded Systems*, pp. 258–263, october 2016.

[45] M. Kozovsky, P. Blaha, and P. Vaclavek, "Verification of nine-phase PMSM model in d-q coordinates with mutual couplings," in *2016 6th IEEE International Conference on Control System, Computing and Engineering (ICCSCE)*, pp. 73–78, IEEE, 2016.

[46] M. Kozovský, "Freertos implementation for hil simulation using aurix multicore," in *Proceedings of the 23nd Conference STUDENT EEICT 2017*, (Brno), pp. 471–474, Vysoké učení technické v Brně, Fakulta elektrotechniky a komunikačních technologií, april 2017.

[47] M. Kozovsky and P. Blaha, "Simulink generated control algorithm for nine-phase PMS motor," in *2017 7th IEEE International Conference on Control System, Computing and Engineering (ICCSCE)*, pp. 59–64, IEEE, nov 2017.

[48] M. Kozovský, "Matlab simulink code generation support for lin communication," in *Proceedings of the 24nd Conference STUDENT EEICT 2018*, (Brno), pp. 408–412, Vysoké učení technické v Brně, Fakulta elektrotechniky a komunikačních technologií, april 2018.

[49] M. Kozovsky and P. Blaha, "High Speed Operation Tests of Resolver Using AURIX Microcontroller Interface," *IFAC-PapersOnLine*, vol. 51, no. 6, pp. 384–389, 2018.

[50] M. Kozovsky and P. Blaha, "Double three-phase PMSM structures for fail operational control," *IFAC-PapersOnLine*, vol. 52, no. 27, pp. 1–6, 2019.

[51] J. Glos, M. Kozovsky, F. Solc, and P. Vaclavek, "Minimizing Power Consumption of Automotive AC System by Condenser Fan Speed Control," in *2020 IEEE 29th International Symposium on Industrial Electronics (ISIE)*, pp. 148–153, IEEE, jun 2020.

[52] L. Buchta, M. Kozovsky, and L. Otava, "Voltage disturbance observer for dual three-phase pmsm system," in *IECON 2020 - 46nd Annual Conference of the IEEE Industrial Electronics Society*, IEEE, aug 2020. accepted for publication.

[53] M. Kozovsky, L. Buchta, and P. Blaha, "Compensation methods of interturn short-circuit faults in dual three-phase pmsm," in *IECON 2020 - 46nd Annual Conference of the IEEE Industrial Electronics Society*, IEEE, aug 2020. accepted for publication.

LIST OF SYMBOLS, PHYSICAL CONSTANTS AND ABBREVIATIONS

Abbreviations

ADC	Analogue to digital converter
AFW	Active field weakening
AMR	Anisotropic magnetoresistance
APO	All phase open
ASC	Active short-circuit
ATO	Angle tracking observer
Back-EMF	Back electromotive force
DC	Direct current
FIU	Fault insertion unit
FOC	Field oriented control
FWI	Field weakening index
GMR	Giant magnetoresistance
IPMSM	Interior permanent magnet synchronous machine
MTPA	Maximum torque per ampere
MTPV	Maximum torque per volt
PMS	Permanent magnet synchronous
PMSM	Permanent magnet synchronous machine
PWM	Pulse-width modulation
SPWM	Sinusoidal pulse-width modulation
SVPWM	Space vector pulse-width modulation
THIPWM	Third-harmonic injection pulse-width modulation

Physical constants

$\boldsymbol{A}_i$	dq model feedback matrix
$\boldsymbol{A}_\Psi$	Back-EMF voltage feedback matrix
$\boldsymbol{B}$	dq model input matrix
B	Motor viscous friction coefficient
$\boldsymbol{C}_{dq}$	Motor dq coordinates cross-coupling matrix
$\boldsymbol{e}_{ab..n}$	General multi-phase motor back-EMF voltage vector
$\boldsymbol{e}_{abc}$	Three-phase motor back-EMF voltage vector
$\boldsymbol{e}_{abc_{123}}$	Triple three-phase motor back-EMF voltage vector
$\boldsymbol{e}_{abc_{123}}$	Extended triple three-phase motor back-EMF voltage vector
$\boldsymbol{e}_{abci}$	Three-phase back-EMF voltage vector of sub-system i
$\boldsymbol{e}_{dq}$	Motor back-EMF voltage transformed into dq coordinates
e_n	Back-EMF voltage of phase n
i	Current

$\boldsymbol{i}_{ab..n}$	General multi-phase motor current vector
$\boldsymbol{i}_{abc}$	Three-phase motor current vector
$\boldsymbol{i}_{abc_{123}}$	Triple three-phase motor current vector
$\boldsymbol{i}_{abci}$	Three-phase current vector of i^{th} sub-system
I_{ch}	Motor characteristic current
$i_{d_{\mathrm{ASC}}}$	Three-phase motor d axis currents during ASC operation
$i_{d_{\mathrm{ASC\_ALL}}}$	Multi-phase motor d axis currents during ASC in all sub-systems
i_{di}	d axis current of sub-system i
$i_{dj,\mathrm{ASC}}$	d axis currents of sub-system j during ASC operation
$\boldsymbol{i}_{dq}$	Motor dq coordinates current vector
$\boldsymbol{i}_{dq123}$	Current vector of all three motor sub-systems in dq coordinates
i_f	Fault current
I_f	Fault current amplitude
$i_{q_{\mathrm{ASC}}}$	Three-phase motor q axis currents during ASC operation
$i_{q_{\mathrm{ASC\_ALL}}}$	Multi-phase motor q axis currents during ASC in all sub-systems
i_{qi}	q axis current of sub-system i
$i_{qj,\mathrm{ASC}}$	q axis currents of sub-system j during ASC operation
I_s	Maximum allowed motor current
i_z	Motor/Sub-system current of z axis(α, β, d, q)/phase(a, b, c)
J	Motor moment of inertia
L	Inductance
$\boldsymbol{L}_{ab..n}$	General multi-phase motor inductance matrix
$\boldsymbol{L}_{abc}$	Three-phase motor inductance matrix
$\boldsymbol{L}_{abc_{123}}$	Triple three-phase motor inductance matrix
$\boldsymbol{L}^{e}_{abc_{123}}$	Extended triple three-phase motor inductance matrix
$\boldsymbol{L}_{abci}$	Three-phase inductance matrix of sub-system i
L_d	motor/sub-system d axis inductance
L_{di}	d axis inductance of motor sub-system i
L_{dq}	Mutual inductance between d and q axis of motor/sub-system
$\boldsymbol{L}_{dq}$	Motor inductance matrix transformed into dq coordinates
L_{it}	Inductance of the interturn short-circuit
L_{M_i}	Mutual inductances between sub-system (for windings in geometrical distance i)
L_{mn}	Mutual inductance between phases m and n within one sub-system
L_p	Inductance phase shift of fluctuation part
L_q	motor/sub-system q axis inductance
L_{qi}	q axis inductance of motor sub-system i
L_s	Inductance constant part
L_{S_i}	Constant part of mutual inductances within one sub-system (for

	windings in geometrical distance i)
L_z^{eq}	Equivalent three-phase motor z axis(d, q) inductance
$L_{\Delta m}$	Inductance fluctuation amplitude part
M	Mutual inductance
$\boldsymbol{M}_{abcij}$	Three-phase mutual Inductance matrix between sub-systems i and j
M_{dd}	Mutual inductance between d axis of motor sub-systems
M_{dq}	Mutual inductance between d axis of one sub-system and q axis of another sub-systems
M_{it}	Mutual inductance between the interturn short-circuit part and the rest of the damaged winding
M_{mn}	Mutual inductance between phases m and n between sub-systems
M_{qq}	Mutual inductance between q axis of motor sub-systems
$M_{yi,zj}$	Mutual inductance between y axis of sub-system i and z axis of sub-system j
n_0	Total number of phase winding turns
n_{it}	number of short-circuited winding turns during interturn fault
P_c	Motor continuous power
Pp	Motor pole-pairs
P_{pk}	Motor peak power
R	Resistance
$\boldsymbol{R}_{ab..n}$	General multi-phase motor resistance diagonal matrix
$\boldsymbol{R}_{abc}$	Three-phase motor resistance diagonal matrix
$\boldsymbol{R}_{abc_{123}}$	Triple three-phase motor resistance diagonal matrix
$\boldsymbol{R}^e_{abc_{123}}$	Extended triple three-phase motor resistance diagonal matrix
$\boldsymbol{R}_{abci}$	Three-phase resistance diagonal matrix of sub-system i
R_d	Motor/Sub-system d axis resistance
R_{di}	d axis resistance of sub-system i
$\boldsymbol{R}_{dq}$	Motor resistance transformed into dq coordinates
R_{it}	Resistance of the interturn short-circuit
R_q	Motor/Sub-system q axis resistance
R_{qi}	q axis resistance of sub-system i
R_s	Resistance of one motor phase
t	Time
T_{ASC}	Three-phase motor breaking torque during ASC
$\boldsymbol{T}_{abc\rightarrow dq_{123}}$	Transformation matrix from abc to dq coordinates for triple three-phase motor
T_c	Continuous motor torque
$\boldsymbol{T}_{dq}$	Park transformation matrix
$\boldsymbol{T}_{dq_i}$	Park transformation matrix of sub-system i

T_e	Generated motor torque
T_{fr}	Friction breaking torque
T_l	Motor load torque
T_M	Maximum motor torque
$\boldsymbol{T}_{\alpha\beta}$	Clarke transformation matrix
$\boldsymbol{T}_{\alpha\beta_i}$	Clarke transformation matrix of sub-system i
u	Voltage
u_0	Voltage reference
$\boldsymbol{u}_{ab..n}$	General multi-phase motor voltage vector
$\boldsymbol{u}_{abc}$	Three-phase motor voltage vector
$\boldsymbol{u}_{abc_{123}}$	Triple three-phase motor voltage vector
$\boldsymbol{u}_{abci}$	Three-phase voltage vector of sub-system i
u_{DC}	DC-link positive voltage
u_{di}	d axis voltage of sub-system i
$\boldsymbol{u}_{dq}$	Motor dq coordinates voltage vector
$\boldsymbol{u}_{dq123}$	Voltage vector of all three motor sub-systems in dq coordinates
u_f	Fault voltage
u_m	Motor/sub-system middle-point voltage
$\boldsymbol{u}_{m_{123}}$	Sub-systems middle-point voltage vector of triple three-phase motor
u_{qi}	q axis voltage of sub-system i
u_z	Motor/Sub-system voltage of z axis(α, β, d, q)/phase(a, b, c)
x_z	Motor variable (voltage/current) of z axis(α, β, d, q)/phase(a, b, c)
ε_e	Electrical angular acceleration
θ	Electrical angle between quadrature rotor axis q and motor phase a
θ_m	Mechanical rotor angle
θ_r	Electrical angle between direct rotor axis d and motor phase a
λ_m	Motor back-EMF constant
φ_i	Phase i electrical angle to reference phase
φ_i^*	electrical phase shift between sub-system i reference phase to motor reference phase
ψ_{di}	d axis magnetic flux of sub-system i
Ψ_M	Motor/sub-system permanent magnet flux
$\boldsymbol{\Psi}_{Mab..n}$	General multi-phase motor permanent magnet flux vector
ψ_{qi}	q axis magnetic flux of sub-system i
ω_e	Electrical motor speed
ω_m	Mechanical motor speed
ω_M	Mechanical motor maximum speed
ω_n	Mechanical motor nominal speed

LIST OF APPENDICES

A MATRICES

$$\boldsymbol{L}^{e}_{abc_{123}} = \begin{bmatrix}
\sigma_1^2 L_{a_1a_1} & \sigma_1^*\sigma_1 L_{a_1a_1} & \sigma_2\sigma_1 M_{a_1b_1} & \sigma_2^*\sigma_1 M_{a_1b_1} & \sigma_1 M_{a_1c_1} & \sigma_3\sigma_1 M_{a_1a_2} & \sigma_3^*\sigma_1 M_{a_1a_2} & \sigma_1 M_{a_1b_2} & \sigma_1 M_{a_1c_2} & \sigma_1 M_{a_1a_3} & \sigma_1 M_{a_1b_3} & \sigma_1 M_{a_1c_3} \\
\sigma_1\sigma_1^* L_{a_1a_1} & \sigma_1^{*2} L_{a_1a_1} & \sigma_2\sigma_1^* M_{a_1b_1} & \sigma_2^*\sigma_1^* M_{a_1b_1} & \sigma_1^* M_{a_1c_1} & \sigma_3\sigma_1^* M_{a_1a_2} & \sigma_3^*\sigma_1^* M_{a_1a_2} & \sigma_1^* M_{a_1b_2} & \sigma_1^* M_{a_1c_2} & \sigma_1^* M_{a_1a_3} & \sigma_1^* M_{a_1b_3} & \sigma_1^* M_{a_1c_3} \\
\sigma_1\sigma_2 M_{a_1b_1} & \sigma_1^*\sigma_2 M_{a_1b_1} & \sigma_2^2 L_{b_1b_1} & \sigma_2^*\sigma_2 L_{b_1b_1} & \sigma_2 M_{b_1c_1} & \sigma_3\sigma_2 M_{b_1a_2} & \sigma_3^*\sigma_2 M_{b_1a_2} & \sigma_2 M_{b_1b_2} & \sigma_2 M_{b_1c_2} & \sigma_2 M_{b_1a_3} & \sigma_2 M_{b_1b_3} & \sigma_2 M_{b_1c_3} \\
\sigma_1\sigma_2^* M_{a_1b_1} & \sigma_1^*\sigma_2^* M_{a_1b_1} & \sigma_2\sigma_2^* L_{b_1b_1} & \sigma_2^{*2} L_{b_1b_1} & \sigma_2^* M_{b_1c_1} & \sigma_3\sigma_2^* M_{b_1a_2} & \sigma_3^*\sigma_2^* M_{b_1a_2} & \sigma_2^* M_{b_1b_2} & \sigma_2^* M_{b_1c_2} & \sigma_2^* M_{b_1a_3} & \sigma_2^* M_{b_1b_3} & \sigma_2^* M_{b_1c_3} \\
\sigma_1 M_{a_1c_1} & \sigma_1^* M_{a_1c_1} & \sigma_2 M_{b_1c_1} & \sigma_2^* M_{b_1c_1} & L_{c_1c_1} & \sigma_3 M_{c_1a_2} & \sigma_3^* M_{c_1a_2} & M_{c_1b_2} & M_{c_1c_2} & M_{c_1a_3} & M_{c_1b_3} & M_{c_1c_3} \\
\sigma_1\sigma_3 M_{a_1a_2} & \sigma_1^*\sigma_3 M_{a_1a_2} & \sigma_2\sigma_3 M_{b_1a_2} & \sigma_2^*\sigma_3 M_{b_1a_2} & \sigma_3 M_{c_1a_2} & \sigma_3^2 L_{a_2a_2} & \sigma_3^*\sigma_3 L_{a_2a_2} & \sigma_3 M_{a_2b_2} & \sigma_3 M_{a_2c_2} & \sigma_3 M_{a_2a_3} & \sigma_3 M_{a_2b_3} & \sigma_3 M_{a_2c_3} \\
\sigma_1\sigma_3^* M_{a_1a_2} & \sigma_1^*\sigma_3^* M_{a_1a_2} & \sigma_2\sigma_3^* M_{b_1a_2} & \sigma_2^*\sigma_3^* M_{b_1a_2} & \sigma_3^* M_{c_1a_2} & \sigma_3\sigma_3^* L_{a_2a_2} & \sigma_3^{*2} L_{a_2a_2} & \sigma_3^* M_{a_2b_2} & \sigma_3^* M_{a_2c_2} & \sigma_3^* M_{a_2a_3} & \sigma_3^* M_{a_2b_3} & \sigma_3^* M_{a_2c_3} \\
\sigma_1 M_{a_1b_2} & \sigma_1^* M_{a_1b_2} & \sigma_2 M_{b_1b_2} & \sigma_2^* M_{b_1b_2} & M_{c_1b_2} & \sigma_3 M_{a_2b_2} & \sigma_3^* M_{a_2b_2} & L_{b_2b_2} & M_{b_2c_2} & M_{b_2a_3} & M_{b_2b_3} & M_{b_2c_3} \\
\sigma_1 M_{a_1c_2} & \sigma_1^* M_{a_1c_2} & \sigma_2 M_{b_1c_2} & \sigma_2^* M_{b_1c_2} & M_{c_1c_2} & \sigma_3 M_{a_2c_2} & \sigma_3^* M_{a_2c_2} & M_{b_2c_2} & L_{c_2c_2} & M_{c_2a_3} & M_{c_2b_3} & M_{c_2c_3} \\
\sigma_1 M_{a_1a_3} & \sigma_1^* M_{a_1a_3} & \sigma_2 M_{b_1a_3} & \sigma_2^* M_{b_1a_3} & M_{c_1a_3} & \sigma_3 M_{a_2a_3} & \sigma_3^* M_{a_2a_3} & M_{b_2a_3} & M_{c_2a_3} & L_{a_3a_3} & M_{a_3b_3} & M_{a_3c_3} \\
\sigma_1 M_{a_1b_3} & \sigma_1^* M_{a_1b_3} & \sigma_2 M_{b_1b_3} & \sigma_2^* M_{b_1b_3} & M_{c_1b_3} & \sigma_3 M_{a_2b_3} & \sigma_3^* M_{a_2b_3} & M_{b_2b_3} & M_{c_2b_3} & M_{a_3b_3} & L_{b_3b_3} & M_{b_3c_3} \\
\sigma_1 M_{a_1c_3} & \sigma_1^* M_{a_1c_3} & \sigma_2 M_{b_1c_3} & \sigma_2^* M_{b_1c_3} & M_{c_1c_3} & \sigma_3 M_{a_2c_3} & \sigma_3^* M_{a_2c_3} & M_{b_2c_3} & M_{c_2c_3} & M_{a_3c_3} & M_{b_3c_3} & L_{c_3c_3}
\end{bmatrix} \tag{A.1}$$

$$\sigma_1^* = (1-\sigma_1) \qquad \sigma_2^* = (1-\sigma_2) \qquad \sigma_3^* = (1-\sigma_3) \tag{A.2}$$

Variables $\sigma_1^*, \sigma_2^*, \sigma_3^*$ represents split ratio of individual coils a_1, b_1, a_2.

$$\boldsymbol{R}^{e}_{abc_{123}} = \begin{bmatrix}
\sigma_1 R_{a_1} & 0 & 0 & 0 & 0 & 0 & 0 & 0 & 0 & 0 & 0 & 0 \\
0 & (1-\sigma_1) R_{a_1} & 0 & 0 & 0 & 0 & 0 & 0 & 0 & 0 & 0 & 0 \\
0 & 0 & \sigma_2 R_{b_1} & 0 & 0 & 0 & 0 & 0 & 0 & 0 & 0 & 0 \\
0 & 0 & 0 & (1-\sigma_2) R_{b_1} & 0 & 0 & 0 & 0 & 0 & 0 & 0 & 0 \\
0 & 0 & 0 & 0 & R_{c_1} & 0 & 0 & 0 & 0 & 0 & 0 & 0 \\
0 & 0 & 0 & 0 & 0 & \sigma_3 R_{a_2} & 0 & 0 & 0 & 0 & 0 & 0 \\
0 & 0 & 0 & 0 & 0 & 0 & (1-\sigma_3) R_{a_2} & 0 & 0 & 0 & 0 & 0 \\
0 & 0 & 0 & 0 & 0 & 0 & 0 & R_{b_2} & 0 & 0 & 0 & 0 \\
0 & 0 & 0 & 0 & 0 & 0 & 0 & 0 & R_{c_2} & 0 & 0 & 0 \\
0 & 0 & 0 & 0 & 0 & 0 & 0 & 0 & 0 & R_{a_3} & 0 & 0 \\
0 & 0 & 0 & 0 & 0 & 0 & 0 & 0 & 0 & 0 & R_{b_3} & 0 \\
0 & 0 & 0 & 0 & 0 & 0 & 0 & 0 & 0 & 0 & 0 & R_{c_3}
\end{bmatrix} \tag{A.3}$$

$$\boldsymbol{e}^{e}_{abc_{123}} = \omega_e \Psi_m \begin{bmatrix} \sigma_1 \cos(\theta + \varphi_{a_1}) \\ (1-\sigma_1) \cos(\theta + \varphi_{a_1}) \\ \sigma_2 \cos(\theta + \varphi_{b_1}) \\ (1-\sigma_2) \cos(\theta + \varphi_{b_1}) \\ \cos(\theta + \varphi_{c_1}) \\ \sigma_3 \cos(\theta + \varphi_{a_2}) \\ (1-\sigma_3) \cos(\theta + \varphi_{a_2}) \\ \cos(\theta + \varphi_{b_2}) \\ \cos(\theta + \varphi_{c_2}) \\ \cos(\theta + \varphi_{a_3}) \\ \cos(\theta + \varphi_{b_3}) \\ \cos(\theta + \varphi_{c_3}) \end{bmatrix} \tag{A.4}$$

B EXPERIMENTAL MOTOR PARAMETERS

Tab. B.1: Experimental motor parameters

Name	Symbol	Value	Unit
DC voltage	U_{DC}	55	V
Maximum continues motor current	I_s	6	A
Winding resistance	R_s	0.45	Ω
Back-EMF constant	λ_{ph}	0.00989	Vs/rad
d-axis inductance	L_d	1.84	mH
q-axis inductance	L_q	1.98	mH
d-axis mutual inductance	M_d	75	µH
q-axis mutual inductance	M_q	163	µH
Nominal speed	ω_n	950	rpm
Maximum speed	ω_M	3500	rpm
Nominal power	P_c	270	W
Number of pole pairs	Pp	21	-
Characteristic current	I_{ch}	5.4	A

C EXPERIMENTAL MOTOR AND TEST BENCH

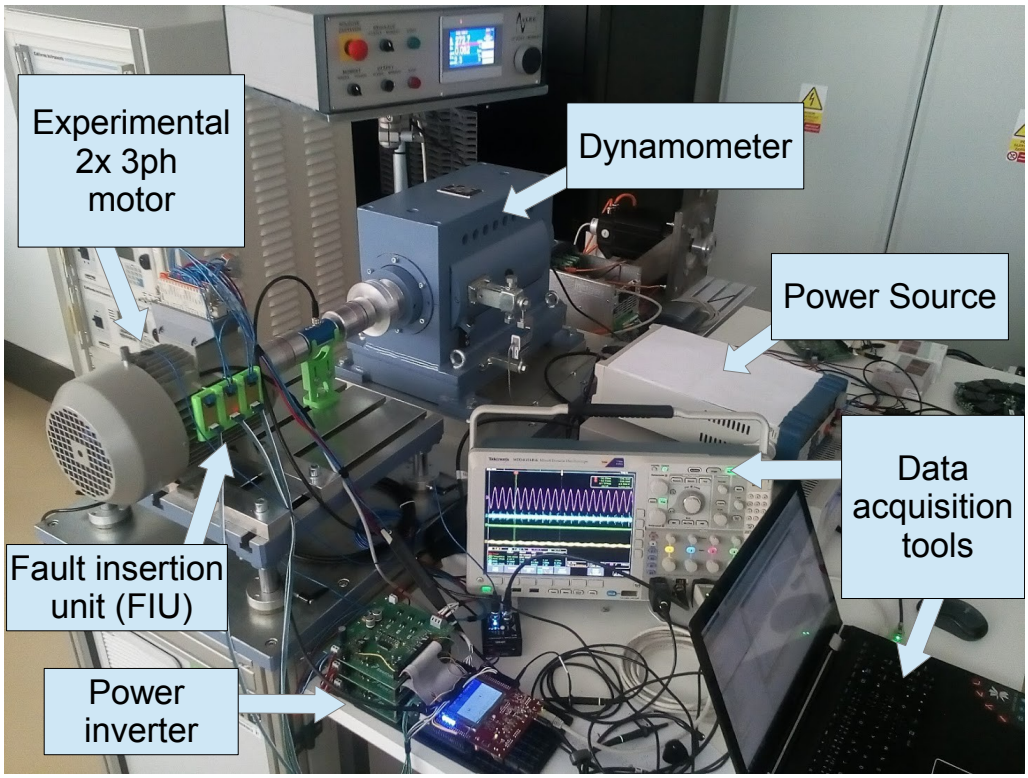

Fig. C.1: Experimental motor connected to the dynamometer.

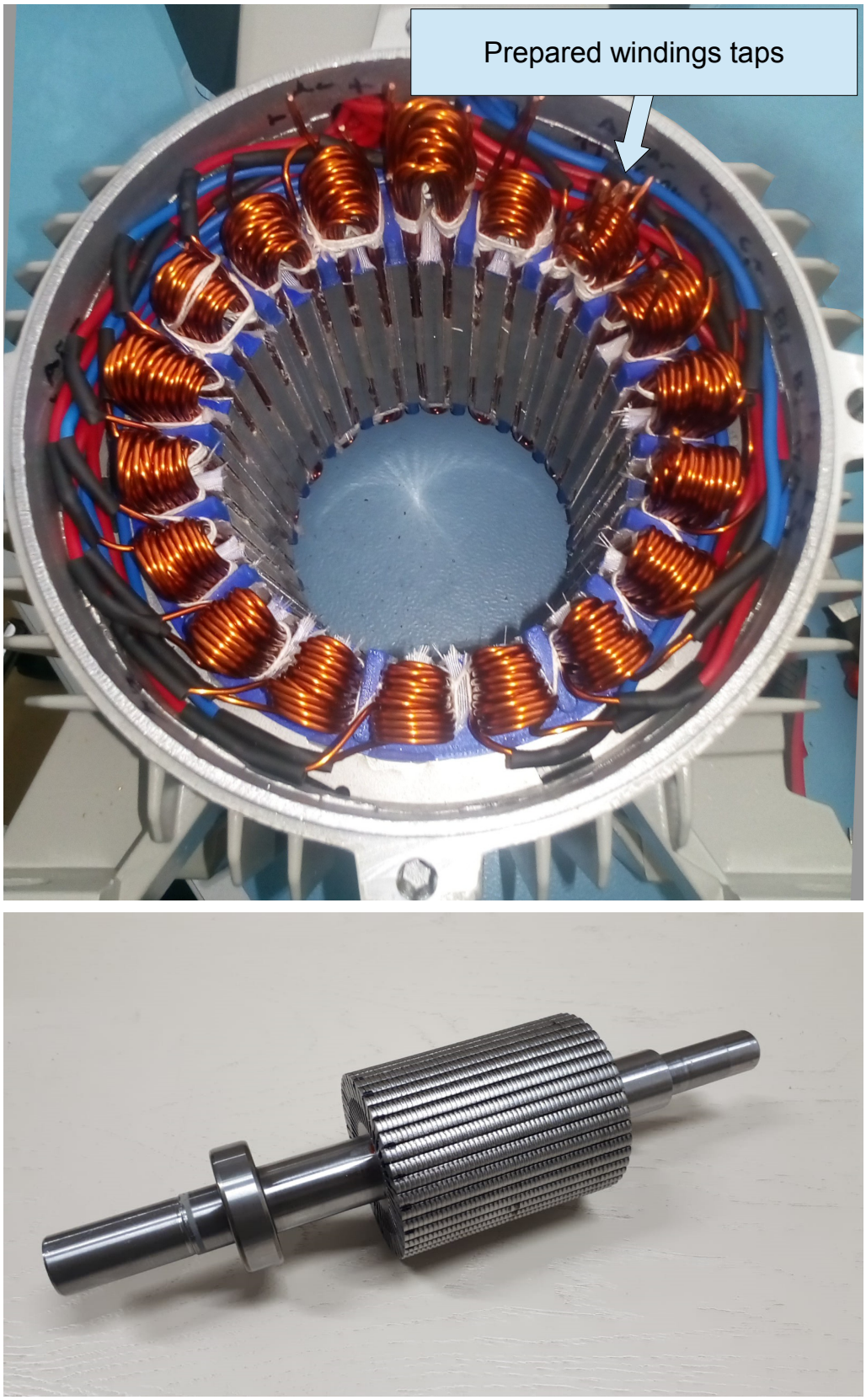

Fig. C.2: Experimental motor stator (top) and rotor with permanent magnets (bottom).